# Durham E-Theses

*The strain-dependence of the critical current density in the high-field superconductor Nb(_3)Sn*

Taylor, David Matthew Joseph

# The strain-dependence of the critical current density in the high-field superconductor $Nb_3Sn$

## David Matthew Joseph Taylor

A thesis submitted in partial fulfilment of the requirements

for the degree of Doctor of Philosophy

Department of Physics, University of Durham

2004

# The strain-dependence of the critical current density in the high-field superconductor Nb₃Sn

## David Matthew Joseph Taylor

**Abstract:** Measurements of the critical current density ($J_C$) of Nb₃Sn superconducting wires were performed as a function of magnetic field ($B \leq 23$ T), temperature (4.2 K $\leq T \leq$ 12 K), and axial strain ($-1.6\% \leq \varepsilon_1 \leq 0.7\%$). Data are presented for wires measured on helical strain springs of different materials and geometries, together with results from finite element analysis (FEA) of these systems. It is demonstrated that the differential thermal contraction of the spring only affects the behaviour of the wire via a change in the parameter $\varepsilon_M$ (the applied strain at the peak), and that the data for different spring geometries show good agreement when the strain is calculated at the midpoint of the wire using FEA. Strain cycling measurement show that the critical current density and $n$-value behave reversibly for applied strains up to 0.3% (~500 cycles), increase irreversibly for strains up to 0.6% (~1000 cycles in total), and decrease irreversibly at higher strains (>0.75%). Comparisons of electric field–temperature characteristics (as measured for the ITER model coils) with the standard electric field–current density characteristics show agreement to within an experimental uncertainty of ~20 mK. Comprehensive $J_C(B,T,\varepsilon_1)$ data are presented for two ITER Nb₃Sn wires, which are characterised by high effective upper critical fields [$B_{C2}^*(0)$]. A new universal relation between normalised $B_{C2}^*(0)$ and strain is reported, which shows a stronger strain-dependence than previous data for binary Nb₃Sn. A power-law relation between $B_{C2}^*(0,\varepsilon_1)$ and $T_C^*(\varepsilon_1)$ (the effective critical temperature) is observed with an exponent of ~2.2, compared to the value $\geq 3$ for binary Nb₃Sn. This is in agreement with microscopic theory, which predicts a power law with an exponent that is lower for dirtier materials, and also shows that the uniaxial strain effects are predominantly due to changes in the phonon properties. A new general scaling law is proposed that parameterises complete $J_C(B,T,\varepsilon_1)$ datasets with a typical accuracy of ~4%, and also provides reasonable predictions from partial datasets.

# *Table of contents*

# *Declaration*

I confirm that no part of the material offered has previously been submitted by me for a degree in this or any other University. If material has been generated through joint work, my independent contribution has been clearly indicated. In all other cases material from the work of others has been acknowledged and quotations and paraphrases suitably indicated

# *Acknowledgements*

I would like to thank the many people who have helped me over the past few years. First of all, thanks to Damian for being a great supervisor—and all that this implies. Particular thanks also to Simon Keys for assistance at the beginning of the Ph.D., Eric Mossang (Grenoble) for support during the very-high-field measurements, Paul Noonan for supervision while at Oxford Instruments, Fred Domptail (Oxford Instruments) for help with the FEA, Neil Mitchell (ITER International Team) for providing useful preprints, and Paul Foley, Matthew King, and Matthew Pritchard for help with various parts of the experimental work. Thanks to all of the support staff in Durham for their assistance, often far beyond the call of duty: Phil Armstrong, Steve Lishman, George Teasdale, Wayne Dobby, Ian Manfren, Mike Lee, Vicky Greener, Pauline Russell, Dave Stockdale, Andy Hunter, John Scott, Tom Jackson, Norman Thompson, Davey Pattinson, John Dobson, Claire Davies, Angela Healer, Norma Twomey, and others. Thanks to friends and colleagues at Durham who helped in many different ways: George Carty, Nicola Morley, Hongjun Niu, Sean Giblin, Tom Hase, and Dan Read. Thanks also to Lars-Olof for organising football, and to Laurent for many excellent kayaking trips. Finally, special thanks to my parents and to Anne-Marie for their love and support.

# *Chapter 1*

## *Introduction*

Superconductivity—when some materials lose all electrical resistance at low temperatures—is a fascinating area of science and the basis for many important technological applications. High-temperature superconductors, first discovered in 1986, can be cooled with relatively inexpensive liquid nitrogen (at a temperature of $-196^\circ$ Celsius) and therefore have the potential to be used in widespread applications such as superconducting power cables. Low-temperature superconductors require liquid helium (at $-269^\circ$ Celsius) but have properties that make them essential for various applications: particularly superconducting magnets. These magnets, consisting of coils of superconducting wire, can be used to generate stable, high magnetic fields using negligible electrical power. They are the main components of Magnetic Resonance Imaging (MRI) scanners, widely used in medicine and a multibillion-pound industry, and NMR spectrometers, used in scientific research. Superconducting magnets are also being used in high-energy particle accelerators, and in the planned International Thermonuclear Experimental Reactor (ITER) to heat and confine a very-high-temperature plasma for fusion.

The most important parameter of a technological superconductor is the maximum current density that can be carried before becoming resistive, the critical current density. Considerable research has been directed at understanding and increasing the critical current density of superconductors in high magnetic fields. The discovery that the magnetic field and temperature dependence of the critical current density can be

described by scaling laws was a very important step in this process. The resulting developments in the low-temperature superconductors (NbTi and $Nb_3Sn$) have been technologically very important, and these developments continue today. In addition to magnetic field and temperature, the critical current density of $Nb_3Sn$ also depends on strain (small deformations of the superconductor), which occurs in magnets due to the forces that are produced when they are cooled and energised. However, measurements of the strain-dependence of the critical current density present a number of experimental difficulties, and are not widely carried out. Various empirical strain scaling laws are commonly used to interpolate and extrapolate data for a particular conductor, but there is currently no consensus on the best approach to scaling, or the underlying physics. For applications such as ITER that use very large-scale magnets, accurate measurements of the critical current density and hence optimisation of the magnet design are extremely important. The aims of the work reported in this thesis were to develop the techniques required to obtain accurate variable-strain critical current density data for $Nb_3Sn$ wires and, using these data, to develop a scaling-law description of critical current density that properly includes the role of strain as well as magnetic field and temperature. The measurements also provide the important engineering data required for the research and development of ITER—probably the most important large-scale international scientific project in the coming decade.

The thesis is structured as follows: Chapter 2 gives an introduction to the fundamentals of superconductivity, first describing the basic phenomena and theoretical ideas and then explaining the mechanisms that determine the critical current density. The next three chapters contain the main experimental results and analysis. In Chapter 3, the properties of the helical springs that are used to measure the strain-dependence of the critical current density are investigated. The apparatus and techniques are described, and experimental data and finite element analysis results are presented for different spring

materials and geometries. These results demonstrate the best approaches for obtaining accurate variable-strain data. Chapter 4 presents the results of strain-cycling measurements to simulate the cyclic charging of the ITER coils. In Chapter 5, comprehensive critical current density data are presented for two $Nb_3Sn$ wires used in the ITER model coils. Various consistency tests and interlaboratory comparisons are first described, and then the data are analysed using a general scaling law. The strain-dependence of the superconducting parameters is described, and their relationship is analysed using microscopic theories of superconductivity. A new scaling law is then proposed, and its accuracy in predicting the properties of $Nb_3Sn$ wires is investigated. Future work is discussed in Chapter 6.

*Chapter 2*

*Fundamentals of superconductivity*

## 2.1 Introduction

This chapter provides an introduction to the basic phenomena and theories of superconductivity, and to flux pinning and the critical current density. In Section 2.2, the characteristic properties of superconductors and the different groups of superconducting materials are described. Section 2.3 summarises the theories used to describe superconductivity, including the phenomenological London theory and Ginzburg–Landau theory, and the microscopic BCS theory. Finally, Section 2.4 describes various models of flux pinning—the mechanism that determines the critical current density of superconductors.

## 2.2 Basic Phenomena

### 2.2.1 Characteristic properties of superconductors

*Critical temperature:* Superconductors undergo a phase transition from the normal state to the superconducting state when they are cooled below a certain critical temperature $T_C$ (see Figure 2.1 on the next page).

*Perfect conductivity:* One of the basic properties of the superconducting state is perfect conductivity (zero electrical resistivity). The observation by Onnes in 1911 of the
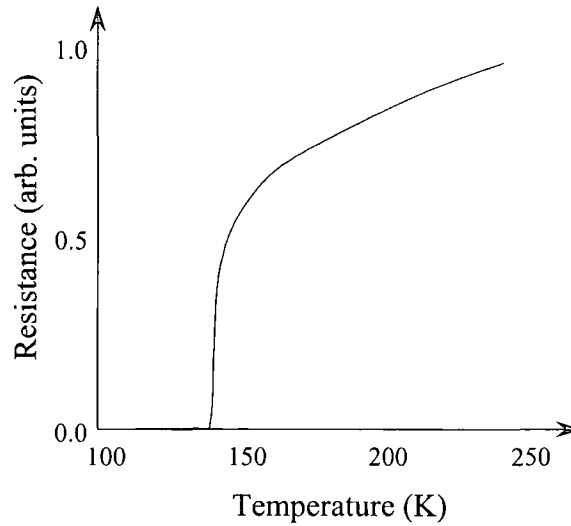
**Figure 2.1** The resistance of $Hg_{0.8}Tl_{0.2}Ba_2Ca_2Cu_3O_{8+\delta}$ as a function of temperature, showing the superconducting transition at 138 K (at the time of writing, the highest $T_C$ at atmospheric pressure) [4].

sudden drop in the resistivity of mercury at a temperature of 4.2 K signified the discovery of superconductivity [1]. Experiments aimed at finding an upper limit for the resistivity have showed that persistent currents flowing around a superconducting ring decay with a time constant of ~150 000 years, implying an average resistivity of less than $10^{-23}$ $\Omega m$ (fifteen orders of magnitude lower than copper) [2].

*Meissner effect:* The second basic property of the superconducting state is the Meissner effect or perfect diamagnetism, the complete exclusion of a small magnetic field (**H**) from the bulk of a superconductor by shielding currents that flow near the surface [see Figure 2.2(a)]. This behaviour was first observed by Meissner and Ochsenfeld in 1933 [3]. The magnetisation due to the screening currents is given by $\mathbf{M} = -\mathbf{H}$ so that the field $\mathbf{B} = \mu_0(\mathbf{H} + \mathbf{M})$ is zero inside the superconductor. The Meissner effect occurs whether the field is applied before or after the material is cooled below $T_C$; the field is expelled as well as excluded.

*Type I and II superconductors, critical magnetic fields:* Superconductor behave in one of two ways as the applied field is increased. Type I superconductors remain in the

(a) Meissner state     (b) Mixed state

(c) Type I     (d) Type II

(e) Type I     (f) Type II
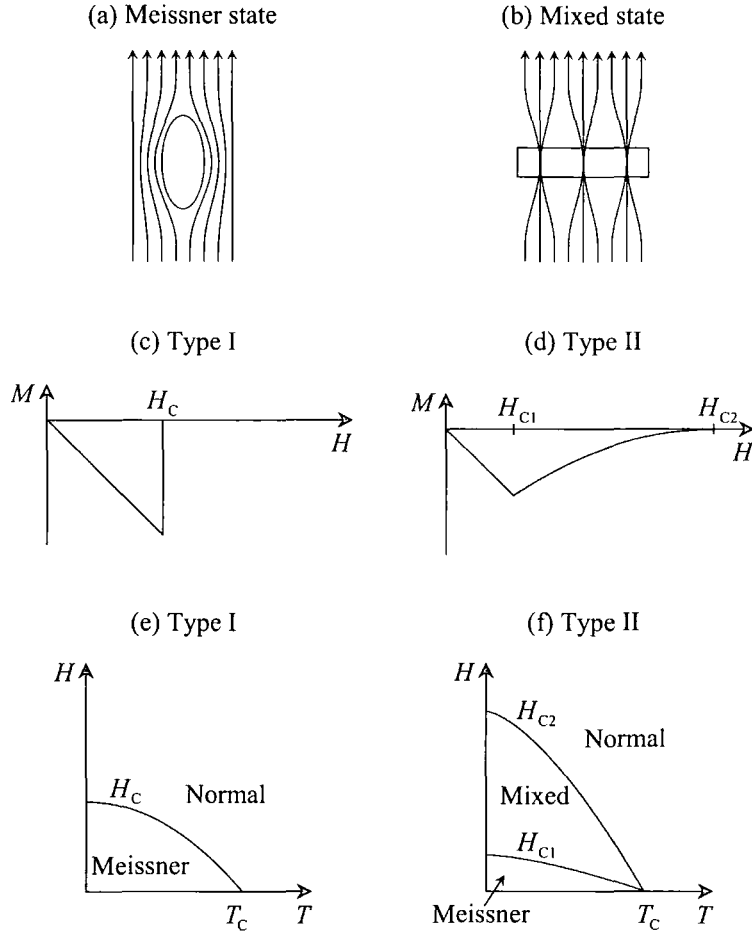
**Figure 2.2** Magnetic states, magnetisation curves, and phase diagrams for type I and type II superconductors

Meissner state until a certain thermodynamic critical field, $H_{\rm c}(T)$, where the superconducting state collapses and the material becomes normal [see Figure 2.2(c)]. Type II superconductors enter a mixed state between a lower critical field, $H_{\rm c1}(T)$, and an upper critical field, $H_{\rm c2}(T)$, and become normal at fields above the upper critical field. The critical fields increase as the temperature is decreased below $T_{\rm C}$, as shown in Figures 2.2(e) and 2.2(f), which represent the phase diagrams of type I and type II superconductors.

*Mixed state:* In the mixed state of type II superconductors, magnetic field penetrates the material in the form of quantised lines of magnetic flux surrounded by vortices of supercurrent [see Figure 2.2(b)]. This state was predicted by Abrikosov in 1957 [5] and

first observed directly some years later by Traüble and Essmann [6] (see also Figure 2.4). The density of flux lines increases as the applied field increases, and $\mathbf{M} \to 0$ ($\mathbf{B} \to \mu_0 \mathbf{H}$) at the upper critical field, as shown in Figure 2.2(d).

## 2.2.2 Superconducting materials

*Metallic elements:* More than 25 metallic elements are now known to be superconductors at atmospheric pressure, with critical temperatures ranging from 325 $\mu$K (rhodium) to 9.25 K (niobium) [7]. A number of others become superconducting at high pressures: for example, lithium has a $T_C$ of 16 K at 80 GPa [8]. Metallic elements are generally type I superconductors, with some exceptions such as niobium. Table 2.1 (on the next page) shows the critical temperatures and critical fields of some common elemental superconductors, as well as for some of the other materials described below.

*Conventional superconducting alloys and compounds:* Superconducting alloys and compounds are generally type II superconductors. An important group of superconductors is made up of *A*15 intermetallic compounds (e.g. $Nb_3X$, $V_3X$ with $X = $ Al, Ga, Si, Ge, or Sn) [9]. These materials generally have the highest critical temperatures of conventional superconductors (e.g. $Nb_3Ge$ with $T_C = 23.2$ K), with the important exception of $MgB_2$—discovered in 2001 to be superconducting with $T_C = 39$ K [10]. Another important group is the Chevrel phase superconductors, such as $PbMo_6S_8$ with a zero-temperature upper critical field of 56 T [11]. The alloy Nb–Ti [$\mu_0 H_{C2}(0) = 15$ T] and the *A*15 compound $Nb_3Sn$ [$\mu_0 H_{C2}(0) = 32$ T] are currently used in almost all superconducting magnets, due to their ability to carry large supercurrents in high magnetic fields (see Section 2.4) [12, 13].

*Cuprate (high-temperature) superconductors:* The first high-temperature super-conductor, La–Ba–Cu–0 with $T_C = 30$ K, was discovered by Bednorz and Müller in 1986 [14]. Discoveries of superconductivity in Y–Ba–Cu–O ($T_C = 92$ K) [15] and

**Table 2.1.** Typical values of critical temperature and critical field for various superconductors. (Type II superconductors unless otherwise stated. Thermodynamic critical fields are shown for type I, and upper critical fields for type II superconductors).

| Material | $T_C$ (K) | $\mu_0 H_C(0)$ (T) (type I) $\mu_0 H_{C2}(0)$ (T) (type II) |
|---|---|---|
| *Elements*[a] | | |
| Al | 1.18 | 0.010 (type I) |
| Pb | 7.19 | 0.080 (type I) |
| Sn | 3.72 | 0.030 (type I) |
| Nb | 9.25 | 0.206 |
| *Conventional superconductors* | | |
| NbTi[b] | 9 | 15 |
| $Nb_3Sn$[c] | 18 | 32 |
| $Nb_3Al$[c] | 18 | 34 |
| $PbMo_6S_8$[d] | 15 | 56 |
| $MgB_2$[e] | 39 | 20 |
| *Cuprate (high-temperature) superconductors*[f] | | |
| $La_{2-x}Sr_xCuO_4$ | 39 | 45 |
| $YBa_2Cu_3O_{7-\delta}$ | 92 | 140 |
| $Bi_2Sr_2Ca_2Cu_3O_{10-\delta}$ | 110 | 180 |

[a] Reference [17].
[b] Reference [12].
[c] Reference [9].
[d] Reference [18].
[e] Reference [19]. Typical upper critical field for bulk samples.
[f] Reference [20]. Upper critical fields parallel to $c$-axis.

Bi–Sr–Ca–Cu–O ($T_C$ = 110 K) [16] soon followed, while currently the material with the highest $T_C$ = 138 K is $Hg_{0.8}Tl_{0.2}Ba_2Ca_2Cu_3O_{8+\delta}$ (see Figure 2.1) [4]. All of the cuprate superconductors are characterised by a layered structure involving $CuO_2$ planes. In contrast to the conventional superconductors, their properties cannot be explained using standard BCS theory (i.e. electron pairing via phonon exchange, see Section 2.3.3).

## 2.3 Theories of superconductivity

### 2.3.1 London equations

The London equations (F. and H. London, 1935 [21]) provide a mathematical description of superconductivity, relating the supercurrent $\mathbf{J}_S$ to the electric field $\mathbf{E}$ and the magnetic field $\mathbf{B}$:

$$\frac{\partial \mathbf{J}_S(\mathbf{r})}{\partial t} = \frac{\mathbf{E}(\mathbf{r})}{\mu_0 \lambda_L^2} \tag{2.1}$$

$$\nabla \times \mathbf{J}_S(\mathbf{r}) = -\frac{\mathbf{B}(\mathbf{r})}{\mu_0 \lambda_L^2} \tag{2.2}$$

$$\lambda_L^2 = \frac{m_e}{\mu_0 e^2 n_s}, \tag{2.3}$$

where $\lambda_L$ is the London penetration depth, $m_e$ is the (free) electron mass, $-e$ is the electron charge, and $n_s$ is the density of superconducting electrons, which is assumed to be constant throughout the superconductor. In the two-fluid model of Gorter and Casimir [22], $n_s$ is assumed to increase from zero at the critical temperature to $n$ (the total electron density) at $T = 0$.

Equation (2.1) implies perfect conductivity: a short pulse of electric field accelerates a supercurrent which then flows persistently. Equation (2.2) can be used to derive the equation $\nabla^2 \mathbf{B} = \mathbf{B}/\lambda_L^2$, which implies the exponential decay of an applied magnetic field with distance into the superconductor and hence the Meissner effect ($\lambda_L$ characterises the penetration depth of the magnetic field). The London equations can be derived from the second Ginzburg–Landau equation [Equation (2.6)] or BCS theory (see Sections 2.3.2 and 2.3.3), and hence emerge from a description of the superconducting state by a (rigid) macroscopic wavefunction.

## 2.3.2 Ginzburg–Landau theory

In Ginzburg–Landau theory (published in 1950 [23]), the superconducting state close to $T_C$ is characterised by a position-dependent complex order parameter $\psi(\mathbf{r})$. The modulus squared of the order parameter gives the effective density of superelectron pairs ($n_p = n_s/2 = |\psi|^2$), while the phase behaves like that of an effective wavefunction (i.e. for gauge transformations). It is postulated that the free energy density can be expanded in powers of $|\psi(\mathbf{r})|^2$ and $|\nabla\psi(\mathbf{r})|^2$ (in a gauge-invariant form), together with a term to account for the energy density of the magnetic field $\mathbf{B}(\mathbf{r}) = \nabla \times \mathbf{A}(\mathbf{r})$. Hence, following Reference [24], the Gibbs free energy density of the superconductor is given by:

$$g_s = g_n + \alpha(T)|\psi|^2 + \frac{\beta}{2}|\psi|^4 + \frac{1}{4m_e}\left|(-i\hbar\nabla + 2e\mathbf{A})\psi\right|^2 + \frac{(\mathbf{B} - \mu_0\mathbf{H}_0)^2}{2\mu_0}, \qquad (2.4)$$

where $g_n$ is the Gibbs free energy density of the normal state, $\alpha(T) = -\alpha_0(1 - T/T_c)$, $\alpha_0$ and $\beta$ are material-dependent positive constants, and $\mathbf{H}_0$ is the applied field. Minimising the free energy density then leads to the following coupled differential equations for the order parameter $\psi(\mathbf{r})$ and the supercurrent density $\mathbf{J}_S(\mathbf{r})$:

$$\frac{1}{4m_e}(-i\hbar\nabla + 2e\mathbf{A})^2\,\psi + \left[\alpha(T) + \beta|\psi|^2\right]\psi = 0 \qquad (2.5)$$

$$\mathbf{J}_s = (1/\mu_0)\nabla \times \mathbf{B} = \frac{ie\hbar}{2m_e}\left(\psi^*\nabla\psi - \psi\nabla\psi^*\right) - \frac{2e^2}{m_e}|\psi|^2\,\mathbf{A}. \qquad (2.6)$$

In the absence of magnetic fields, the order parameter has the equilibrium value $|\psi_\infty(T)|^2 = -\alpha(T)/\beta$ [from Equation (2.5)], and is associated with a superconducting condensation energy [from Equation (2.4)]:

$$\Delta g(T) = g_n(T) - g_s(T) = \frac{[\alpha(T)]^2}{2\beta}. \qquad (2.7)$$

(a) Type I SN interface

$|\psi|^2$        $\lambda(T)$      $B$

Superconducting          Normal

$\xi(T)$

(b) Flux line

$B_z(r)$

$|\psi(r)|^2$

$\xi$     $\lambda$    &rarr; $r$
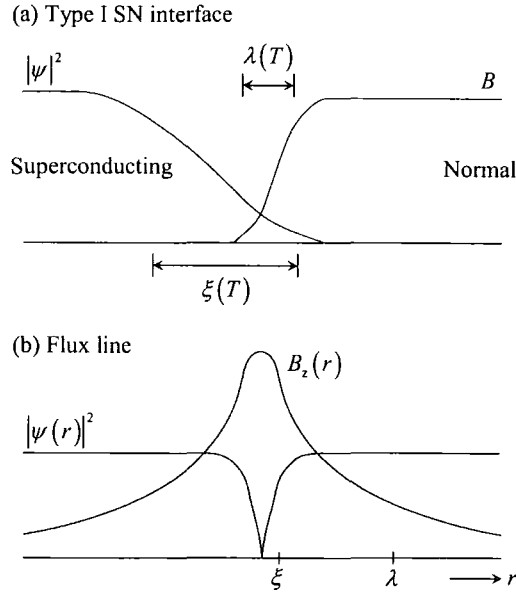
**Figure 2.3** (a) The variation of the order parameter $|\psi|^2$ and the magnetic field $B$ at an interface between a superconducting region and a normal region for a type I superconductor with $\kappa = \lambda/\xi < 1/\sqrt{2}$. (b) The radial-dependence of the order parameter and magnetic field for an isolated flux line in a type II superconductor ($\kappa > 1/\sqrt{2}$). Supercurrents encircle the flux line, with magnitude $|J_0| \propto dB_z/dr$.

In an applied field, the screening currents of the superconductor in the Meissner state raise the Gibbs free energy density of the system [the fourth term on the right-hand side of Equation (2.4)]. For type I superconductors, the thermodynamic critical field is reached when this diamagnetic energy ($\mu_0 H^2/2$) equals the superconducting condensation energy ($\Delta g$), and hence:

$$\mu_0 H_C(T) = \left( \frac{\mu_0 \left[ \alpha(T) \right]^2}{\beta} \right)^{1/2}. \tag{2.8}$$

For type II superconductors, entry into the mixed state at $H = H_{C1} < H_C$ significantly lowers the diamagnetic energy and no transition occurs at $H_C$.

Non-uniform solutions of the Ginzburg–Landau equations involve two characteristic lengths: the coherence length $\xi$, which characterises the distance over which the order parameter can vary:

$$\xi(T) = \left(\frac{\hbar^2}{4m_e|\alpha(T)|}\right)^{1/2},$$ (2.9)

and the Ginzburg–Landau penetration depth $\lambda$, the distance over which the magnetic field or supercurrent density can vary:

$$\lambda(T) = \left(\frac{m_e}{2e^2\mu_0|\psi_\infty(T)|^2}\right)^{1/2} = \left(\frac{m_e\beta}{2e^2\mu_0|\alpha(T)|}\right)^{1/2}.$$ (2.10)

The theory usefully describes the variation of $|\psi|^2$ and $\mathbf{B}$ at an interface between a superconducting and a normal region. Since $|\psi|^2$ gives a negative contribution to the free-energy and $\mathbf{B} - \mu_0\mathbf{H}_0$ gives a positive contribution, the surface energy depends on the relative sizes of $\lambda$ and $\xi$ [see Figure 2.3(a)]. Defining the Ginzburg–Landau parameter $\kappa = \lambda/\xi$, it can be shown that for $\kappa < 1/\sqrt{2}$, the surface energy is positive (a type I superconductor), whereas for $\kappa > 1/\sqrt{2}$, the surface energy is negative (type II).

It was recognised by Abrikosov [5] that the negative surface energy implies that type



(a)                    (b)                    100 nm
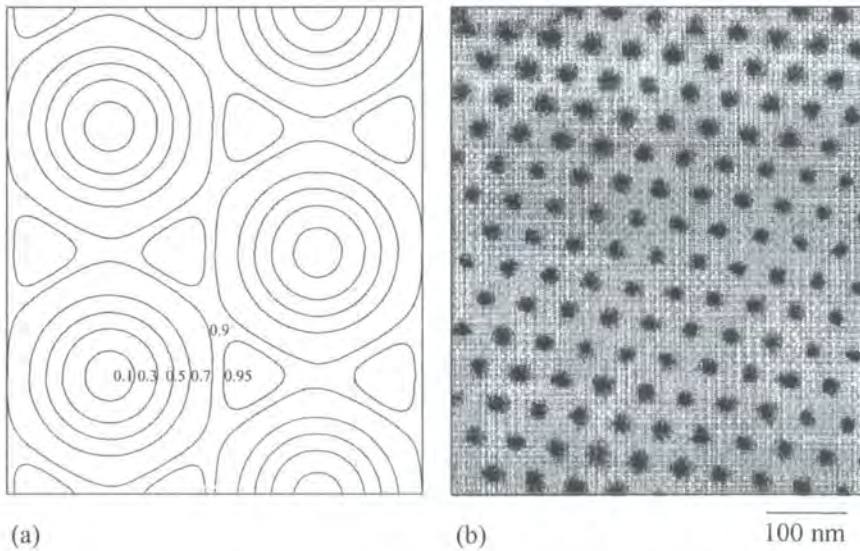
**Figure 2.4** The hexagonal Abrikosov lattice: (a) Contour plot of normalised $|\psi|^2$ calculated using the Ginzburg–Landau equations (the lines also represent contours of magnetic field and streamlines of supercurrent) [25]. (b) Scanning-tunnelling-microscope image [26].

II superconductors enter a mixed state where the magnetic field penetrates the superconductor in the form of normal regions each carrying a single quantum of flux. The quantisation of flux in a superconductor is a direct consequence of the order parameter having a well-defined phase and occurs in units of:

$$\Phi_0 = \frac{h}{2e} = 2.07 \times 10^{-15} \ \text{Tm}^2. \tag{2.11}$$

The structure of an isolated flux line is shown in Figure 2.3(b); it has a normal core (radius $\sim\xi$) where $|\psi| \to 0$ and $B$ is a maximum, surrounded by a region (radius $\sim\lambda$) of circulating supercurrents and decreasing magnetic field. Abrikosov found a periodic solution to the Ginzburg–Landau equations corresponding to lattice of flux lines [5] and it was shown that the most stable configuration is a hexagonal lattice [25], which was later confirmed experimentally (see Figure 2.4) [6, 26]. The nearest-neighbour separation in the hexagonal lattice is given by:

$$a_0 = 1.075 \left( \Phi_0 / B \right)^{1/2}. \tag{2.12}$$

In Ginzburg–Landau theory, the upper critical field is given by:

$$\mu_0 H_{C2}(T) = \frac{2m_e |\alpha(T)|}{e\hbar} = \frac{\Phi_0}{2\pi \left[ \xi(T) \right]^2} = \kappa \sqrt{2} \mu_0 H_C(T), \tag{2.13}$$

which is the field where the separation of flux lines is $\sim\xi$ and the normal cores begin to

**Table 2.2** Typical superconducting parameters for $Nb_3Sn$ at $T = 0$ [27].

| $T_C$ (K) | $H_C$ (T) | $H_{C1}$ (T) | $H_{C2}$ (T) | $\xi$ (nm) | $\lambda$ (nm) | $\kappa$ |
|-----------|-----------|--------------|--------------|------------|----------------|----------|
| 18        | 1.1       | 0.1          | 32           | 3.2        | 64             | 20       |

(a)

(b)
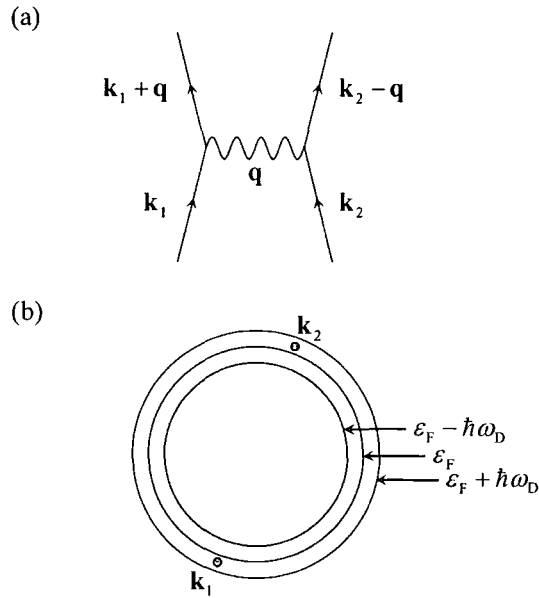
**Figure 2.5** (a) The interaction of two electrons (momenta $\hbar k_1$ and $\hbar k_2$) via exchange of a phonon ($\hbar q$). (b) In BCS theory, the interaction is attractive for electrons within an energy $\hbar \omega_D$ of the Fermi energy $\varepsilon_F$ ($\omega_D$ is the Debye frequency).

strongly overlap. It can be seen that materials with short coherence lengths (high values of $\kappa$) have high values of upper critical field [28]. Table 2.2 shows the set of superconducting parameters for $Nb_3Sn$ (note that the six parameters $H_C$, $H_{C1}$, $H_{C2}$, $\xi$, $\lambda$, and $\kappa$ can be calculated if any two of them are known).

## 2.3.3 BCS theory

In 1957, Bardeen, Cooper, and Schrieffer (BCS) published their microscopic theory of superconductivity [29], which successfully describes conventional, low-temperature superconductors. BCS theory requires a net attractive interaction between electrons, which occurs in conventional superconductors due to the exchange of phonons (lattice vibrations), as proposed by Fröhlich [30]. This is a dynamic process in which one electron polarises the lattice by attracting the positive ions, and the excess ions then attract a second electron. BCS theory uses a simplified description of the electron–phonon–electron interaction (see Figure 2.5), with a constant, attractive interaction $(-V)$

(a)



(b)
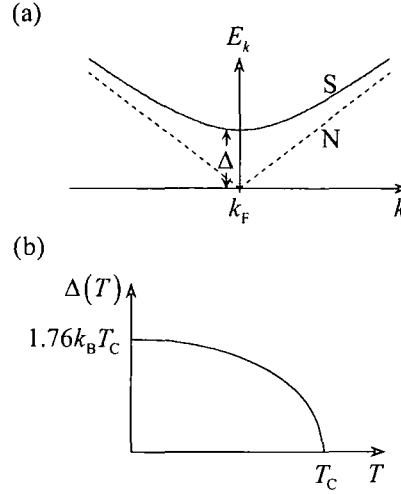


**Figure 2.6.** (a) Excitation energies (for electrons or holes) as a function of momentum near the Fermi surface, shown for the superconducting (S) and normal (N) states. (b) Temperature-dependence of the energy gap in BCS theory.

when the energy of the each electron relative to the Fermi energy ($\varepsilon_{k_1}$ and $\varepsilon_{k_2}$) is less than the typical phonon energy $\hbar\omega_D$ ($\omega_D$ is the Debye frequency):

$$V_{k_1 k_2} = \begin{cases} -V & \left|\varepsilon_{k_1}\right|, \left|\varepsilon_{k_2}\right| < \hbar\omega_D \\ 0 & \text{otherwise} \end{cases}. \tag{2.14}$$

It was shown by Cooper [31] that a weak interaction such as this would lead to the formation of bound electron pairs (Cooper pairs) at the Fermi surface. Hence BCS proposed a wavefunction in which all of the electrons at the Fermi surface form Cooper pairs. The pairs have a binding energy $2\Delta(T)$, implying that there is a minimum energy $\Delta(T)$ required to excite an electron or hole, and hence an energy gap at the Fermi surface [see Figure 2.6(a)]. The gap increases as the temperature decreases below $T_C$ [see Figure 2.6(b)], and has a value at $T = 0$ of:

$$\Delta(0) = 2\hbar\omega_D \exp\left(-\frac{1}{N(0)V}\right), \tag{2.15}$$

where $\omega_D$ is the Debye frequency, $N(0)$ is the electronic density of states (per spin direction) at the Fermi energy, and $-V$ is the matrix element for the electron–phonon–electron interaction. The energy gap is related to the superconducting condensation energy and hence the thermodynamic critical field by:

$$\Delta g(T) = \tfrac{1}{2}\mu_0 \left[ H_C(T) \right]^2 = \tfrac{1}{2} N(0) \left[ \Delta(T) \right]^2. \tag{2.16}$$

The Cooper pairs have no internal orbital angular momentum and hence antiparallel spins, and a characteristic radius given by the BCS coherence length:

$$\xi_{BCS} = \frac{\hbar v_F}{\pi \Delta(0)}, \tag{2.17}$$

where $v_F$ is the Fermi velocity. This radius is typically of order $10^{-6}$ m, implying that there is considerable overlap between the pairs. In fact, the Cooper pairs show a strong interdependence; the binding energy depends on the number of pairs already condensed and the centre-of-mass momentum of every pair is identical (zero in the ground state). Hence, at $T = 0$, supercurrents cannot decay by the normal process of scattering at the Fermi surface because changing the momentum of a single Cooper pair effectively destroys its cooperative binding energy, and cannot occur unless the kinetic energy of the pair is greater than $2\Delta$. (The argument is somewhat more complex at finite temperatures where excitations are present [32].)

The critical temperature in BCS theory is given by:

$$k_B T_C = 1.14 \hbar \omega_D \exp\left( -\frac{1}{N(0)V} \right) = \frac{2\Delta(0)}{3.52}. \tag{2.18}$$

Equation (2.18) predicts that $T_C \propto \omega_D \propto M^{-1/2}$ (where $M$ is the mean atomic mass of the superconductor), in agreement with the observations of the isotope effect in a number of superconductors. Many other aspects of BCS theory have been confirmed experimentally [32].

The standard BCS theory assumes that the electron–phonon coupling is weak [$N(0)V$ is small], but this is not the case for a number of materials (e.g. Pb, Nb$_3$Sn) and the theory must be modified. The equations of strong-coupling (Eliashberg) theory [33, 34] have been solved numerically for specific superconductors, and the results fitted using approximately universal functions. A number of equations for $T_C$ have been proposed, an example of which (the Allen and Dynes equation) is given in Section 5.5.2 [35, 36]. For other quantities, the calculated strong-coupling corrections to the standard BCS values can be expressed in terms of the ratio $T_C/\omega_{ln}$ (where $\omega_{ln}$ is an average phonon frequency) [37].

It was shown by Gor'kov [38] that BCS theory can be used to derive the Ginzburg–Landau equations, and hence relate the adjustable parameters in Ginzburg–Landau theory to the various microscopic parameters of the superconductor: $N(0)$, $v_F$, $\Delta(0)$, and $l$ (the electron mean free path). For example, (using the interpolation formula of Goodman [39]) the expression for the Ginzburg-Landau parameter is:

$$\kappa = 0.957 \frac{\lambda_L(0)}{\xi_0}\left(1 + 0.752 \frac{\xi_0}{l}\right), \qquad (2.19)$$

where $\lambda_L(0)$ is the zero-temperature London penetration depth given by Equation (2.3) with $n_s = n$ [where $n = \frac{4}{3}m_e N(0)v_F^2$ for a Fermi sphere of free electrons]. This combination of microscopic and phenomenological theories—Ginzburg–Landau–Abrikosov–Gor'kov (GLAG) theory—provides a very useful framework for describing the properties of type II superconductors. GLAG theory has also been extended to

temperatures below $T_C$, to describe, for example, the complete temperature-dependence of the critical fields and hence the Ginzburg–Landau parameter [39-43]. The equation for the upper critical field that appears in Section 5.5.2 is an example of this approach (it also includes strong-coupling effects, and the effects of a non-spherical Fermi surface).

## 2.4 Flux pinning and the critical current density

### 2.4.1 Introduction

For type II superconductors in the mixed state, the interaction between a transport current density **J** and the flux lines leads to an effective Lorentz force per unit volume on the flux lines given by $\mathbf{J} \times \mathbf{B}$ [44]. If the flux lines move as a result of this force, then an electric field is induced and energy is dissipated via the normal electrons in the cores [45]. In order for the material to carry a transport current without dissipation, the flux lines must be "pinned" to prevent them from moving. Pinning occurs due to inhomogeneities in the material such as dislocations or grain boundaries, which cause local variations in the superconducting properties. Hence the free energy of the system can change depending on the spatial distribution of flux lines. It is generally energetically
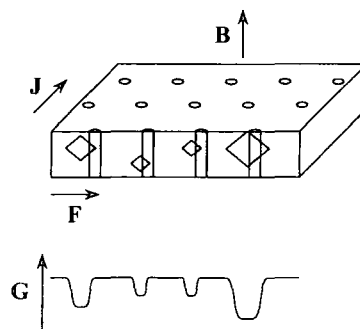


**Figure 2.7.** Flux lines in a type II superconductor subject to the Lorentz force due to a transport current, but pinned by inhomogeneities in the material that cause local variations in the free energy.

favourable for the flux line to occupy the region of the inhomogeneity (see Figure 2.7). The pinning sites are characterised by their dimensions and spacing in relation to the characteristic lengths of the superconductor ($\lambda$, $\xi$, $a_0$), and their superconducting parameters (for example, the pinning sites may be non-superconducting or have different values of $T_C$ or $\kappa$ to the bulk) [46]. The Lorentz force on the flux lines increases as the transport current density increases, and the flux lines begin to move at a certain critical current density, $J_C$. Hence the volume pinning force can be defined as [44]:

$$F_P = J_C B \qquad \text{for } \mathbf{B} \perp \mathbf{J}. \tag{2.20}$$

The magnetic field and temperature dependence of $F_P$ in a number of super-conducting materials can be described by an empirical scaling law first observed by Fietz and Webb [47]:

$$F_P = C(T) f(b), \tag{2.21}$$

where $f$ is a function of the reduced magnetic field $b = B/B_{C2}(T)$ and generally takes the form $f(b) = b^p (1-b)^q$, where $p$ and $q$ are constants for a particular material (e.g. $p = 1$ and $q = 1$ for NbTi, $p = 1/2$ and $q = 2$ for Nb$_3$Sn [48]).

In the following sections, some simple models of flux pinning are described that are particularly applicable to low-temperature, strong-pinning superconductors (e.g. technological NbTi and Nb$_3$Sn). It must be noted that these models are not definitive, but they do usefully illustrate the types of mechanisms that determine the volume pinning force (i.e. vortex–pin and vortex–vortex interactions). A number of other theoretical models have been developed, including collective pinning [49] (which is important for

weak-pinning materials) and collective flux creep [50-52] (important at high-temperatures or at fields close to $B_{C2}$).

## 2.4.2 Pin breaking

If the vortex–pin interactions are sufficiently strong, then the hexagonal structure of the flux-line lattice can be completely disrupted. In this case, all of the flux lines are in pinning sites and the volume pinning force can be obtained from a direct summation of the elementary pinning forces [48].

The pinning site can interact with the magnetic field of the flux line (magnetic pinning) or the normal core (core pinning). The strength of these interactions depends, respectively, on the gradients of **B** ($\sim 1/\lambda$) and $|\psi|^2$ ($\sim 1/\xi$) in the flux lines. Hence, in high-field (short-coherent-length) superconductors, core pinning generally dominates [48, 53]. When an isolated flux-line occupies a non-superconducting region, the approximate reduction in the free energy per unit length of flux line is given by the product of the condensation energy density ($\frac{1}{2}\mu_0 H_C^2$) and the volume of the core per unit length ($\pi\xi^2$):

$$\delta g = \tfrac{1}{2}\mu_0 H_C^2 \pi\xi^2 .$$ 
(2.22)

In a flux-line lattice, the average condensation energy (and hence $\delta g$) is reduced by a factor $(1-b)$ [44]. The elementary pinning force per unit length is then obtained by dividing $\delta g$ by the distance over which the order parameter changes. If the size of the pinning site (in the direction of the Lorentz force) is small, then this distance is determined by the variation of $|\psi|^2$ in the flux-line lattice and is given by $a_0/\pi$ [44]. Hence the elementary pinning force per unit length of flux line is given by [using Equation (2.13)]:

(a) Scaling curves



(b) Pin breaking          (c) Flux line shear
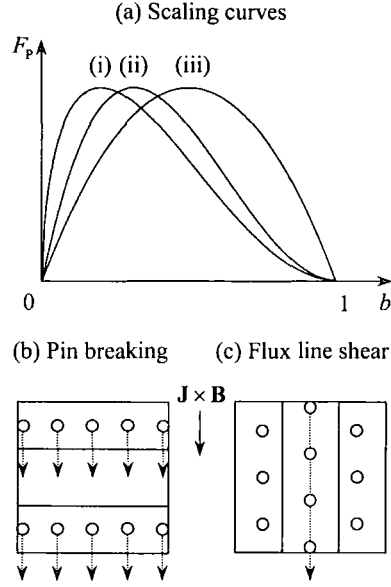
**Figure 2.8** (a) Reduced field dependence of the volume pinning force for (i) $p = 1/2$ and $q = 2$ (e.g. $Nb_3Sn$), (ii) $c_{66}$ (flux-line shear model), and (iii) $p = 1$ and $q = 1$ (pin breaking model, NbTi). (b) Pin breaking (grey areas: pinning sites) and (c) Flux-line shear (grey areas: strong-pinning channels, white area: weak-pinning channel).

$$f_p = \frac{B_{C2}^2 \pi^2 \xi^2 (1-b)}{4\mu_0 \kappa^2 a_0}.$$  (2.23)

For pinning by planar boundaries (e.g. grain boundaries), the total length of pinned flux line per unit volume is $L = S_V / a_0$, where $S_V$ is approximately given by the total area of boundary per unit volume orientated perpendicular to the Lorentz force [46, 48]. Direct summation ($F_p = L f_p$) then gives the following expression for the volume pinning force [using Equation (2.12)] [48]:

$$F_p = \frac{\pi S_V B_{C2}^2}{9.2\mu_0 \kappa^2} b(1-b).$$  (2.24)

In the case of pinning due to normal metallic regions (of smallest dimension $t$) in which superconductivity is induced due to the proximity effect, this expression must be

multiplied by a factor $(t/\xi_{BCS})^2$ (typically of order $10^{-2}$) [54]. For pinning due to local variations in the Ginzburg–Landau parameter ($\Delta\kappa$), the expression is multiplied by $\Delta\kappa/\kappa$ [48]. A number of alternative methods for calculating the pinning energy have also been described [44, 46, 53-55]. The model outlined here shows reasonable agreement with experimental data for NbTi although not for Nb₃Sn [12, 13, 46] (see Figure 2.8). It has been suggested [48] that the morphology of the grains makes flux-line shear the dominant mechanism in Nb₃Sn, as described in the next section.

## 2.4.3 Flux-line shear

If the material contains particular configurations of weak-pinning regions and strong-pinning regions, then the volume pinning force can be determined by the shearing of the flux-line lattice (FLL) around the strongly-pinned regions [53, 56-58].

Models of flux-line shear generally assume that there is a channel of weak pinning surrounded by channels of strong pinning, orientated parallel to the Lorentz force (see Figure 2.8) [53, 56]. The flux lines in the weak-pinning channel are prevented from moving mainly by the rigidity of the flux-line lattice and the neighbouring strongly-pinned flux lines. This causes a shear stress on the FLL that increases as the Lorentz force is increased until it exceeds the shear strength of the lattice, $\tau_{max}$, and the flux lines in the weak-pinning channel begin to move. Hence the volume pinning force is given by:

$$F_P = \frac{2\tau_{max}}{w},$$
(2.25)

where $w$ is the effective width of the weak-pinning channel [53, 56]. The shear strength can be related to the elastic shear modulus of the FLL, $c_{66}$, by:

$$\tau_{max} = Ac_{66},$$
(2.26)

where $1/2\pi \leq A \leq 1/30$ [56, 57]. For large values of $\kappa$, the shear modulus is given by:

$$c_{66} = \frac{B_{C2}^2}{8\mu_0 k_1^2}\left(\frac{\kappa}{\kappa_2}\right)^2 b(1-0.29b)(1-b)^2, \tag{2.27}$$

where $\kappa_1(T)$ and $\kappa_2(T)$ are Maki parameters (equal to the Ginzburg–Landau parameter at $T = T_C$) [59]. Combining Equations (2.25), (2.26), and (2.27) gives an expression for the volume pinning force that is proportional to $c_{66}$, with the reduced-field dependence shown in Figure 2.8.

The predictions of the flux-line shear model show good agreement with experimental data for artificially-structured, two-dimensional systems [56, 57], but not for bulk materials such as $Nb_3Sn$ (see Figure 2.8). In some cases, the effective width of the weak-pinning channel can depend on $a_0 \propto B^{-1/2}$, leading to different field-dependences for $F_p$ [48, 53, 58]. In $Nb_3Sn$, flux-line shear is expected to occur at grain boundaries, where $\kappa$ is increased [due to a reduced electron mean free path, see Equation (2.19)] and hence $c_{66}$ is decreased [Equation (2.27)]. Different models have treated either the grain boundary as the weak-pinning channel (in which case $w = a_0$) or the grain itself (in which case $w = D$ or $w = D - a_0$, where $D$ is the diameter of the grain) [48, 58, 60]. The second case leads to a better agreement with the experimentally observed field-dependence of $F_p$ for $Nb_3Sn$, although the grains do not form a percolative path through the material (i.e. the moving flux lines must also cross grain boundaries) [48]. As yet, there is no definitive theory of flux-line shear for polycrystalline superconductors.

*Properties of helical springs used to measure the effect of axial strain on the critical current density of superconducting wires*

## 3.1 Introduction

Measurements of the axial strain dependence of the critical current density in high magnetic fields provide important information on technological superconducting wires and tapes. The brittle superconductor $Nb_3Sn$ has been studied most extensively [61-75], due to its importance in superconducting magnet technology and large sensitivity to the strains that occur in magnets due to differential thermal contraction and Lorentz forces. For future large-scale and high-field applications of $Nb_3Sn$ (fusion, NMR), quantifying the effect of axial strain ($\varepsilon$) on the critical current density ($J_c$) is particularly important [74, 76]. Axial strain effects have also been investigated in a number of other materials including NbTi [77], $Nb_3Al$ [78-81], $PbMo_6S_8$ [82, 83], $MgB_2$ [64, 84, 85], Bi-2223 [64, 65, 86-90] and YBCO [91]. In these measurements, the techniques used to apply the strain generally fall into one of two categories: "axial-pull" or "bending spring". In the axial-pull technique [61, 73, 92], strain is applied to a short straight sample via end-grips which also serve as the current leads. In the bending-spring technique, the conductor is attached to a thick spring which is then deformed to apply the strain to the sample. Various different spring geometries are used, including the helical ("Walters") spring

[65, 66, 93], which is investigated in this chapter and is used for the measurements in this thesis, the U-shaped spring [62, 64, 85], and the arc-shaped ("Pacman") spring [64, 94].

In standard $J_C$ measurements, the conductor is perpendicular to the applied magnetic field (or to within ~6°) [95, 96]. For axial-pull apparatus used in standard solenoid magnets, the sample length is therefore limited to the diameter of the cold bore: typically 40 mm [61]. U-shaped bending springs generally have a similar sample length [64]. In these short-sample measurements, the current-transfer regions near the current contacts can overlap with the region between the voltage taps, resulting in a current-transfer voltage being measured, which must be corrected for in order to obtain the intrinsic voltage-current characteristics [97, 98]. The electric field criteria used to define $J_C$ are therefore relatively high: typically 200–500 $\mu$Vm$^{-1}$ [61, 62, 97]. Axial-pull apparatus can be used with split-pair magnets in order to increase the sample length to typically 180 mm, although the maximum fields of these magnets are generally lower than solenoid magnets ($\leq$15 T) [73, 92]. A recent variation of the U-shaped bending spring, the Pacman, uses an initially curved beam to increase the sample length to ~120 mm (the circumference of the magnet bore) [64, 94]. The Walters spring has a helical sample geometry similar to that used in (internationally-agreed) standard $J_C$ measurement techniques [66, 99, 100]. This geometry accommodates ~800 mm long samples [65, 66, 93], enabling critical current density measurements to be routinely performed with a sensitivity of 10 $\mu$Vm$^{-1}$ and, with care, at electric fields below 1 $\mu$Vm$^{-1}$ [101].

Axial-pull measurements are limited to tensile applied strains, as samples generally buckle in compression. However, differential thermal expansion of the component parts of the conductor often leads to a compressive prestrain on the superconducting material, which makes measurements possible over a limited range of compressive intrinsic strain [68, 72, 90]. The prestrain can in principle be increased by cladding the conductor in a stainless-steel jacket [102, 103] or using specially-prepared wires [72]. In contrast,

bending-spring measurements enable both compressive and tensile axial strains to be applied to a sample that is attached to the spring. These measurements are particularly important for predicting conductor performance in systems where the structural materials cause a large thermal precompression, such as the cable-in-conduit conductors with stainless-steel jackets used for fusion applications (see Chapter 5) [104]. In bending-spring measurements, differential thermal contraction of the spring and attached sample results in thermal stresses on the sample at cryogenic temperatures (in contrast to axial-pull measurements, in which the sample is free-standing). For measurements on wires, it is generally assumed that the effect of the differential thermal contraction is simply to produce an additional axial strain on the conductor that can be subtracted in order to obtain the intrinsic strain behaviour. Methods for estimating the thermal strain due to the sample holder have been described [65]. In addition, when strain is applied using a bending spring, there is both a transverse strain gradient across the width of the conductor (which depends on the cross-section of the turns of the spring [66, 105]) and a
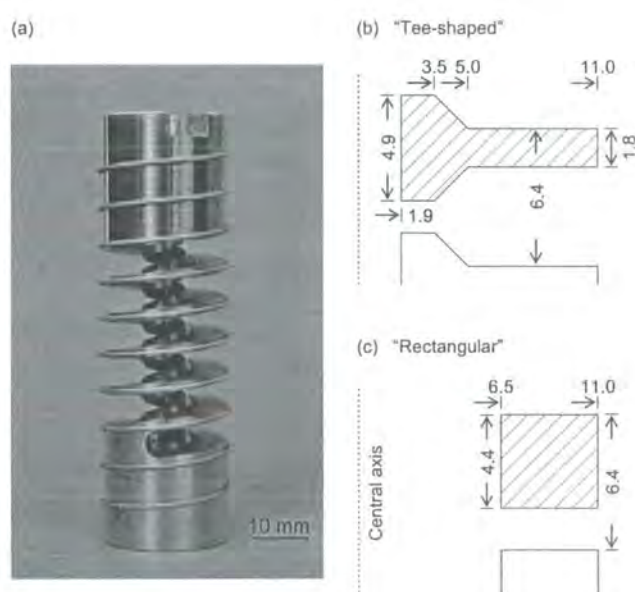


**Figure 3.1.** (a) Photograph of a superconducting wire mounted on a tee-shaped spring; (b) and (c) sections through turns of the tee-shaped and rectangular springs showing radial and axial dimensions in mm.

longitudinal strain variation along the length of the conductor (see Section 3.4.3). Bending springs avoid the possibility of stress concentrations at weak points in the conductor, but the elasticity of the spring is also an issue. It is clear that the properties of the spring are important factors that must be understood in order to perform accurate variable-strain measurements on conductors. Detailed tests are therefore required of the effects of spring material and geometry, as well as comparisons between the different measurement techniques. Some such results have been presented for other types of bending springs [72, 94, 103], but results for helical springs are very limited.

In this chapter (and associated paper [106]), we will present $J_c$ versus axial strain data for Nb$_3$Sn wires measured on helical springs of different materials and geometries, together with results from finite element analysis (FEA) of these systems. The influence of thermal prestrain, elasticity of the spring, and the transverse and longitudinal strain uniformity will be investigated in detail. We will evaluate the extent to which the intrinsic properties of conductors can be accurately measured (and hence to what degree the different measurement techniques are, in principle, equivalent [72, 103]). Based on our experimental and FEA results, we will also make a number of recommendations

**Table 3.1.** Range and uncertainty of the experimental parameters for the $J_c(B,T,\varepsilon)$ measurements.

| Parameter | Range | Uncertainty |
|---|---|---|
| Voltage (Electric field) | $\leq 50\ \mu V$ ($2500\ \mu Vm^{-1}$) | 5 nV noise (Durham) ($0.25\ \mu Vm^{-1}$) |
| Current | $\leq 400$ A (liquid He) $\leq 200$ A (>4.2 K) | 10 mA ($\leq 120$ A) 2 A ($\leq 500$ A) |
| Magnetic field | $\leq 28$ T (Grenoble) $\leq 15$ T (Durham) | 0.5% |
| Temperature | 4.2 to 20 K | 20 mK |
| Applied Strain | +0.7% to $-1.5\%$ ~$10^3$ cycles | 3% |
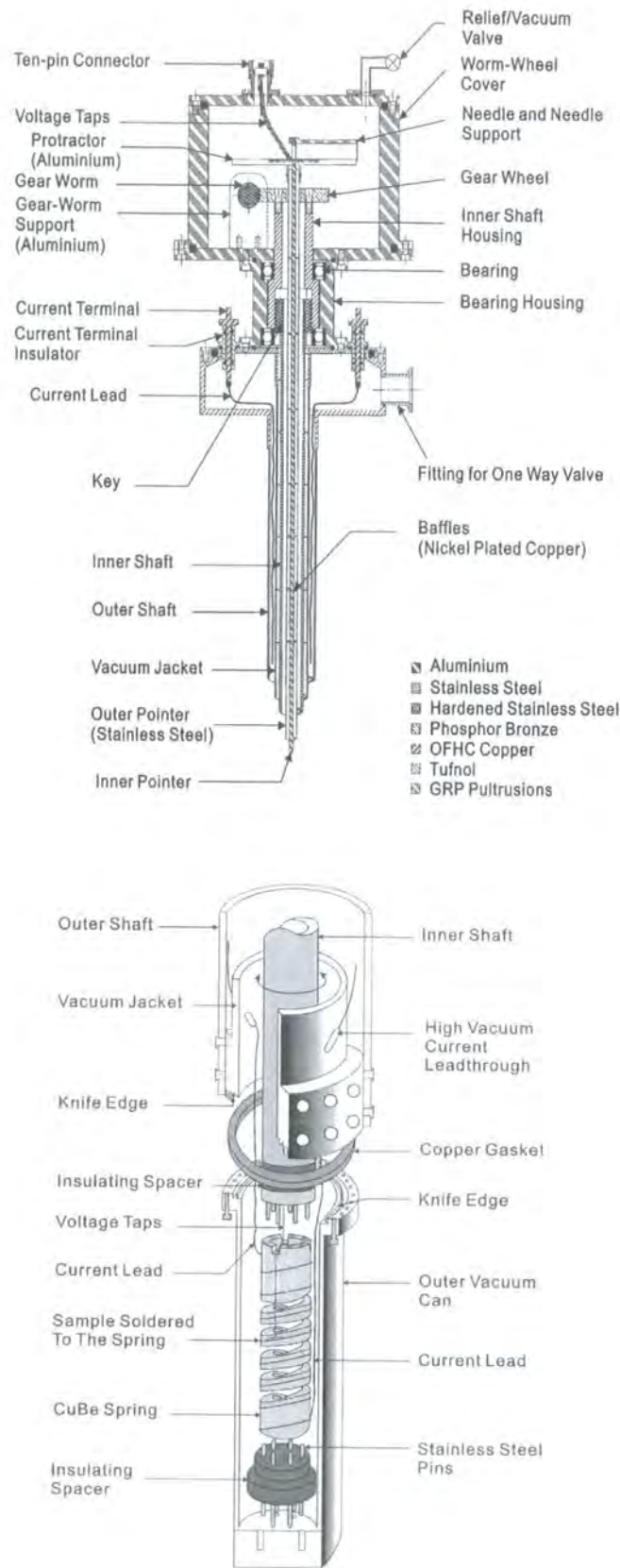
**Figure 3.2.** Schematic diagrams of the top and bottom parts of the $J_c(B,T,\varepsilon)$ probe (reproduced from Cheggour *et al.* [93]).

about the design of helical springs, supplementing previous work by Walters *et al.* [66]. The chapter is organised as follows: Section 3.2 consists of a description of the apparatus and techniques, and the samples investigated; the results of the variable-strain critical current density measurements are presented in Section 3.3; in Section 3.4, the FEA results are presented and comparisons are made with the experimental data; finally, some recommendations on spring design are made in Section 3.5.

# 3.2 Experimental

## 3.2.1 Apparatus and techniques

$J_C(B,T,\varepsilon)$ measurements were performed on superconducting wires attached to helical springs [see Figure 3.1(a)] in which the strain is generated by rotating one end of the spring with respect to the other [66]. The probe (see Figure 3.2) [78, 93] uses two concentric shafts to apply the torque to the spring: the inner shaft connects a worm-wheel system at the top of the probe to the top of the spring, and the outer shaft is connected to the bottom of the spring via an outer can. For measurements at 4.2 K, the outer can contains a number of holes to admit liquid helium from the surrounding bath, whereas for variable-temperature measurements, the outer can forms a vacuum space around the sample with a copper gasket and knife edge seal between the can and the outer shaft. The current leads sit in liquid or gaseous helium for the length of the probe, and enter the vacuum space around the sample via high-current lead-throughs [107]. At particular values of magnetic field, temperature, and strain, measurements are made of the voltage ($V$) across sections of the wire as a function of the current ($I$), which is increased at a constant slow rate.
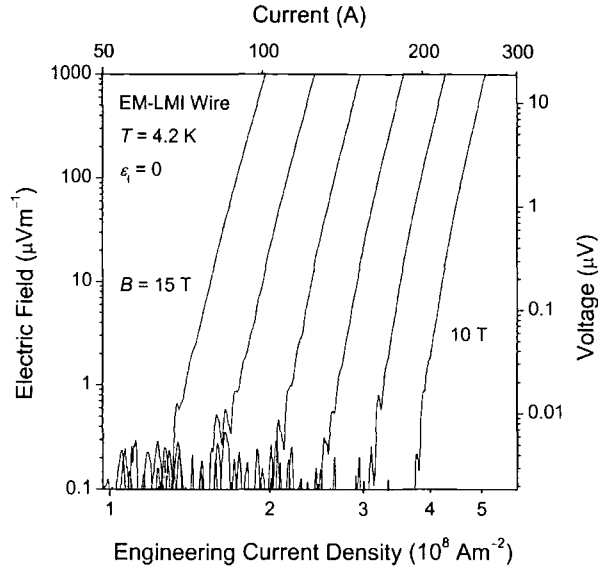
**Figure 3.3.** Log-log plot of electric field versus engineering current density (and voltage versus current) for the EM-LMI wire at a temperature of 4.2 K, zero intrinsic strain, and integer magnetic fields between 10 and 15 T.

A number of modifications to the apparatus have been carried out to increase the range and accuracy of the various experimental parameters (see Table 3.1):

*Voltage:* In order to reduce thermal emfs, the copper voltage leads are continuous from the sample to the voltage amplifiers (except for a set of soldered joints close to the sample, where the temperature is approximately uniform). Measurements are performed using a nanovolt amplifier (EM-Electronics A10), the accuracy of which was checked against a nanovoltmeter (Keithley 182). The amplifier has a voltage noise equivalent to the Johnson noise of a 20 $\Omega$ resistor at room temperature. For a bandwidth of ~1.5 Hz, the expected noise is therefore ~2 nV (half the peak-to-peak value), or ~0.1 $\mu$Vm$^{-1}$ for the typical voltage-tap separation of 20 mm [108]. Figure 3.3 shows a representative set of *V–I* (or *E–J*: electric field–current density) characteristics, where a thermal offset voltage that is a linear function of current (time) has been subtracted from the measured data (typically 1 nV per 100 A). It can be seen that the noise floor is within a factor of ~2 of the amplifier noise. Voltages (electric fields) up to a maximum of ~50 $\mu$V

(2500 $\mu V m^{-1}$) are generally measured, and up to three sections of the wire can be measured simultaneously.

*Current:* The total cross-sectional area of copper wire has been increased considerably in the vacuum space at the bottom of the probe (factor ~10) to reduce the ohmic heating in this region. In addition, the copper plating on the top and bottom parts of the spring (i.e. in the current transfer regions) is made particularly thick (up to ~1 mm), and the electrical contact between the current leads and the superconducting wire are made using this electroplated copper (the solder is applied subsequently). The maximum current that can be applied without heating of the sample is ~400A for

**Table 3.2.** Properties of the different spring materials and of a typical $Nb_3Sn$ wire.

| Material | Thermal expansion 293–4 K (%) | Young's modulus at 4 K [293 K] (GPa) | Poisson's ratio at 4 K [293 K] | Elastic limit at 4 K [293 K] (%) |
|---|---|---|---|---|
| Titanium -4Al-6V | −0.174[a] | 130[b] [110] | [0.31][b] | 1.3[c] [1.0][d] |
| Copper-beryllium (TH04) | −0.317[a] | 132 [119][c] | [0.27][b] | 1.0 [0.9][c] |
| Brass (C27200) | −0.370[e] | [105][f] | [0.34][f] | [0.4][f] |
| Stainless steel 316L | −0.300[a] | 208[a] [193[f]] | 0.28 [0.29][g] | [0.1][f] |
| $Nb_3Sn$ wire | −0.28[g,h] | 25–100[g,i] | — | ~0 [~0][g] |
| Copper | −0.334[g] | 137 [128][g] | [0.31][f] | 0.04 [0.02][g] |
| $Nb_3Sn$ | −0.16[j] | 100 [135][g] | 0.4[j] | — |

[a] Reference [109]. Stainless steel data is for type 316.
[b] Reference [110]. Cryogenic data for Ti-6Al-4V at 20 K.
[c] Reference [66].
[d] Reference [93].
[e] Reference [111]. 70/30 Brass (C26000).
[f] Reference [112].
[g] Reference [113]. Stainless steel data is for type 316LN.
[h] Reference [114]. Vacuumschmelze bronze-route wire.
[i] Reference [115]. A range of tangent modulus values are shown for the $Nb_3Sn$ wire (which behaves plastically). Similar at 293 and 7 K.
[j] Reference [70].

measurements at 4.2 K, and ~200 A above 4.2 K. The uncertainty in the current is estimated to be 10 mA for our 120 A power supply, and 2 A for our 500 A supply.

*Magnetic Field:* Measurements in Durham are performed using our superconducting magnet in fields up to 15 T. An extended vacuum can and inner shaft (~600 mm long) also enable the probe to be used in a tail-dewar with a 38 mm diameter bore in magnetic fields up to 28 T using the resistive magnets at the European high-field laboratory (Grenoble). The field variation over the turns of the spring in both configurations is always less than 0.5%.

*Temperature:* Measurements above 4.2 K are carried out (in a low-pressure helium gas environment) using three independent temperature controllers with Cernox thermometers and constantan wire heaters distributed to produce a uniform temperature profile along the turns of the spring. The thermometers were calibrated commercially in zero magnetic field, and corrected for the small in-field changes to the calibration (more details are given in Section 5.2). The results of various consistency tests show that the uncertainty in the temperature of the wire is ~20 mK (see Section 5.3.2) [67, 78].

*Strain:* A computer-controlled stepper-motor enables experiments involving ~$10^3$ strain cycles to be carried out, with cycles having a typical frequency of 90 s (see Chapter 4) [116]. The uncertainty in the applied strain is estimated to be ~3% from a consideration of uncertainties in the calibration factors obtained from strain-gauge measurements, the correction factors used to calculate the strain at the middle of the wire, and the longitudinal strain variations. These factors are discussed below.

## 3.2.2 Samples

Measurements were made on two types of ITER-candidate ∅0.81 mm $Nb_3Sn$ wire: the EM-LMI internal tin wire and the Vacuumschmelze (Vac) bronze-route wire. The wires were heat-treated in an argon atmosphere on oxidised stainless-steel mandrels

using a three-zone furnace (large isothermal zone), with an additional thermocouple positioned next to the samples in order to monitor the temperature. The heat-treatment schedules were as follows: for the EM-LMI wire, 210°C for 100 h, 340°C for 24 h, 450°C for 18 h, and 650°C for 200 h (ramp rate: 50°C per hour throughout); for the Vac wire, 570°C for 220 h, and 650°C for 175 h (ramp rates: 100°C per hour, 80°C per hour, 100°C per hour). The wires were then etched in hydrochloric acid to remove the chromium plating, transferred to the springs, and attached by copper-plating and soldering (the Ti-6Al-4V spring was nickel-plated prior to attaching the wire). Two different geometries of spring were used for the measurements, details of which are given in Figure 3.1: the first (an older design) has turns with a rectangular cross-section, while the second uses a tee-shaped cross-section (based on the design of Walters *et al.* [66]). Measurements were performed on springs made from a number of different materials: Ti-6Al-4V, copper-beryllium (TH04 temper), brass, and stainless steel (SS) 316L. Table 3.2 shows some of the properties of these materials. Four EM-LMI samples were measured on rectangular springs made from the different materials, and a fifth EM-LMI sample was measured on a tee-shaped spring made from Cu-Be. In addition, Vac samples were measured on a brass rectangular spring and on a Cu-Be tee-shaped spring. Variable-strain $J_c$ measurements were carried out at 4.2 K in magnetic fields up to 23 T in Grenoble (except for the EM-LMI sample on the Cu-Be tee-shaped spring, which was measured in magnetic fields up to 15 T in our superconducting magnet). In all of the measurements, tensile strains were first applied to the sample and then compressive strains. This was to ensure that both tensile and compressive data were obtained before applying the large compressive strains that cause strong plastic deformation of some components of the wire. $J_c$ at zero applied strain was generally found to be reversible after the tensile strain cycle to within ~1%, in agreement with previous strain cycling results (e.g. Chapter 4) [116, 117].
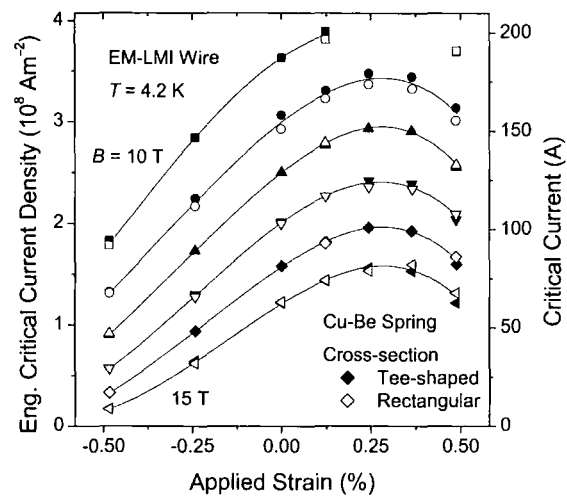
**Figure 3.4.** Engineering critical current density (and critical current) as a function of applied strain at 4.2 K and integer magnetic fields between 10 and 15 T. Data are shown for EM-LMI wires on Cu-Be springs with rectangular and tee-shaped cross-sections. The lines are a guide to the eye.
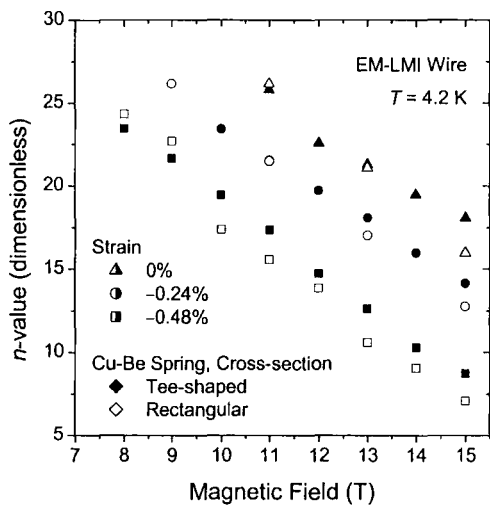


**Figure 3.5.** The $n$-value as a function of magnetic field at different applied strains at 4.2 K for EM-LMI wires on Cu-Be springs with rectangular and tee-shaped cross-sections.

# 3.3 Critical current versus strain results

### 3.3.1 Results for different spring geometries

Figures 3.4 and 3.5 show variable-strain engineering critical current density and $n$-value data for EM-LMI wires mounted on Cu-Be springs with rectangular and tee-shaped cross-sections. $J_C$ is defined at an electric field criterion of $10~\mu Vm^{-1}$, calculated by dividing the critical current by the total cross-sectional area of the wire, and corrected for the normal shunt current (typically 50 mA) [96]. The $n$-value is calculated using $E \propto J^n$ for electric fields between 10 and $100~\mu Vm^{-1}$. The applied strains are calculated using calibration data from strain gauges mounted on the surface of the spring that are corrected using finite element analysis (FEA) to give the strain at the midpoint of the wires as described in Section 3.4.1. Relatively good agreement is found between the
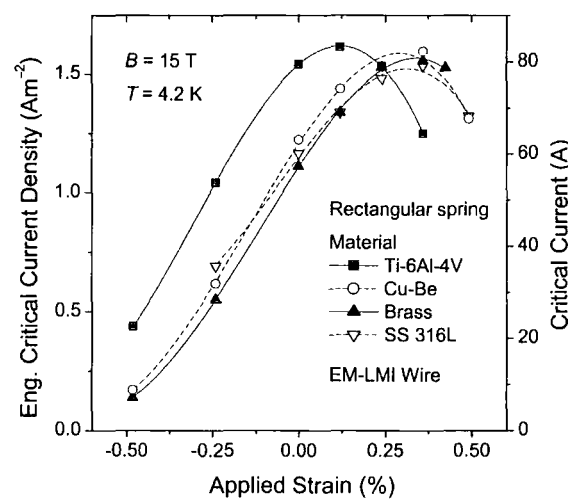


**Figure 3.6.** Engineering critical current density (and critical current) at 15 T and 4.2 K as a function of applied strain for EM-LMI wires on rectangular springs made from four different materials. The lines are a guide to the eye.
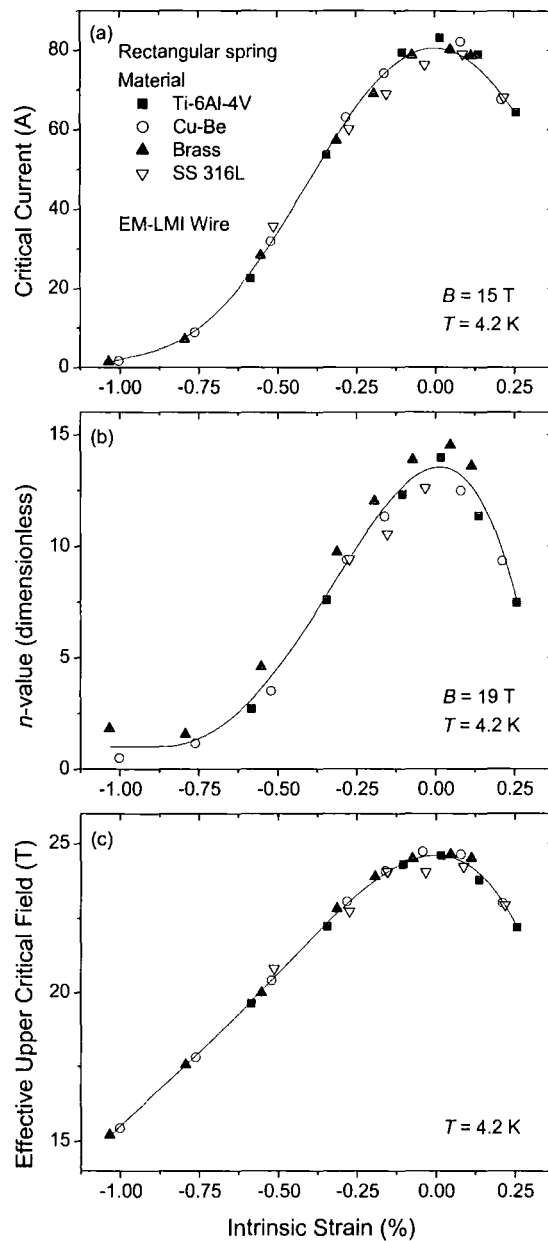
**Figure 3.7.** (a) Critical current at 4.2 K and 15 T, (b) *n*-value at 4.2 K and 19 T, and (c) effective upper critical field at 4.2 K as a function of intrinsic strain for EM-LMI wires on four different spring materials. The lines are a guide to the eye. Intrinsic strain was calculated from the applied strain by subtracting the value at which the effective upper critical field is a maximum.

results for the two different spring geometries: the $J_C$ data superimpose to within ±2%, and the *n*-value data to within ±10%. These results therefore validate the methods used to obtain the characteristic strain for the wire (see Section 3.4.1).

## 3.3.2 Results for different spring materials

Figure 3.6 shows the engineering critical current density as a function of applied strain ($\varepsilon_A$) for EM-LMI wires on rectangular springs made from four different materials.
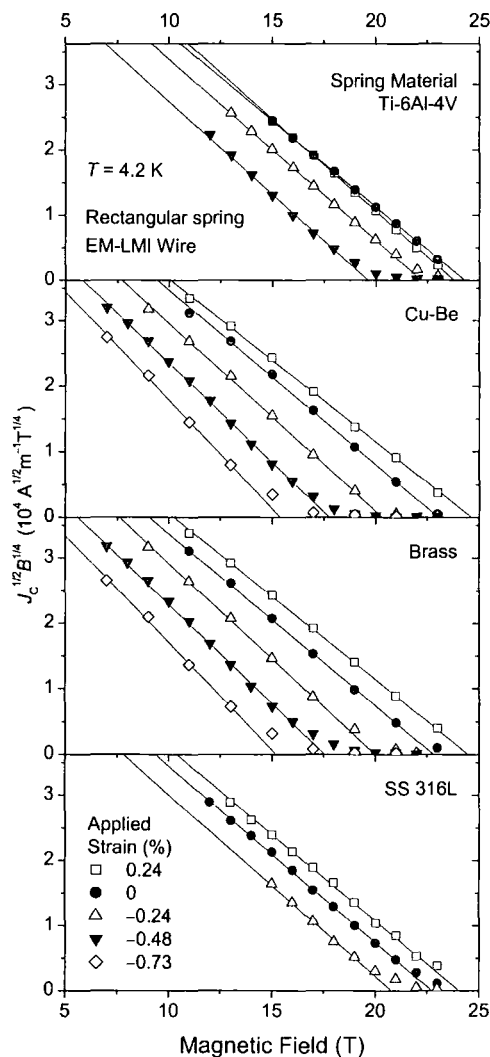


**Figure 3.8.** Kramer plots at different applied strains at 4.2 K for EM-LMI wires on rectangular springs made from four different materials.
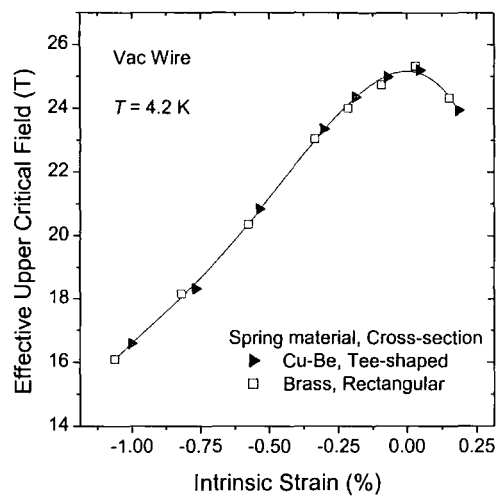
**Figure 3.9.** Effective upper critical field at 4.2 K as a function of intrinsic strain for Vac wires on springs of different materials and cross-sections. The line is a guide to the eye.
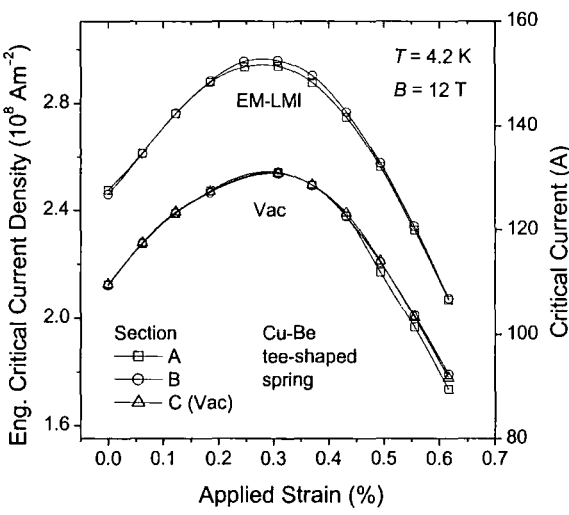


**Figure 3.10.** Engineering critical current density (and critical current) as a function of applied strain at 12 T and 4.2 K for three different sections of a Vac sample and two different sections of an EM-LMI sample, both on Cu-Be tee-shaped springs. The lines are a guide to the eye.

The spring material clearly affects the relationship between $J_C$ and applied strain, and in particular the position of the peaks in $J_C(\varepsilon_A)$. Intrinsic strain $(\varepsilon_I)$ is defined relative to the applied strain where $J_C$ is a maximum $(\varepsilon_M)$ by:

$$\varepsilon_I = \varepsilon_A - \varepsilon_M. \tag{3.1}$$

It is found by plotting $J_C$ as a function of intrinsic strain, that the data for the four different spring materials approximately superimpose, typically to within ±5% [see Figure 3.7(a)]. Similar agreement is also found for the *n*-value [Figure 3.7(b)] and the effective upper critical field [Figure 3.7(c)]. The values of effective upper critical field $[B_{C2}^*(4.2\ \text{K})]$ were obtained from Kramer plots ($J_C^{1/2}B^{1/4}$ versus $B$), examples of which are shown in Figure 3.8 [58]. The level of agreement between the different samples is typically ±1% for the $B_{C2}^*(4.2\ \text{K})$ data as a function of intrinsic strain. The largest deviations from the universal curves are observed for the stainless steel spring. This can be attributed to plastic yielding of the steel, which has an elastic limit of ~0.1%, and difficulty bonding the wire to the spring. The different values of $\varepsilon_M$ are related to the additional thermal strains due to the sample holder, which vary according to the thermal expansion of the material used (see Table 3.2). The universal intrinsic strain dependences show that these additional strains are similar in nature to the applied (mechanical) strains, so that the same strain-state in the wire is obtained from different combinations of applied (mechanical) strain and thermal strain. In Section 3.4.2, the measured values of $\varepsilon_M$ will be compared with predictions from FEA.

Figure 3.9 shows the values of effective upper critical field at 4.2 K obtained from measurements on Vac wires mounted on springs of different materials and geometries (a brass rectangular spring and a Cu-Be tee-shaped spring). These data also lie on a universal curve as a function of intrinsic strain to within ±1%.

### 3.3.3 $J_C$ homogeneity along the wire's length

Figure 3.10 shows the strain-dependence of $J_C$ for different sections of Vac and EM-LMI samples on Cu-Be tee-shaped springs. Each section was ~20 mm long and separated by approximately one turn. The $J_C$ data agree to within ±2% for both samples, which is typical of the samples that we have investigated, although on one occasion (one in fifteen samples) significantly different behaviour is observed for one of the sections of the wire [93].

## 3.4 Modelling results and comparisons with experimental data

### 3.4.1 Results for different spring geometries

*3.4.1.1 Analytic equations* Walters *et al.* gives the following expression for the circumferential strain $\varepsilon_{\theta\theta}$ in a helical bending spring as a function of the radial distance $r$ [66]:

$$\varepsilon_{\theta\theta} = K\left(1 - r_n/r\right), \tag{3.2}$$

where $K$ is a factor that depends on the applied angular displacement $\theta$, the number of turns of the spring $N$, and the pitch angle $\alpha$:

$$K = \left(\theta/2\pi N\right)\cos\alpha. \tag{3.3}$$

The position of the neutral radius $r_\text{n}$ can be calculated using the condition that there is no net force perpendicular to the cross-section of the spring, i.e.:

$$\int w(r)E(r)\varepsilon_{\theta\theta}(r)\,\mathrm{d}r = 0, \tag{3.4}$$

where $w$ is the width of the section (in the axial direction) and $E$ is the Young's modulus (both of these quantities can vary with position to allow for complex spring geometries and the presence of the wire—the integral can generally be calculated analytically). Equations (3.2)–(3.4) can be used to predict the strain-state in springs and attached wires, although the treatment does not consider the effects of the complex distortions that occur when the spring is twisted [66]. These "loaded beam" equations will be compared with results obtained from finite element analysis in the next section.
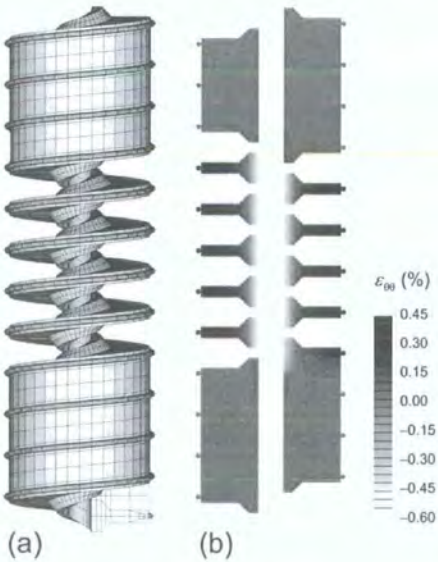


**Figure 3.11.** (a) FEA model of a tee-shaped spring with attached wire. (b) The circumferential strain on a plane through the centre of the spring at an angular displacement of +15°.
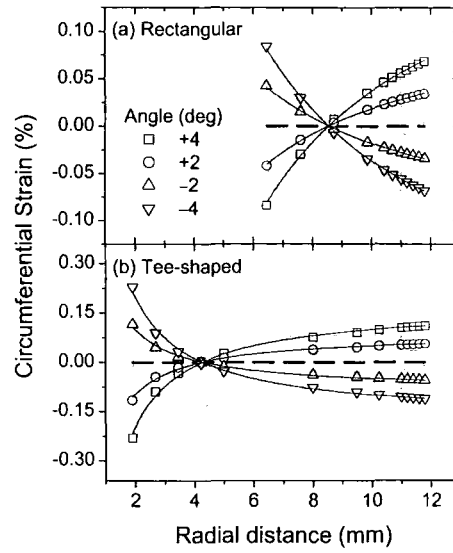
**Figure 3.12.** The circumferential strain as a function of the radial distance at different angular displacements for (a) rectangular and (b) tee-shaped springs with attached ∅0.81 mm wires. The symbols show the FEA results at the centre of the cross-section (shown by the dashed lines), while the solid lines show fits made using Equation (3.2). The variation in strain in the axial direction is negligible (see Figure 3.11).

*3.4.1.2 Finite element analysis* Finite element analysis was carried out using the software package Strand7 (G+D Computing, Australia). A typical finite element model consisting of ~20 000 8-node brick elements is shown in Figure 3.11(a). The results were found to change by less than 1% for further increases in mesh density. The models used elastic-plastic material properties with stress-strain curves defined via a modified power-law fit to the following parameters: Young's modulus, yield stress, ultimate stress, and elongation at ultimate stress [113]. Figure 3.11(b) shows the circumferential strain due a +15° (anticlockwise) rotation of one end of the spring. The strain is approximately independent of axial position throughout the cross-section of a turn of the spring. The variation of circumferential strain with radial distance (along the centre of the cross-section) is shown in Figure 3.12 for the Cu-Be rectangular and tee-shaped springs used in the $J_C$ vs. $\varepsilon$ measurements. The FEA results can be fitted quite accurately using Equation

(3.2) with $r_n$ and $K$ as free parameters (lines in Figure 3.12). The values of $r_n$ obtained from the FEA (8.52±0.01 mm for the rectangular spring and 4.24±0.03 mm for the tee-shaped) agree well with those calculated using Equation (3.4) (8.54 and 4.24 mm). The two methods therefore give approximately the same radial-dependence for the strain in the turns, although not the same absolute values of strain (discussed below).

For the spring in the elastic regime, a linear relation between strain and angle is

**Table 3.3.** Calibration factors (% applied strain per degree angular displacement) for the Cu-Be rectangular and tee-shaped springs. Factors obtained from finite element analysis and the loaded-beam equations are shown for springs with and without attached wires ($\varnothing 0.81$ mm, $E = 30$ GPa ), giving the strain at the outer surface of the spring, at the active part of a strain gauge (i.e. 45 μm above the surface of the spring) and at the middle of the wire. The corrected calibration factors (for the middle of the attached wire) are calculated from the measured values (for strain gauges on springs without attached wires) using the FEA results.

| Cu-Be spring geometry | Position | Calibration factor (% per degree) | | | |
|---|---|---|---|---|---|
| | | Measured | FEA | Loaded-beam eqs. | Corrected |
| | | with shafts | no shafts | no shafts | with shafts |
| Rectangular | | | | | |
| No attached wire | Outside of spring | | 0.0143 | 0.0156 | |
| | Strain gauge | 0.0139 | 0.0145 | 0.0158 | |
| Attached wire | Outside of spring | | 0.0141 | 0.0155 | |
| | Middle of wire | | 0.0159 (+9.3%) | 0.0174 (+10.1%) | 0.0152 |
| Tee-shaped | | | | | |
| No attached wire | Outside of spring | | 0.0269 | 0.0380 | |
| | Strain gauge | 0.0221 | 0.0269 | 0.0381 | |
| Attached wire | Outside of spring | | 0.0267 | 0.0379 | |
| | Middle of wire | | 0.0275 (+2.0%) | 0.0388 (+1.7%) | 0.0226 |

observed experimentally in strain-gauge calibrations, obtained from the finite element analysis (to within ~0.5%), and predicted by Equation (3.3). Table 3.3 shows calibration factors defined as the strain per unit angular displacement at various radial positions: the outer surface of the spring, the active part of a strain gauge (total height above the surface of the spring: 45 μm [118]), and the midpoint of a ⌀0.81 mm wire. Calibration factors are presented for strain-gauge measurements on springs without attached wires in the strain-probe (helical strain), finite element analysis (helical strain, averaged over the central turns of the spring, see Section 3.4.3), and the loaded-beam equations (circumferential strain). Helical strain is defined as the strain parallel to the helical path at a particular radius (e.g. the axis of the wire), and differs from the circumferential strain by typically 1% on the outer surface of the spring. The measured calibration factors are the lowest of the three factors, primarily because of the shafts and connectors twisting in the probe. (The rotation of the top of the spring is measured directly, but, in standard operation, the rotation of the bottom of the spring is measured via the shafts and connectors that carry the torque.) For the rectangular springs, there is reasonable agreement between the measured calibration factor and the value from FEA. The larger differences observed for the tee-shaped spring are consistent with the prediction that the torque required per unit angular displacement is a factor of ~4 larger for this spring (see Tables 3.3 and 3.4). The calibration factors from the loaded-beam equations are considerably larger than the FEA values, which can be attributed to the effects of the radial compression and the distortion of the envelope of the turns that occur when the spring is twisted. These effects are not included in the loaded-beam equations and are expected to reduce the strains relative to the calculated values [66]. Strain-gauge measurements show that the calibration factors are independent to within ~2% of both spring material and temperature (293–4 K), consistent with FEA and the loaded-beam equations for springs with and without attached wires.

**Table 3.4.** Design parameters for the Cu-Be rectangular and tee-shaped springs, obtained both from FEA and the loaded-beam equations.

| Cu-Be spring geometry | Strain gradient across $\varnothing$0.81mm wire (%) | Torque per % applied strain (Nm) | Ratio of strain at inside of spring to strain at outside of spring |
|---|---|---|---|
| | FEA [loaded-beam eqs.] | | |
| Rectangular | ±9.9 [±10.5] | 27 [22] | −1.47 [−1.44] |
| Tee-shaped | ±2.9 [±2.1] | 67 [63] | −2.16 [−1.97] |

The FEA results have been used to relate the measured calibration factors (for which the strain gauge is attached to the surface of a spring without an attached wire) to the strain at the midpoint of a $\varnothing$0.81 mm wire attached to the spring. For these wires, there is negligible difference between the calculated strain at the midpoint and the mean strain on the filaments. As shown in Table 3.3, the effect of attaching a wire ($E = 30$ GPa) to the spring decreases the calibration factor, whereas the radial-dependence of the strain and the different radial positions of the strain gauge and the midpoint of the wire cause the calibration factor to increase (see Figure 3.12). For the experimental data presented in this thesis, the strain values are always quoted for the midpoint of the wire using the corrected calibration factors. The FEA corrections are ~2% for the tee-shaped spring and ~9% for the rectangular spring, the magnitudes of which are confirmed by the loaded-beam equations. The good agreement between the results for different spring geometries demonstrates that this approach is valid (Figures 3.4, 3.5, and 3.9).

The transverse strain gradient across the wire differs considerably between the two spring geometries. The variations are approximately ±10% for the rectangular spring and ±3% for the tee-shaped spring (see Table 3.4), although these values are somewhat smaller over the central region of the wire occupied by the superconducting filaments

(approximately $\varnothing 0.7$ mm for the EM-LMI wire and $\varnothing 0.5$ mm for the Vac wire [119]). For the EM-LMI wire on the rectangular spring, the variation in strain corresponds to a variation in $B^*_{C2}(4.2 \text{ K})$ of $\pm 0.5$ T at an applied strain of $-0.5\%$, while for the tee-shaped spring the variation is $\pm 0.1$ T. The agreement in the $n$-values for the different spring geometries, as shown in Figure 3.5, is to be expected if the intrinsic variations in the superconducting properties—due to composition gradients, for example—are larger than those due to the strain gradient [13, 120].

The data in Table 3.3 are valid for the elastic regime of the spring material, where critical current versus strain measurements are generally carried out. Table 3.4 shows the ratio of the circumferential strain at the inside of the spring to the circumferential strain at the outside of the spring for the two different geometries (see Figure 3.12). The magnitude of the strain is higher at the inner surface, and so the spring will yield first in this region. We note that finite element analysis shows that at the inner surface of the spring, the circumferential strain is significantly different from the helical strain but has a similar magnitude to the von Mises equivalent strain [121] that is appropriate for considering plastic yielding. For a spring made of Cu-Be (with an elastic limit of 1%), yielding occurs when the strain on the outer surface is ~0.5% for the tee-shaped cross-section and ~0.7% for the rectangular cross-section. Since some of the data presented in Section 3.3 were obtained at high compressive strains where parts of the spring are in the plastic regime, the possible effects of plasticity also need to be considered. In strain-gauge measurements performed at room temperature on the Cu-Be rectangular spring (and a Ti-6Al-4V tee-shaped spring), deviations from the linear relation between strain and angle observed for the elastic regime became significant (equal to +2%) at an applied strain of $-1.5\%$ ($-0.9\%$ for the Ti-6Al-4V tee-shaped spring). These results are consistent with FEA that includes the role of plasticity and confirms that yielding at the inner surface does not have a very large effect on the average strain at the outer surface,

primarily because most of the spring remains elastic. At the highest strains where the strain–angle relationship is nonlinear, measurements can still be performed accurately if the strain-gauge calibrations and the measurements are performed using the same sequence of applied strains.

Finite element analysis provides useful information about the changes in the spring's dimensions when a torque is applied. At angular displacements corresponding to ±1% applied strain, the predicted change in the spring's height (from 75 mm) is ±0.5 mm for the rectangular spring and ±1 mm for the tee-shaped spring. Our strain probe has a sliding keyway in the inner shaft to accommodate this change. If the spring is constrained so that the ends cannot move vertically, the calibration factor is predicted to be somewhat larger (~0.5%) for the rectangular spring and considerably larger (~5%) for tee-shaped spring. In addition, the outer diameter increases at compressive applied strains; the maximum increases are 1.5 mm (rectangular) and 0.5 mm (tee-shaped) at −1% strain. (Similar decreases occur for the inner diameter at tensile applied strains.)

### 3.4.2 Results for different spring materials

It is well known that at cryogenic temperatures the filaments in a $Nb_3Sn$ wire are under compressive strain due to differential thermal contraction. It is generally assumed that the peak in the critical current density occurs when the applied axial strain cancels the axial component of this thermal strain (i.e. a one dimensional model is correct to first-order) [68-70]. Hence we can write down the following formula for the applied axial strain at the peak ($\varepsilon_M$) for our particular measurement procedure:

$$\varepsilon_M = -\left( \left( \tfrac{\Delta l}{l} \right)^{923-293 \text{ K}}_{\text{Isolated wire}} + \left( \tfrac{\Delta l}{l} \right)^{293-4 \text{ K}}_{\text{Wire on spring}} - \left( \tfrac{\Delta l}{l} \right)^{923-4 \text{ K}}_{Nb_3Sn \text{ compound}} \right). \tag{3.5}$$

**Table 3.5.** Calculated change in length between 293 and 4 K of the EM-LMI $Nb_3Sn$ wire ($\varnothing$0.81 mm, $E = 30$ GPa ) on rectangular springs of different materials, and predicted and measured values of $\varepsilon_M$.

| Spring material | Length change of wire 293–4 K (%) | $\varepsilon_M$ (%) | |
|---|---|---|---|
| | FEA [force-balance eq.] | Predicted (FEA) | Measured |
| Titanium-4Al-6V | −0.184 [−0.174] | 0.12 | 0.10 ±0.02 |
| Copper-beryllium | −0.315 [−0.316] | 0.255 | 0.28 ±0.02 |
| Brass | −0.364 [−0.369] | 0.30 | 0.31 ±0.02 |
| Stainless steel 316L | −0.300 [−0.300] | 0.24 | (0.27 ±0.02) |

The first term on the right-hand side of the equation is the relative change in length of the isolated wire on cooling from the reaction temperature (923 K) to room temperature (293 K), which has been calculated using finite element modelling to be −0.63% for the EM-LMI wire [113]. The second term is the relative change in length of the wire that has been firmly attached to the spring at room temperature (by copper plating) and then cooled to 4 K (the thermal cycle due to soldering does not affect the strain state of the wire). A simple 1D "force balance" equation [90] gives values for the relative change in length of the wire between 293 and 4 K that are within ~1% of the thermal expansion of the spring material (compare Tables 3.2 and 3.5), due to the small cross-sectional area of the wire in relation to the spring. Similar values are obtained from FEA, although there are somewhat larger differences for the Ti-6Al-4V tee-shaped spring, where the average contraction of the wire is 5% higher than the thermal contraction of Ti-6Al-4V (see Table 3.5). The third term on the right-hand side of Equation (3.5) is the intrinsic thermal expansion of $Nb_3Sn$ between 923 and 4 K, for which a value of −0.69% has been used (923–293 K: −0.53%, 293–4 K: −0.16%) [70]. Table 3.5 shows the values of $\varepsilon_M$

calculated using Equation (3.5), which show good agreement with the experimentally measured values for the different spring materials.

Various studies have been carried out of the three-dimensional strain-state of the filaments in $Nb_3Sn$ wires [122-127]. Given the uncertainties in some of the parameters used in Equation (3.5), our results are consistent with models in which the peak in the superconducting properties occurs when the deviatoric strain or the axial strain in the filaments is a minimum (zero). In any case, the FEA confirms that after cool-down, the 3D strain-state of the (EM-LMI) wire attached to the spring is, to a good approximation, equal to the strain-state of an isolated wire that is first cooled down and then subject to an axial strain. This equivalence between the thermal strains and the applied (mechanical) strains provides an explanation for the universal behaviour of the wires as a function of intrinsic strain (see Section 3.3.2). This is due to the line-like contact between the wire and the spring. Note that this is not the case for tape conductors, where the differential thermal contraction also leads to an in-plane transverse strain on the tape [128] (or for a wire attached to the spring with large amounts of copper-plating or solder).
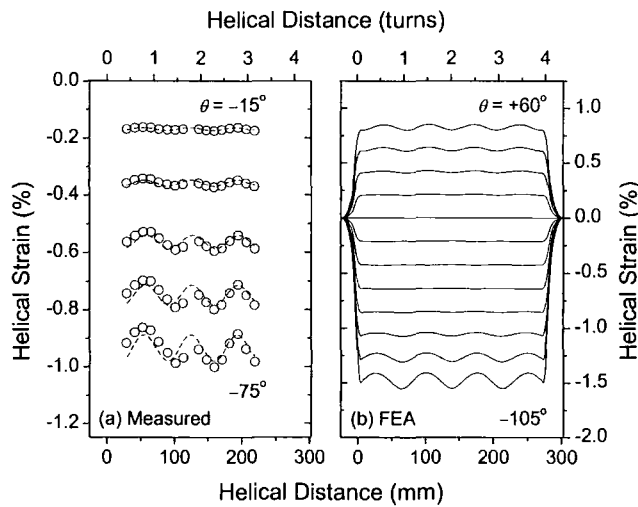


**Figure 3.13.** The helical strain at the outer surface of a Cu-Be rectangular spring (with four turns) as a function of helical distance: (a) results from strain-gauge measurements (the symbols show the measured data while the dashed lines are a guide to the eye); (b) FEA results

**Table 3.6.** The amplitude of the longitudinal strain oscillations for springs of different materials and geometries.

| Spring material and geometry | Amplitude of oscillations (%) | |
|---|---|---|
| | −1.0% strain | +0.5% strain |
| Rectangular ($N = 4$) | | |
| Cu-Be (meas.) | 5 | — |
| Cu-Be (FEA) | 1.3 | 2.5 |
| Brass (FEA) | 3.9 | 3.6 |
| Tee-shaped (FEA) | | |
| Cu-Be ($N = 4.5$) | 1.4 | 0.7 |
| Cu-Be ($N = 2, 3, 4, 5, 6$) | 2.6, 0.1, 0.25, 0.3, 0.35 | — |

### 3.4.3 Strain uniformity along the wire's length

In order to investigate the uniformity of the strain along the length of the wire, measurements were carried out using 16 strain gauges placed around the outer surface of a Cu-Be rectangular spring. A sinusoidal variation of strain with helical distance was observed, as shown in Figure 3.13(a). The results obtained from the finite element analysis are shown in Figure 3.13(b). The measured "oscillations" have a similar wavelength to the FEA results (equal to one turn) but are both considerably larger and off-set spatially. At a mean applied strain of −1%, the measured value for the amplitude is ~5% of the mean, compared to the FEA value of 1.3% (see Table 3.6).

Finite element analysis was used to investigate the strain variations for various types of spring over extended strain ranges. The size of the oscillations generally increases non-linearly with increasing strain, and for the Cu-Be rectangular spring is considerably larger at tensile strains than equivalent compressive strains, as shown in Figure 3.13(b). For the Cu-Be tee-shaped spring with four-and-a-half turns (used for the critical current measurements), the oscillations have a similar size to the rectangular spring in compression but are smaller in tension (see Table 3.6). At a mean applied strain of
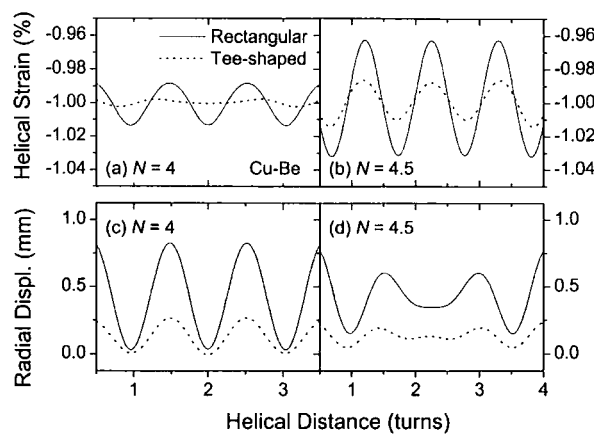
**Figure 3.14.** The helical strain and radial displacement at the outer surface of springs with 4 and 4.5 turns as a function of helical distance (results from FEA).
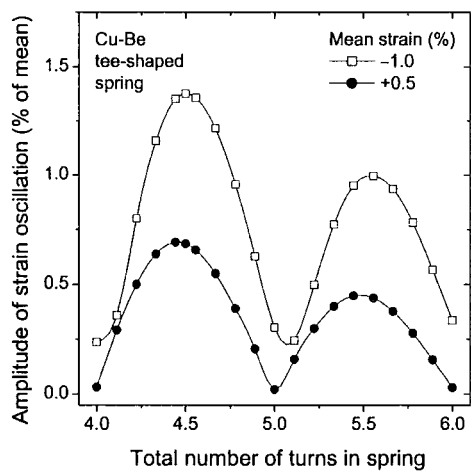


**Figure 3.15.** The amplitude of the longitudinal strain oscillation at −1% and +0.5% mean strain at the outer surface of a Cu-Be tee-shaped spring as a function of the total number of turns in the spring (results from FEA).

+0.5%, the predicted amplitude of the strain oscillations corresponds to a maximum variation in the critical current of approximately ±0.6 A for the EM-LMI and Vac wires at 4.2 K and 12 T (see Figure 3.10). Tee-shaped springs with integer number of turns ($N = 4$, 5 or 6) have considerably smaller oscillations, by a factor of ~5 at −1% strain, than the ($N = 4$) rectangular spring and the half-integer ($N = 4.5$) tee-shaped spring.

Finite element analysis shows that the strain oscillations are related to the distortion of the envelope of the turns that occurs when the spring is twisted. For springs with integer numbers of turns, a correlation is observed between strain magnitude and radial displacement as a function of helical distance [see Figures 3.14(a) and (c)], although for springs with half-integer number of turns, there is no simple correlation [Figures 3.14(b) and (d)]. The behaviour is clearly quite complex, and, to our knowledge, an analytic description is not yet available. The smaller oscillations for the tee-shaped springs can be attributed to the greater torsional rigidity of the cross-section and hence smaller distortions. Figure 3.15 shows how the oscillation amplitude varies as a function of the total number of turns in the Cu-Be tee-shaped spring at +0.5% and −1.0% strain. It can be seen that for this type of spring an integer number of turns (4 or 5) is indeed the optimum number for minimising the oscillations.

It was also found that the longitudinal oscillations are considerably larger when the spring material is in the plastic regime (presumably because the spring yields first at the peaks of the oscillations which therefore increase disproportionally). For example, a finite element model of a (brass) spring with an elastic limit of 0.4% (rather than 1.0% for Cu-Be) has oscillations that are larger by a factor of ~3 at −1% applied strain (see Table 3.6). Hence the difference between the experimental results and the FEA in Figure 3.13 may be partly due to the copper-beryllium used for the spring having a lower elastic limit than the typical value at room temperature (0.9%).

# 3.5 Discussion of spring design

Our experimental and FEA results allow us to make some recommendations about optimum spring designs. The universal relations between superconducting properties and intrinsic strain for wires on different spring materials demonstrate that the thermal expansion of the spring only affects the behaviour of wires through a change in the parameter $\varepsilon_M$. However, it is important to use a spring material with a high elastic limit—such as Cu-Be (TH04 temper) or Ti-6Al-4V—given the requirement for a reversible (unique) relationship between angular displacement and strain, the deviations observed for the $J_C$ measurements on the stainless-steel spring, and the increase in the size of the longitudinal strain variations predicted by the FEA for springs in the plastic regime. We now prefer to use the titanium alloy, as it is routinely used for sample-holders in standard $J_C$ measurements [105, 129] and it has the highest elastic limit at 4.2 K of any engineering alloy (we have also used copper-beryllium, but the sensitivity to heat-treatment conditions and the toxicity of the beryllium means that some care is required when handling). Although Ti-6Al-4V cannot easily be soldered to or copper-plated directly, we have used a well-established technique for nickel plating the spring [130] prior to transferring and attaching the wire using copper-plating and soldering.

The $J_C$ data demonstrate that it is necessary to use finite element analysis (or the loaded-beam equations) to relate the strain-gauge calibration data to the strain at the midpoint of the conductor. After applying the correction to obtain the strain at the middle of the wire, second-order effects due to the different strain gradients for the two spring geometries are not observed for our results. The magnitude of the strain gradient may be important for larger or different types of conductor, and can be reduced by using a spring with a radially thicker, tee-shaped cross-section (our optimised tee-shaped springs have strain gradients and correction factors of <3%). As the radial thickness of the spring is increased, the ratio of the strain at the inside of the spring to the strain at the outside

increases in magnitude, reducing the strain range over which the spring remains elastic. Walters *et al.* suggested maximising the elastic strain range by setting this ratio to be equal to −1 [66]. We have used an alternative approach in which the value of the inner/outer strain ratio is specified by the strain range over which measurements are required, and then the tee shape is optimised to minimise the strain gradient across the conductor. Our specific requirements are for detailed measurements to ±0.5% applied strain and hence for a spring material with an elastic limit of ~1% we use an inner/outer strain ratio of −2. To optimise the properties of the spring, the loaded-beam equations given by Walters *et al.* can be used (see Section 3.4.1.1), as these predict a radial-dependence for the strain in the turns that agrees well with the FEA [66]. The first stage of the process is the same as that described by Walters *et al.* and involves maximising the outer radius of the spring (given the available space), minimising the width at the outside of the tee (given the width of the conductor), and maximising the width at the inside of the tee (given the maximum pitch-angle for the wire of ~5° [95] and hence the turn pitch) [66]. The two parameters to be calculated are then the inner radius and the position of the ramped step (see Figure 3.1). For any given value of inner radius there is an optimum step position that minimises the neutral radius [calculated using Equation (3.4)] and hence minimises both the strain gradient across the conductor and the size of the inner/outer strain ratio [Equation (3.2)]. The optimum step position can be calculated at discrete values of inner radius using a spreadsheet solver/optimiser. Hence the optimum inner radius and ramped step position are uniquely determined once the inner/outer strain ratio is specified by the required elastic strain range.

The geometry of the tee-shaped spring used in our measurements [see Figure 3.1(b)] was obtained using the method described above with an inner/outer strain ratio of −2. For this spring, the loaded-beam equations predict a strain gradient across a ⌀0.81 mm wire of ±2.1% (FEA: ±2.9%) compared to the value of approximately ±6% that would be

obtained using the approach of Walters *et al*. The reversibility of the critical current density and strain-gauge calibration data also imply that measurements can generally be carried out on a single cycle to a value of compressive strain beyond the predicted elastic regime (by a factor of ~2). In general, the availability of a larger bore diameter enables both a larger strain range and a smaller strain gradient across the conductor.

The design should also consider the torque required to twist the spring, which can also be calculated using the loaded-beam equations, so that higher-strength shafts are used for springs with radially thicker turns [66, 93]. The FEA results for the tee-shaped spring also show that the calibration factor is quite strongly dependent (~5%) on whether the height of the spring is able to change. Our probe is designed with a sliding keyway so that the change in height can occur freely (or, at least, reproducibly).

Finite element analysis shows that the uniformity of the strain along the length of the wire varies quite considerably with spring material and geometry. These longitudinal strain variations can be large, but our FEA results show that they can be reduced to <0.5% by using a spring with an optimum integer number of turns (4 or 5).

# 3.6 Conclusions

Variable-strain critical current density data and finite element analysis results are presented for $Nb_3Sn$ wires on helical (Walters) springs of different materials and geometries. The strains produced by these springs can in principle be much more complex than those produced by axial pull techniques. For wires measured on different spring materials (Cu-Be, Ti-6Al-4V, brass, SS 316L), the critical current density, *n*-value, and effective upper critical field are universal functions of intrinsic strain— deviations are observed for the stainless-steel spring which are attributed to plasticity. The experimental and modelling results demonstrate that the thermal strains due to the

spring are predominantly axial in nature, so that the only effect on the behaviour of the wire is a change in the parameter $\varepsilon_M$, which depends systematically on the thermal expansion of the spring material. The variable-strain data obtained on different spring geometries show good agreement when the applied strain is calculated at the midpoint of the wire using strain-gauge calibration data corrected to account for the strain gradient across the wire (and the presence of the wire on the spring). The agreement is observed even though the transverse strain gradient for the rectangular-shaped spring used in our measurements is considerably larger than for the tee-shaped spring. The correction factors can be obtained from FEA or analytical calculations. Experimental results show that the critical current density is uniform along the length of the wire typically to within ±2%. Finite element analysis shows that the variations in strain along the length of the wire vary considerably with spring material and geometry, but are generally less than ±2% for our measurements. The universal strain dependences observed for different types of helical spring provide good evidence that the intrinsic properties of the conductor can be accurately measured—the capacity for very high-field and high-sensitivity measurements is also demonstrated. Supplementing previous work by Walters *et al.*, springs made with highly elastic materials (e.g. Ti-6Al-4V), optimised tee-shaped cross-sections, and optimum integer numbers of turns (e.g. 4 or 5) are shown to give the best performance in relation to the transverse and longitudinal strain uniformity in the wire.

---

*Effect of axial strain cycling on the critical current density and n-value of ITER niobium-tin wires*

## 4.1 Introduction

Strain has a very large effect on the superconducting properties of $Nb_3Sn$. In superconducting magnets, strain arises from the differential thermal contraction that occurs on cooling to cryogenic temperatures, and the Lorentz-forces that occur during high-field operation. The International Thermonuclear Experimental Reactor (ITER) will use magnets made from cable-in-conduit conductors (CICC's) with $Nb_3Sn$ strands (wires) [76]. For these large-scale high-field magnets, knowledge of the effects of strain is extremely important. In addition, the ITER magnets will undergo many charging cycles (up to 50 000), and so the effects of cyclic strain and fatigue also need to be considered.

The axial strain dependence of the critical current density [61, 62, 131] (and *n*-value [101]) of technical $Nb_3Sn$ wires has been measured extensively. The effects are generally found to be reversible, to first order, for small numbers of cycles over quite large ranges of strain, while at higher strains damage occurs to the superconducting filaments. However, the effects of large numbers of strain cycles within the so-called reversible regime has not been widely investigated. A study of bronze-route $Nb_3Sn$ wires stress cycled at room-temperature did not observe fatigue effects [132], nor did a study of CICC's subject to axial strain cycles at cryogenic temperatures [73]. In contrast,

**Figure 4.1.** The top end of the strain probe, with the computer-controlled stepper motor (on the left).

investigations of transverse stress cycling of CICC's [133] and cyclic charging of ITER model coils [76] have found some evidence of fatigue effects and in order to understand these results, accurate data for the component wires are required. The work presented in this chapter (and associated paper [116]) is the first reported investigation of the effects of axial strain cycling (involving >1000 cycles) at cryogenic temperatures on the critical current density and *n*-value of technical $Nb_3Sn$ wires.

## 4.2 Experimental

Measurements were made on two different $\varnothing 0.81$ mm ITER-candidate $Nb_3Sn$ wires: an internal-tin wire made by Europa Metalli-LMI (EM-LMI) and a bronze-route wire made by Vacuumschmelze (Vac). The heat-treatment schedules and mounting procedures were as described in Chapter 3. The springs were made of copper-beryllium, with tee-shaped cross-sections designed to minimise the strain gradient across the wire. The strains values quoted are for the midpoint of the wire, calculated from the strain-gauge calibration data using finite element analysis (see Chapter 3).
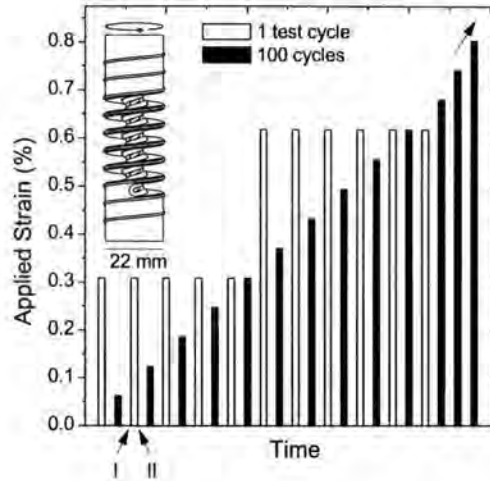
**Figure 4.2.** The strain cycling procedure. The labels I and II refer to the measurements at zero applied strain at the beginning and the end of each test cycle respectively. Inset: spring sample holder with tee-shaped cross-section.

The experiments were carried out using our strain probe [93] with an added computer-controlled stepper motor (see Figure 4.1). This enables strains (and strain cycles) to be applied automatically, with a resolution of ~$10^{-6}$ % strain per step. Standard voltage–current ($V$–$I$) measurements were made on three different sections of the wire, which was immersed in a liquid-helium bath at 4.2 K (see Chapter 3). The experiments consisted of single strain-cycles during which $V$–$I$ measurements were made (test cycles), alternated with sets of 100 strain cycles (see Figure 4.2). The maximum applied strain was increased for each successive set of 100 cycles in increments of 0.062% until the wire was damaged. The test cycles were first carried out to 0.31% applied strain and after the set of 100 cycles to 0.31% had been completed, they were then carried out to 0.62%. $V$–$I$ measurements were made at magnetic fields between 9 and 15 T at zero applied strain at the beginning of the test cycle, at 10 and 12 T during the first half of the cycle and then at 10 and 12 T at zero applied strain at the end of the cycle. No test cycles were carried out after sets of cycles to applied strains above 0.62%, but measurements

were made at 10 and 12 T during the 100th cycle, at the maximum applied strain and at zero applied strain. The strain was changed at a constant maximum speed of 0.01% s[-1] (e.g. cycles to 0.31% took ~90 s). In addition, the temperature of the wire was kept below ~20 K for the entire experiment (the Vac wire was subjected to a thermal cycle to room temperature after strain cycling to 0.61%, but this had no significant effect).

## 4.3 Results

Figure 4.3 shows the electric field–engineering current density ($E$–$J$) characteristics for the three different sections of the EM-LMI wire (A, B, and C) at zero applied strain before any cycling. $E$ and $J$ were calculated from the voltage and current by dividing by the voltage-tap separation (typically ~20 mm) and the cross-sectional area of the wire ($5.15 \times 10^{-7}$ m²). The data are typical of both wires, which were homogeneous in terms of their $E$–$J$ characteristics to within 5% (until damage occurred). This chapter will consider engineering critical current densities ($J_C$) defined at an electric-field criterion of
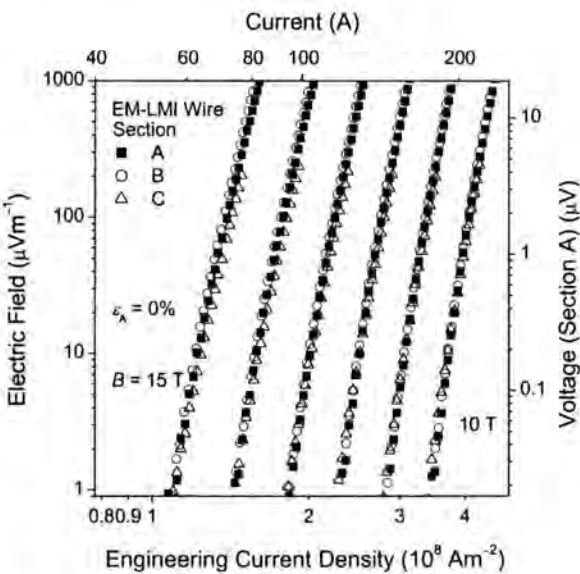


**Figure 4.3.** Electric field versus engineering current density (and voltage versus current) on a log-log scale for three different sections of the EM-LMI wire at zero applied strain (before any cycling) and integer magnetic fields between 10 and 15 T.

**Figure 4.4.** (a) Engineering critical current density (and critical current) and (b) *n*-value as a function of applied strain for section A of the EM-LMI wire at a magnetic field of 12 T, measured after each set of 100 strain cycles. The engineering critical current density was defined at 10 $\mu$Vm$^{-1}$, and the *n*-value was calculated for the electric field range 10–100 $\mu$Vm$^{-1}$.



**Figure 4.5.** (a) Engineering critical current density and (b) *n*-value for three different sections of the EM-LMI wire at zero applied strain and a magnetic field of 12 T, plotted as a function of the maximum applied strain for the previous 100 cycles. Data are shown at the beginning (I) and at the end (II) of the single test-cycles. Insets: data (I) for all applied strains.

$10 \, \mu\text{Vm}^{-1}$ and *n*-values calculated using $E \propto J^n$ for the electric-field range $10\text{-}100 \, \mu\text{Vm}^{-1}$. $J_C$ and *n* clearly depend on the choice of criterion (e.g. *n* typically varies by 50% in the experimentally accessible electric-field range $1\text{-}1000 \, \mu\text{Vm}^{-1}$, decreasing with increasing *E*), but the trends described below do not depend on this choice.

## 4.3.1 EM-LMI wire

Figure 4.4 shows the engineering critical current density and *n*-value for the EM-LMI wire as a function of applied strain ($\varepsilon_A$), measured after each set of 100 strain cycles. Data are shown for one section of the wire (A) at a magnetic field of 12 T, but the same trends were observed for the other sections and at 10 T. Figure 4.5 shows the $J_C$ and *n* data at zero applied strain and 12 T, measured after each set of 100 strain cycles before and after each test cycle. The first test-cycle to 0.31% applied strain caused a 1% decrease in $J_C$ at $\varepsilon_A = 0\%$ for all three sections of the wire (for *n*, the experimental errors are too large to observe changes of this magnitude). For subsequent cycles to applied strains up to and including 0.31% (~500 cycles in total), the data were reversible to within the experimental error. In this regime, $J_C$ and *n* are a maximum at $\varepsilon_A = \varepsilon_M = 0.28\%$ with values of $2.95 \times 10^8 \, \text{Am}^{-2}$ (152 A) and 24.5 respectively. The first test-cycle to $\varepsilon_A = 0.61\%$ caused $J_C$ at zero applied strain to increase by ~2%. At low applied strains (≤0.25%) $J_C$ (and *n*) were then unaffected by the subsequent ~500 cycles to applied strains between 0.37% and 0.62%. However, at high applied strains (≥0.25%) these multiple cycles caused $J_C$ and *n* to increase after each successive set of cycles (approximately monotonically), resulting in a final increase in $J_C$ at $\varepsilon_A = \varepsilon_M$ of 5% as well as a small increase in $\varepsilon_M$ itself to 0.32%. The increases were proportionally larger at higher applied strains (~14% at $\varepsilon_A = 0.61\%$). Cycling to $\varepsilon_A = 0.74\%$ caused $J_C$ at zero applied strain to increase by a further 2.5% (no test cycle was carried out). Finally,

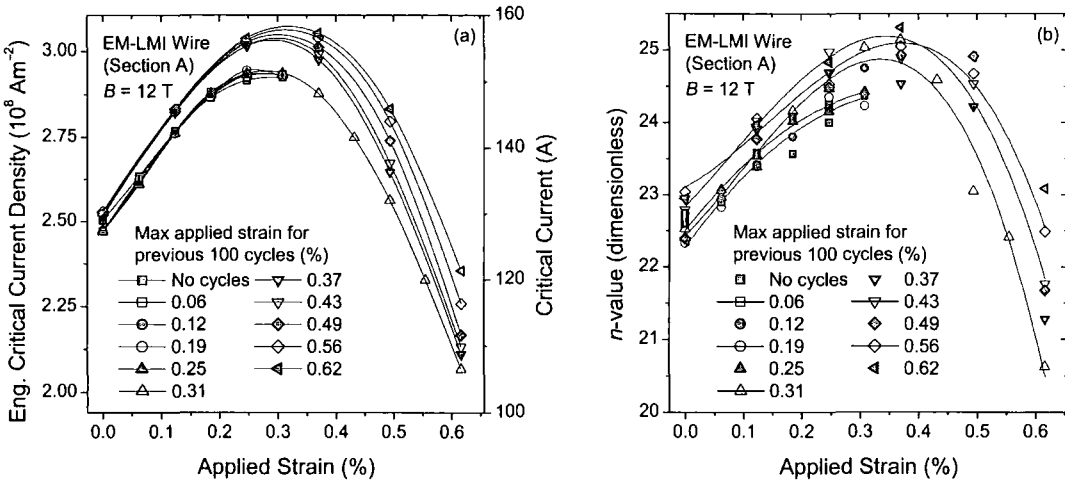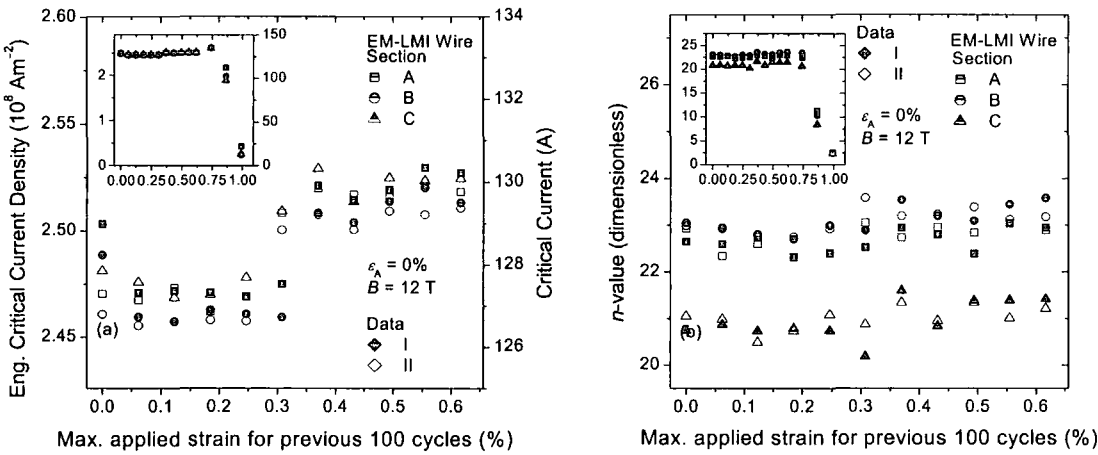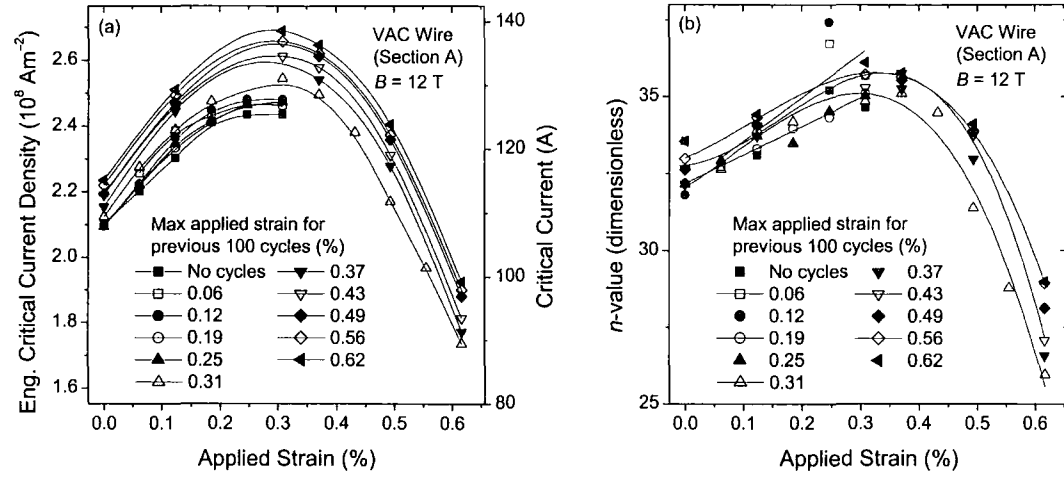**Figure 4.6.** (a) Engineering critical current density and (b) *n*-value as a function of applied strain for section A of the Vac wire at a magnetic field of 12 T, measured after each set of 100 strain cycles. The engineering critical current density was defined at 10 $\mu Vm^{-1}$, and the *n*-value was calculated for the electric field range 10–100 $\mu Vm^{-1}$.
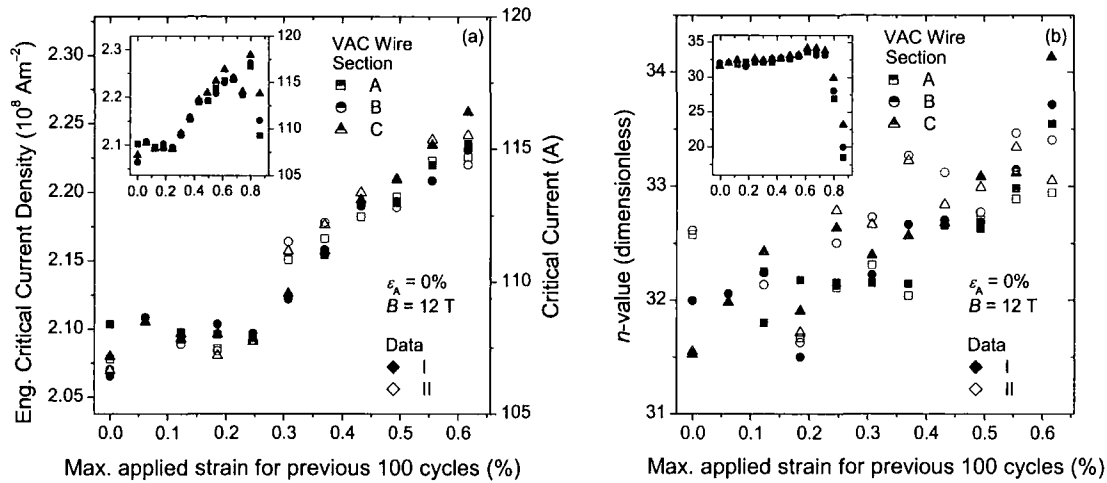


**Figure 4.7.** (a) Engineering critical current density and (b) *n*-value for three different sections of the Vac wire at zero applied strain and a magnetic field of 12 T, plotted as a function of the maximum applied strain for the previous 100 cycles. Data are shown at the beginning (I) and at the end (II) of the single test-cycles. Insets: data (I) for all applied strains.
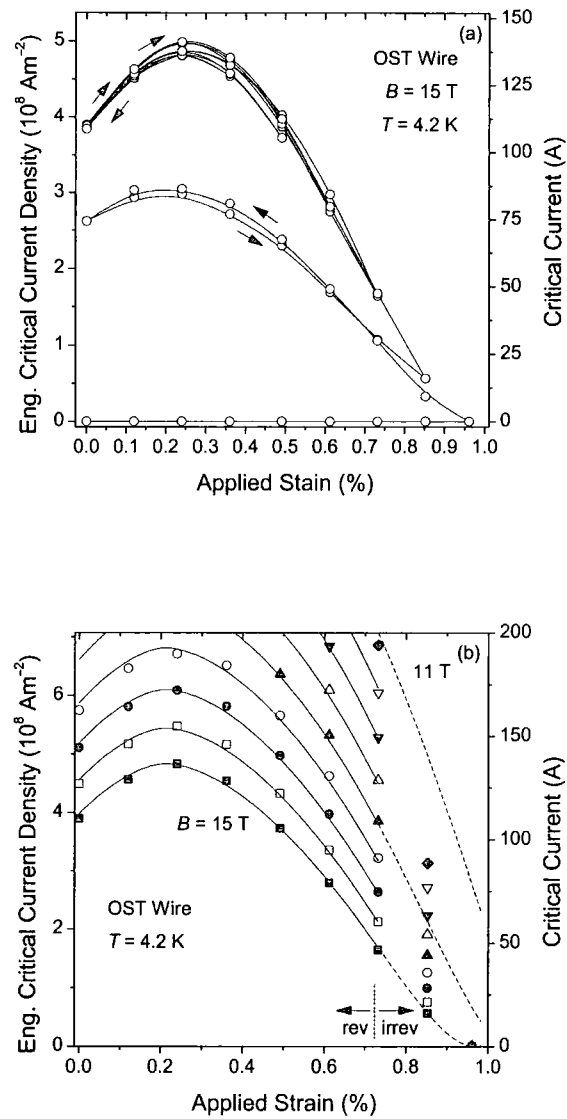
**Figure 4.8.** A limited dataset for a jellyroll $Nb_3Sn$ wire. Engineering critical current density (and critical current) as a function of applied strain at 4.2 K: (a) at a magnetic field of 15 T as the strain is cycled to successively higher peak values, and (b) at magnetic fields between 11 T and 15 T at the peak strain of each cycle.

cycling to $\varepsilon_A = 0.86\%$ caused $J_C$ and $n$ at zero applied strain to reduce by 15% and 50% respectively, indicating damage to the wire. Further damage occurred after cycling to $\varepsilon_A = 0.99\%$.

## 4.3.2 Vac wire

Equivalent data for the Vac wire are shown in Figures 4.6 and 4.7. The scatter on the data is generally larger, but $J_C$ and $n$ are again reversible to within the experimental error for cycles to applied strains up to 0.31% (no irreversible effect due to the first cycle was observed for this wire). In this case $J_C = 2.5 \times 10^8$ Am$^{-2}$ (128 A) and $n = 35$ at $\varepsilon_A = \varepsilon_M = 0.29\%$ and 12 T. $J_C$ and $n$ again increased after each successive set of cycles to applied strains between 0.37% and 0.62%, with $J_C$ at $\varepsilon_A = \varepsilon_M$ and 12 T increasing by 7% in total. This was similar to the EM-LMI wire, except that at low applied strains ($\leq 0.12\%$) larger increases occurred ($J_C$ increased by 6% in total at zero applied strain) and there was no indication of a change in $\varepsilon_M$. Evidence of damage from the $J_C$ data was first observed after cycling to $\varepsilon_A = 0.86\%$, although $n$ also decreased considerably (by 25%) after cycling to $\varepsilon_A = 0.80\%$.

## 4.3.3 A limited dataset for a jellyroll Nb₃Sn wire

Some critical current density and $n$-value measurements were also carried out on a jellyroll Nb₃Sn wire as a function of magnetic field and tensile strain at 4.2 K [13, 117]. This experiment was addressed primarily at finding the strain at which filament breakage occurs, and involved cycling the strain to successively higher peak values. The measurements were found to be reversible to within 5% for cycles up to 0.73% applied strain (0.52% intrinsic strain), while the wire was irreversibly damaged at higher strains (see Figure 4.8).

## 4.4 Discussion

For engineering purposes, it may be sufficient to know that there were no decreases in the critical current density or $n$-value for either wire during the >1000 strain cycles to applied strains up to 0.74%. Nevertheless, significant *increases* in the critical current density and $n$-value did occur as a result of strain cycling to applied strains between 0.37% and 0.74%. In fact, the increases in $J_C$ are associated with increases in the effective upper critical field (Kramer plots not shown), while increases in $n$ are broadly related to increases in $J_C$. The brittle $Nb_3Sn$ filaments behave elastically until damage (cracking) occurs at values of intrinsic strain in the range 0.3%–0.6% for most wires (compared to ~0.45% in this work), where intrinsic strain is, by convention, taken to be zero where $J_C$ is a maximum [134]. The changes in $J_C$ and $n$ are therefore likely to be caused by changes in the strain-state of the $Nb_3Sn$ filaments. The copper and bronze matrix materials have elastic limits of ~0.1% and ~0.2% respectively (and are in thermal pretension at zero applied strain), and so will be plastically deformed during strain cycling [134].

In general, loading-unloading treatments on wires can be carried out to reduce the axial thermal prestrain on the filaments [132]. In our experiment, however, the axial strain is directly controlled and therefore the changes in $J_C$ and $n$ observed during cycling can only be explained by also considering the non-axial strains. The effects of tensorial strains on $Nb_3Sn$ are not fully understood, although the consensus is that increases in either deviatoric or hydrostatic strain cause the superconducting parameters to decrease, with the deviatoric strain (related to the change in shape) having the larger effect [62, 123]. This suggests that the increases in $J_C$ and $n$ are due to a decrease in one or both of these quantities, although in simple models of wires, if deviatoric strain alone is considered then this is always zero at $\varepsilon_M$ (and $J_C$ at $\varepsilon_M$ is always the same). Detailed knowledge of the complex effects associated with plastic deformation and work

hardening of the components of the matrix requires finite element analysis modelling, which is in progress.

## 4.5 Conclusions

The results of our measurements of the effect of axial strain cycling on two ITER candidate $Nb_3Sn$ wires (EM-LMI and Vac) can be summarised as follows:

1.   Both wires were unaffected by the ~500 strain cycles to applied strains up to 0.31% (apart from a 1% decrease in the critical current density caused by the first test-cycle for the EM-LMI wire).

2.   The first test-cycle to 0.62% caused a 1–2% increase in the critical current density at zero applied strain (for the EM-LMI wire, this was the only increase in the zero applied strain data during the first ~1000 cycles).

3.   The ~500 strain cycles to applied strains between 0.37% and 0.62% caused the critical current density and *n*-value to incrementally increase at all applied strains; the final increases were proportionally larger at higher strains and varied from 2% to 14% (EM-LMI wire) and 6% to 11% (Vac wire).

4.   Cycling to applied strains above 0.74% (~0.45% intrinsic strain) caused large irreversible decreases in the critical current density and *n*-value.

*The scaling law for the strain-dependence of the critical current density in Nb₃Sn superconducting wires*

## 5.1 Introduction

Nb₃Sn superconducting wires, which are used in almost all high-field superconducting magnets operating above 12 T [13], have a critical current density ($J_c$) that depends on the magnetic field ($B$), the temperature ($T$), and the strain-state ($\varepsilon$) of the superconductor [62, 75]. The importance of magnetic field and temperature in the performance of small magnets is well established. Understanding the effect of strain—which occurs due to thermal contraction and magnetic forces—is becoming increasingly important, motivated by the International Thermonuclear Experimental Reactor (ITER) project in which very large-scale superconducting magnets will be used to inductively heat and confine a plasma for fusion [135]. As part of the research and development for ITER, two model coils have been built using Nb₃Sn cable-in-conduit conductors (CICC's) and tested at elevated temperatures (> 4.2 K). These are the Toroidal Field Model Coil (TFMC), with EM-LMI internal-tin Nb₃Sn wires in a stainless-steel jacketed cable, and the Central Solenoid Model Coil (CSMC), with Vacuumschmelze bronze-route Nb₃Sn wires in an Incoloy-908 jacketed cable [76]. In these magnets, the differential thermal contraction during cool-down causes intrinsic axial strains on the Nb₃Sn filaments of approximately −0.65% (compression) for the TFMC [104] and −0.3%

for the CSMC [136], while the magnetic (operating) strains are ~0.1% (tension) [76]. $J_C(B)$ measurements on the EM-LMI and Vac wires have been performed at a temperature of 4.2 K and zero applied strain [137, 138], as a function of temperature at zero applied strain [105, 129], as a function of axial strain at 4.2 K [73, 116, 139], and as a function of axial strain and temperature [62, 105, 140]. In this chapter (and associated paper [67]), we present the results of comprehensive, high-sensitivity ($10 \, \mu Vm^{-1}$) measurements of $J_C(B,T,\varepsilon)$ for both of the wires used in the model coil tests. These results are being used to assess the extent to which the model coils reached their short-sample specification [76, 136, 141].

$J_C(B,T,\varepsilon)$ data are parameterised using scaling laws, which allow the interpolation and extrapolation of the measured data for interlaboratory comparisons and magnet design. A number of different empirical scaling laws have been proposed to describe the magnetic field, temperature, and axial strain-dependence of $J_C$ in Nb$_3$Sn wires. These scaling laws generally incorporate aspects of the temperature scaling law of Fietz and Webb [47] (with subsequent refinements [142]) and the strain scaling law of Ekin [61]. The latter followed from the well-known measurements [61] of $J_C$ for a number of technological Nb$_3$Sn wires as a function of magnetic field and axial strain at 4.2 K (previous variable-strain measurements were also reported by a number of authors [68, 71, 143-147]). Both scaling laws relate changes in $J_C$ to changes in the upper critical field ($B_{C2}$), although a fundamental inconsistency implies that an additional strain-dependent parameter is required in order to unify the two laws [63, 71]. Summers *et al.* [148] subsequently proposed such a unified scaling law, which also includes Ekin's universal relation for the normalised values of $B_{C2}(4.2 \, K, \varepsilon)$ for binary Nb$_3$Sn wires, and a power-law relationship between $B_{C2}(4.2 \, K, \varepsilon)$ and $T_C(\varepsilon)$ (the critical temperature) [61]. The Summers Scaling Law parameterised the data available at the time quite accurately (although detailed variable-temperature-and-strain $J_C$ data had not yet been

reported) and was subsequently adopted as the standard formulae for large-scale magnet design [149]. Although the strains in magnets are three-dimensional in nature, there is now reasonable consensus (despite some conflicting results in the literature on the effect of transverse stress) that in the reversible strain regime, uniaxial (deviatoric) strain—whether applied in the axial or transverse direction—is the most important strain component; its effects in $Nb_3Sn$ are approximately an order-of-magnitude larger than hydrostatic strain [122, 123, 150-153].

More recently a number of laboratories have succeeded in obtaining $J_C(B,T,\varepsilon)$ data, and various alternative scaling laws have been proposed [62, 63, 75, 78, 105, 122]. In Durham, a general scaling law for $J_C(B,T,\varepsilon)$, the Interpolative Scaling Law (ISL), has been shown to allow very accurate parameterisations of comprehensive data for $Nb_3Al$ and $Nb_3Sn$ wires [75, 78]. The Interpolative Scaling Law uses general polynomial functions for the strain-dependent parameters, in contrast to the Summers Scaling Law. It therefore contains a relatively large number of free parameters and cannot generally be used to extrapolate beyond the measured regions of parameter space (e.g. the measured strain range). It is desirable, particularly for engineering purposes, to develop a scaling law with fewer free parameters that can be determined from a smaller $J_C(B,T,\varepsilon)$ dataset, allowing accurate predictions for $J_C$ to be made in other regions of parameter space. In this chapter, we develop such a scaling law based on a theoretical analysis of the effect of strain using microscopic theory and a review of the extensive experimental data now available. In particular, we use microscopic theory [27, 35-37, 41, 80, 123] to analyse the relationship between $B_{C2}(0,\varepsilon)$ and $T_C(\varepsilon)$ (and the other strain-dependent parameters) and to help motivate the introduction of modified versions of the empirical power-law relations currently used [62, 148]. A comparison of our theoretical and experimental results also allow us to address the important question of whether the variations of the superconducting properties of $Nb_3Sn$ with uniaxial strain are

predominantly due to changes in the electronic or the phononic properties of the material [80, 123].

The chapter is structured as follows. In Section 5.2, the experimental techniques are briefly summarised. Sections 5.3 and 5.4 contain the main experimental results. Section 5.3 describes consistency tests and interlaboratory comparisons, and hence addresses how general and accurate are the data. Section 5.4 presents the $J_{\mathrm{C}}(B,T,\varepsilon)$ data for the EM-LMI and Vac wires. These data are parameterised using the Interpolative Scaling Law and comparisons are made with alternative scaling laws. In Section 5.5, the observed relationships between $B_{\mathrm{C2}}(0)$ and $T_{\mathrm{C}}$ are examined using microscopic theory. Finally, in Section 5.6, a new simplified Interpolative Scaling Law is presented and its accuracy in parameterising complete datasets and extrapolating from partial datasets is examined.

## 5.2 Experimental techniques

Measurements were made on two types of ITER-candidate $\varnothing 0.81$ mm $Nb_3Sn$ wire: two samples of the Europa Metalli-LMI internal-tin wire (billet 285-17) and three samples of the Vacuumschmelze bronze-route wire (billet 21). The wires were subject to standard heat treatments (see Section 3.2.2), and then etched in hydrochloric acid to remove the chromium plating, transferred to copper-beryllium spring sample-holders, and attached by copper-plating and soldering. The strain values quoted characterise the average strain in the wire. They are calculated using data from strain-gauge calibrations, with correction factors obtained from finite element analysis (and confirmed using analytical calculations) to account primarily for the strain gradient across the wire (see Chapter 3). The corrections depend on the spring geometry and, for the ITER-candidate wires, vary from ~2% (tee-shaped springs) to ~ 9% (rectangular springs). The voltage ($V$)

across a section of the wire (typical length: ~20 mm) was measured using a nanovolt amplifier and a digital voltmeter, with most of the measurements being made at constant temperature with a slowly-increasing current ($I$), although some additional measurements on the first EM-LMI sample were made at constant current with a slowly-increasing temperature.

Measurements at 4.2 K were made with the sample directly immersed in a liquid-helium bath, and at temperatures above 4.2 K with the sample located in a vacuum chamber containing a small quantity of helium gas. Above 4.2 K, the temperature was controlled using three independent controllers with Cernox thermometers and constantan wire heaters. For the EM-LMI wire, the central thermometer was placed directly on top of the wire and the other two thermometers placed on the sample holder next to the wire at both ends of the turns of the spring; for the Vac wire, all three thermometers were placed on the sample holder. The thermometers were calibrated commercially in zero magnetic field, while the central thermometer was also calibrated in-house in magnetic fields up to 15 T [78] and the small (~50 mK) corrections obtained from this were used for all three thermometers [154]. The heaters were situated, correspondingly, on both ends of the sample holder (between the turns of the wire), and around the central turns of the spring on the outside of an OFHC copper tube. Variable-temperature data obtained previously using our probe were found to agree well with data from another group [78, 155]. We note that in our experimental set-up, temperature control is more difficult when the temperature is being swept ($V$–$T$ measurements), although fairly smooth temperature sweeps were generally achieved.

Voltage–current and additional voltage–temperature measurements were made on the first EM-LMI sample, with particular emphasis given to obtaining data near the operating conditions for the TFMC. The experimental procedure was as follows: $V$–$I$ measurements were first made at 4.2 K at applied strains from 0.49% tension to −0.48%

compression and at integer values of magnetic field up to 15 T. The applied strain was then set to zero and the probe was warmed to room temperature so that thermometry, heaters, and a vacuum can could be fitted. The probe was then cooled back to 4.2 K and the applied strain was changed to $-0.48\%$ ($-0.76\%$ intrinsic strain) where *V–I* and *V–T* measurements were carried out. *V–I* measurements were made at 1 K increments between 5 and 13 K and at half-integer fields up to a maximum of 15 T. Additional *V–I* characteristics were also obtained at 0.1 K increments at various fields. *V–T* measurements were made with the current fixed at 111 A, 50 A, and 25 A at half-integer values of magnetic field, and also with a current of 0.5 A at 0, 3, 6, 9, and 12 T. *V–I* measurements were then made at a magnetic field of 12 T and 0.5 K temperature increments at applied strains from $-0.48\%$ to $0.61\%$ and then from $0.61\%$ to $-0.81\%$ (with some additional data obtained at 15 T). The second EM-LMI sample was measured in magnetic fields up to 23 T in a resistive magnet at the European high-field laboratory in Grenoble, where *V–I* data were obtained at a temperature of 4.2 K at applied strains between $+0.49\%$ and $-0.48\%$. For the Vac wire, *V–I* measurements were carried out at 4.2 K in fields up to 15 T (sample 1), at 8 K and 12 K in fields up to 15 T (sample 2), and at 4.2 K in fields up to 23 T in Grenoble (sample 3). There were no significant differences between the results for different samples of the same wire; for example, equivalent $J_c$ data at fields $\leq 15$ T obtained in Durham and Grenoble agree to within ~2%.

The chapter provides engineering critical current density ($J_c$) data calculated by dividing the critical current ($I_c$) by the total cross-sectional area of the wire ($5.153 \times 10^{-7} \, \text{m}^2$) and defined at an electric-field criterion of $10 \, \mu\text{Vm}^{-1}$. $J_c$ was calculated using the value of current in the superconducting material alone, obtained by subtracting the current in the normal shunt from the total current (for example, the typical

shunt resistance is ~5 μΩ at 6 T corresponding to a shunt current of 40 mA at 10 μVm$^{-1}$)

[78]. For the particular case of comparing the $E-T$ and $E-J$ characteristics, however, we

will refer to the total current as this is constant during the $E-T$ measurements (see

Section 5.3.2). Approximately 250 $J_C(B,T,\varepsilon)$ data points were used in the analysis for

the EM-LMI wire and ~800 data points were used for the Vac wire.
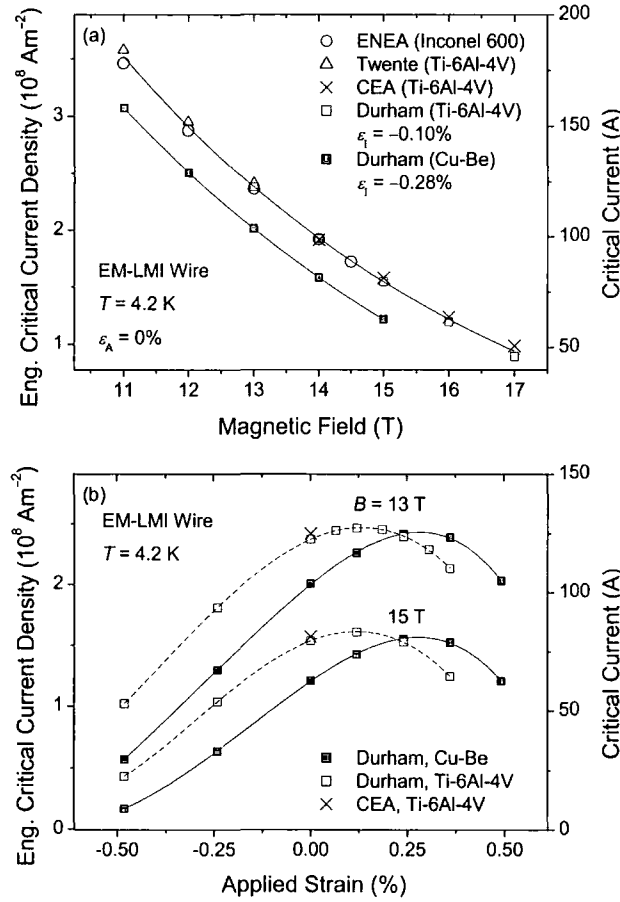


**Figure 5.1.** Interlaboratory comparisons for the EM-LMI wire: (a) Engineering critical current

density (and critical current) at 10 μVm$^{-1}$ as a function of magnetic field at 4.2 K and zero

applied strain. (b) Engineering critical current density as a function of applied strain at 4.2 K, and

13 and 15 T. The data were obtained in Durham on Cu-Be and Ti-6Al-4V springs and in other

laboratories on Ti-6Al-4V and Inconel-600 sample holders [129, 138, 140].

## 5.3 Consistency tests and interlaboratory comparisons

We will begin by presenting the results of various consistency tests and interlaboratory comparisons. These are vital given the complexities involved in making such measurements and the importance of the data for the ITER project, and enable the accuracy of the data to be addressed prior to comparison with theory.

### 5.3.1 Comparison with other $J_C$ data for as-prepared EM-LMI wires

Figure 5.1(a) shows the results of various measurements of the engineering critical current density of as-prepared EM-LMI wires as a function of magnetic field at 4.2 K [129, 138, 140]. In these (zero applied strain) measurements, the strain-state of the wire is determined primarily by the thermal expansion of the sample holder. It can be seen that the data from all of the laboratories agree to within ±2.5% for measurements on the same titanium alloy sample holder (as well as for an Inconel 600 sample holder) and hence show similar variations to those observed in the VAMAS international round-robin measurements [156]. Figure 5.1(b) shows our $J_C$ data measured as a function of applied strain ($\varepsilon_A$) at 4.2 K for EM-LMI wires mounted on a Cu-Be spring (used in this experiment) and a Ti-6Al-4V spring. These data superimpose to within ~5% if plotted as a function of intrinsic strain ($\varepsilon_I$), where intrinsic strain is defined relative to the applied strain where $J_C$ is a maximum ($\varepsilon_M$):

$$\varepsilon_I = \varepsilon_A - \varepsilon_M . \tag{5.1}$$

The values of $\varepsilon_M$ are ~0.28% for the Cu-Be spring and ~0.10% for the Ti-6Al-4V spring, which are consistent with the thermal strain on the filaments due to the cool-down from 293 K (where the wire is copper-plated to the spring) to 4.2 K being determined by the

thermal expansion of the spring material: −0.32% for Cu-Be and −0.17% for Ti-6Al-4V

[157]. Therefore, as long as both the applied strains and the thermal strains are properly

considered, the $J_C$ datasets obtained on springs of different materials and geometry are

consistent (see Chapter 3).

## 5.3.2 Comparison of *E−T* and *E−J* characteristics

In the ITER model coil tests, the electric field is measured as a function of

temperature (*E−T*) while keeping the current density fixed, and the temperature where

dissipation begins—the current-sharing temperature $T_{CS}$—is determined as a function of

current density and magnetic field. This method is used because *E−T* measurements are

easier to perform on the model coils than standard *E−J* measurements (electric field as a

function of current density), while at elevated temperatures the coils can be fully tested

(driven resistive) at values of current that do not generate strains outside the coil

operating range. For the TFMC (which uses EM-LMI wires), *E−T* measurements were
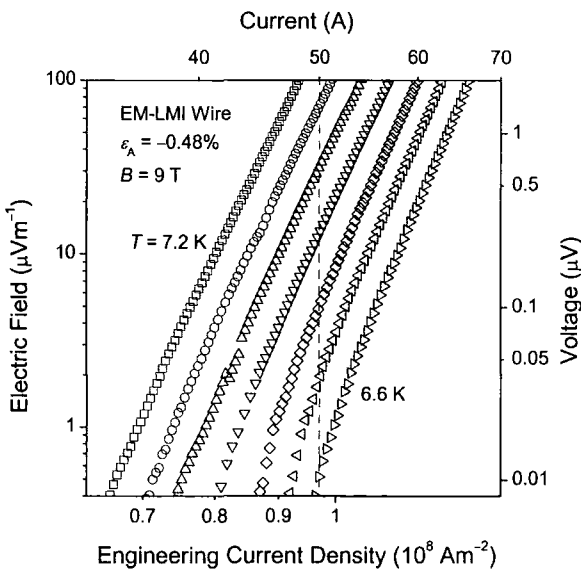


**Figure 5.2.** Log–log plot of electric field versus engineering current density (and voltage versus

current) for the EM-LMI wire at 9 T and at 0.1 K increments between 6.6 and 7.2 K. (The dashed

line is used for comparison with the *E−T* data, see Figure 5.3.)

performed with currents up to 80 kA (111 A per wire), magnetic fields up to ~9.5 T, and

temperatures between ~6 K and ~10 K [141, 158]. The $T_{CS}$ data are then compared with

measurements of $J_C$ for the component wires and the performance of the model coils

assessed [76, 104, 136, 141, 158]. The underlying assumption in these comparisons is

that although $J_C$ is not a thermodynamic property, the $E-T$ and $E-J$ characteristics of the

wires are completely equivalent—this assumption is addressed in this section.

Figure 5.2 shows the electric field–engineering current density ($E-J$) characteristics

for the EM-LMI wire at −0.48% applied strain (−0.76% intrinsic strain), at a magnetic
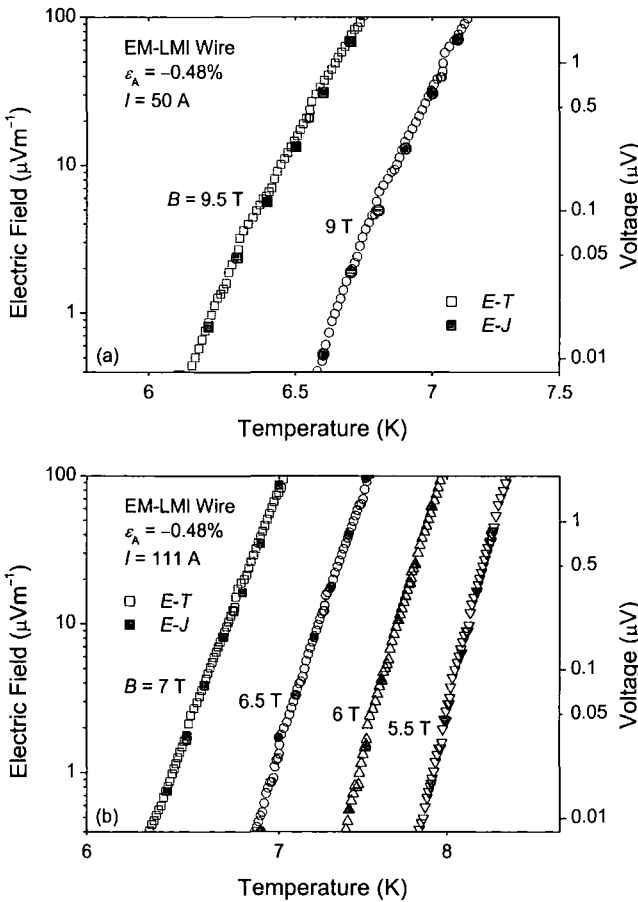


**Figure 5.3.** Log–log plot of electric field (and voltage) versus temperature: (a) for a constant total

current of 50 A at 9 and 9.5 T, and (b) for a current of 111 A at half-integer magnetic fields

between 5.5 and 7 T. The open symbols show the $E-T$ characteristics, while the closed symbols

show points extracted from the $E-J$ characteristics (e.g. on the dashed line in Figure 5.2).
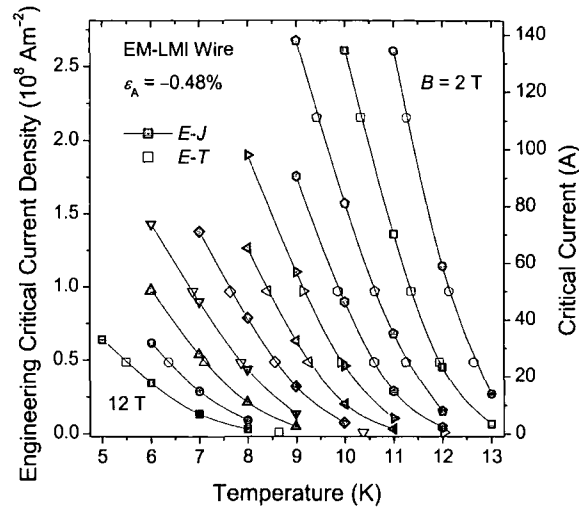
**Figure 5.4.** Engineering critical current density (and critical current) at 10 $\mu Vm^{-1}$ as a function of temperature at integer magnetic fields between 2 and 12 T. The closed symbols show $J_C$ obtained from the $E$–$J$ characteristics, while the open symbols show $J_C$ calculated from the $E$–$T$ characteristics.
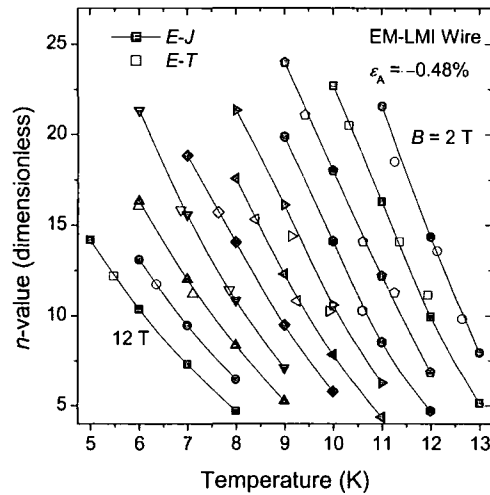


**Figure 5.5.** The $n$-value as a function of temperature at integer magnetic fields between 2 and 12 T. The closed symbols show $n$ obtained from the $E$–$J$ characteristics, while the open symbols show $n$ calculated from the $E$–$T$ characteristics. The $n$-values were calculated for electric fields between 10 and 100 $\mu Vm^{-1}$ using the total current (including the shunt current) and, as such, are typically ~0.75 lower than the shunt-subtracted $n$-values.

field of 9 T, and at 0.1 K temperature increments. The data can be parameterised by the standard power-law expression:

$$E(J,B,T,\varepsilon) = E_C \left[ J / J_C(B,T,\varepsilon) \right]^n,$$ (5.2)

where the $n$-value for the EM-LMI wire is approximately constant over one order of magnitude of electric field (at constant $B$, $T$, and $\varepsilon$), but decreases slowly with increasing electric field. Figure 5.3 shows the electric field–temperature ($E$–$T$) characteristics for a total current of 50 A and magnetic fields of 9 and 9.5 T, and a total current of 111 A and magnetic fields between 5.5 and 7 T. In order to compare the data obtained from the two different types of measurement, $E(J,B,T,\varepsilon)$ data points have been taken from the $E$–$J$ characteristics at a particular value of total current (dashed line in Figure 5.2) and plotted together with the $E$–$T$ characteristics: it can be seen that the data superimpose, with a typical uncertainty of ~20 mK. In addition, Figure 5.4 shows the engineering critical current density as a function of temperature, where $J_C$ has been calculated in the standard way from the $E$–$J$ characteristics at an electric-field criterion of 10 $\mu Vm^{-1}$, and $T_{CS}$ has been calculated from the $E$–$T$ characteristics at the same criterion. The data from the two different types of measurement lie on a single curve at a particular magnetic field to within ~20 mK.

As shown in Figure 5.3, the electric field–temperature characteristics can also be described by a power law, where the exponent is again approximately constant over one order of magnitude of electric field (we note, however, that an exponential dependence gives a similarly accurate parameterisation [51]). The power-law exponent of the $E$–$T$ characteristics ($\partial \log E / \partial \log T$) can be related to the $n$-value using the following expression (note that the partial derivatives mean that $J$, $B$, and $\varepsilon$ are constant):

$$\left.\frac{\partial \log E}{\partial \log T}\right|_{T=T_{cs}} = \left.\left(\frac{\partial \log E}{\partial \log J_C} \frac{\partial \log J_C}{\partial \log T}\right)\right|_{T=T_{cs}} = \left.-n\frac{T_{cs}}{J_C}\frac{\partial J_C}{\partial T}\right|_{T=T_{cs}}. \tag{5.3}$$

This expression has been used to calculate values of $n$ from the exponents of the $E$–$T$ characteristics (between 10 and 100 $\mu$Vm$^{-1}$), the values of $T_{cs}$ and $J_C$ (at 10 $\mu$Vm$^{-1}$), and the partial temperature derivatives of $J_C$ (calculated at $T_{cs}$ using spline fits to the standard $J_C$ data). These calculated values of $n$ are plotted as a function of temperature in Figure 5.5 together with $n$-values calculated in the standard way from the $E$–$J$ characteristics (also for electric fields between 10 and 100 $\mu$Vm$^{-1}$). The $n$-values obtained using the two different methods lie on a single curve at a particular magnetic field to within the
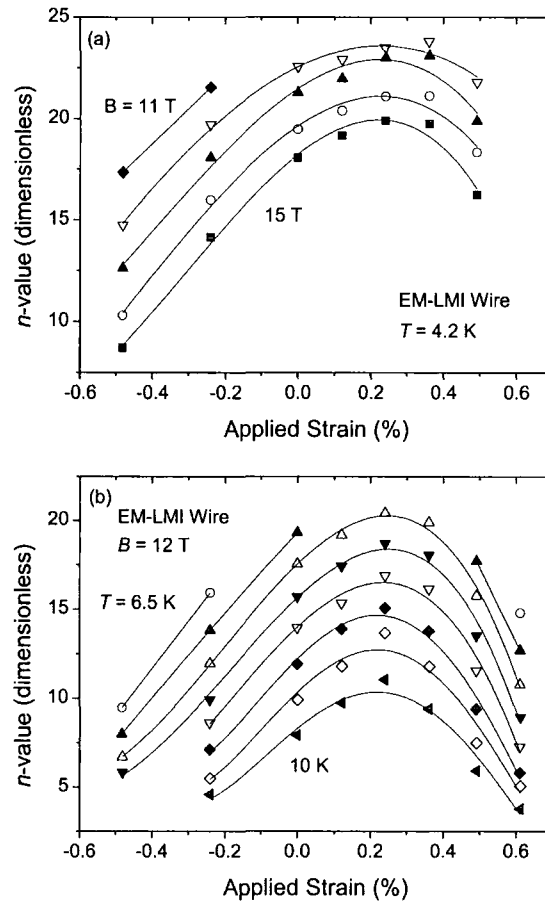


**Figure 5.6.** The $n$-value for electric fields between 10 and 100 $\mu$Vm$^{-1}$ as a function of applied strain for the EM-LMI wire: (a) at 4.2 K and at integer magnetic fields between 11 and 15 T; (b) at 12 T and at 0.5 K increments between 6.5 and 10 K. The lines are a guide to the eye.
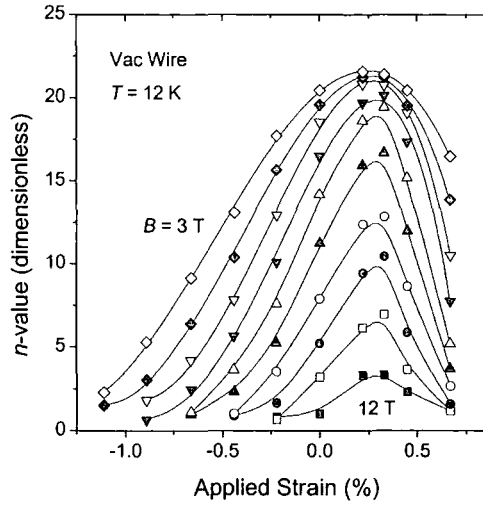
**Figure 5.7.** The *n*-value for electric fields between 10 and 100 μVm$^{-1}$ as a function of applied strain for the Vac wire at 12 K and at integer magnetic fields between 3 and 12 T. The lines are a guide to the eye.

accuracy of our measurements. In this case, the error corresponds to an uncertainty in temperature of ~100 mK, or, more probably, systematic changes in temperature during the transition (10–100 μVm$^{-1}$) of ~10 mK.

The data presented show $E(J,B,T,\varepsilon)$ [and $J_c(B,T,\varepsilon)$] to be path-independent, single-valued functions for our particular measurement procedures. Unpublished data for a number of ITER-candidate wires show that, in high magnetic fields, $J_C$ is also a non-hysteretic function of applied magnetic field and temperature, consistent with other data in the literature on similar wires [159]. Such hysteretic effects are generally only observed in high-temperature superconductors and other inhomogeneous or granular materials [160-162]. We suggest that the equivalence between the *E–T* and *E–J* data observed in this work will be observed for all wires where $J_C$ is non-hysteretic.

The *n*-value [defined in Equation (5.2)] was measured as a function of magnetic field, temperature, and strain. Figure 5.6 shows the *n*-value for electric fields between
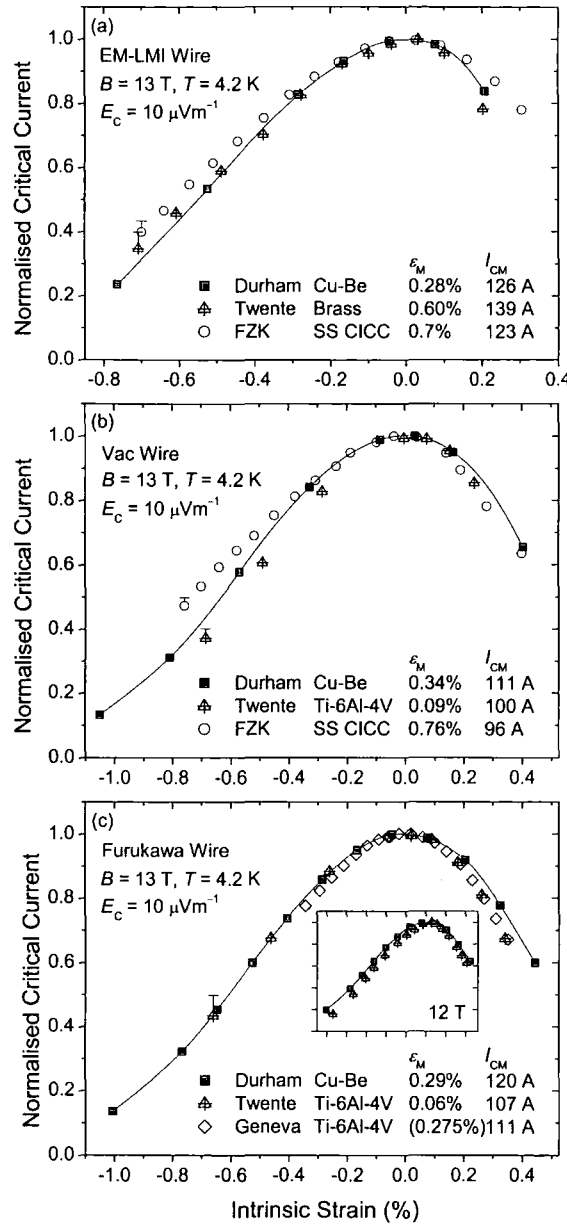
**Figure 5.8.** Interlaboratory comparisons of the normalised critical current as a function of intrinsic strain at 4.2 K and 13 T for (a) EM-LMI, (b) Vac and (c) Furukawa ITER Nb₃Sn wires. Critical currents were measured at 10 μVm⁻¹ or calculated at 10 μVm⁻¹ from measurements performed at higher electric-field criteria using *n*-values measured in Durham (the error bars show the effect of these calculations on the normalised values). The legends show the spring material (or the CICC jacket material), the value of applied strain where the critical current is a maximum ($\varepsilon_M$), and the value of the critical current at this maximum ($I_{CM}$). Inset (c): comparison of Durham and Twente Pacman data at 12 T (same axes and symbols as main graph) [65, 73, 105, 139, 140, 163].

10 and 100 $\mu Vm^{-1}$ as a function of applied strain for the EM-LMI wire. Figure 5.7 shows similar data for the Vac wire (additional data were presented in a previous publication [101]). The variation of $n(B,T,\varepsilon)$ is qualitatively similar to that of $J_C$, decreasing with increasing $B$, $T$ or $|\varepsilon_1|$. However, assuming that $n$ is a unique function of $J_C$ leads to unacceptable errors of typically 25% as $n$ systematically decreases with increasing $T$ or $|\varepsilon_1|$ at constant $J_C$. As yet, we have no simple and accurate parameterisation of the $n$-value.

## 5.3.3 Comparisons of variable-strain $J_C$ data for the EM-LMI, Vac, and Furukawa ITER wires

Interlaboratory comparisons of variable-strain $J_C$ data for the EM-LMI and Vac ITER wires and cables are shown in Figure 5.8, where the normalised critical current at 4.2 K and 13 T is plotted as a function of intrinsic strain. Data are also shown for a Furukawa ITER $Nb_3Sn$ wire [139]. The measurements in other laboratories were performed on individual wires at the University of Twente using different types of "bending spring" [105], at the University of Geneva using a helical spring [65], and on cable-in-conduit conductors at Forschungszentrum Karlsruhe (FZK) using an "axial pull" system [73]. Note that as $J_C$ was measured at higher electric-field criteria at Twente (500 $\mu Vm^{-1}$) and FZK (100 $\mu Vm^{-1}$), we have calculated $J_C$ at 10 $\mu Vm^{-1}$ from these data using $n$-values measured in Durham—$n$ decreases by a factor of ~2 from 0% to −0.7% intrinsic strain (see Section 5.3.2) so that the strain-dependence of the normalised critical current is larger at lower electric-field criteria. It can be seen that the agreement between the normalised critical current data from different laboratories is generally good. The biggest deviations occur for the cable-in-conduit conductors at $\varepsilon_1 \ll 0$, where the CICC data are less strain-sensitive. The normalised critical current data for measurements on wires agree to within ±6% for the EM-LMI wire ($\varepsilon_1 = -0.7\%$), ±8% for the Vac wire

($\varepsilon_1 = -0.7\%$), and $\pm 2.5\%$ for the Furukawa wire ($\varepsilon_1 = +0.35\%$). We have particular confidence in our EM-LMI data because six different samples on springs of various materials and geometries all show a similar intrinsic strain-dependence for $J_C$ to within $\pm 5\%$ (see Chapters 3 and 4), and the reversibility of $J_C$ over a number of strain cycles (described below) demonstrates that the samples were not damaged. For all of the wires, there are variations of approximately $\pm 7\%$ between different laboratories for the value of the critical current at $\varepsilon_1 = 0$, although some of these variations may be due to the different billets measured.

In general, obtaining reliable variable-strain $J_C$ data presents a difficult experimental challenge. In addition to the standard good practice required for critical current measurements [96, 156], there are a number of issues to be considered: damage to any part of the wire during mounting may have a considerable effect on the strain-dependence of $J_C$; the experimental set-up should preferably involve relatively long lengths of wire in a homogeneous strain-state beyond the measurement regions, in order to avoid current-transfer voltages [61, 64]; and the sample holder (if used) should not be strained beyond its elastic limit. Plasticity of the component parts of the superconducting wires can also play a significant role in interlaboratory comparisons. In Chapter 4, measurements on EM-LMI and Vac wires demonstrated that extensive strain cycling can cause $J_C$ to increase by up to ~7% at 4.2 K, 12 T, and $\varepsilon_1 = 0$, without damaging the superconducting filaments [116]. These changes in $J_C$ were attributed to changes in the radial stress on the filaments due to the plastic deformation of the matrix. In the present measurements, $J_C$ for the EM-LMI wire (sample 1) at zero applied strain increased by ~3% after the cycle 0% → 0.49% → −0.48% → 0%, and $J_C$ at −0.48% applied strain decreased by ~4% after the cycle −0.48% → 0.61% → −0.48%. Hence additional variations in the strain-dependence of $J_C$ of the order of a few percent are to be expected when measurements at different laboratories involve multiple strain cycles (thermal or

mechanical) that strain the wire beyond the elastic limit of the component materials (~0.1%). From a comparison of the variable-strain datasets available, we conclude that variations of typically ±5% in the strain-dependence of the normalised $J_C$ can in principle be achieved between different laboratories.

## 5.4 $J_C(B,T,\varepsilon)$ scaling laws

### 5.4.1 Interpolative Scaling Law for $J_C(B,T,\varepsilon)$

The $J_C(B,T,\varepsilon)$ data can be parameterised using the Interpolative Scaling Law (ISL) [75] in which the volume pinning force ($F_p = J_C B$) is given by [46]:

$$F_p = \frac{A'(\varepsilon)\left[B_{C2}^*(T,\varepsilon)\right]^n}{\left[\kappa_1^*(T,\varepsilon)\right]^m} b^p (1-b)^q , \tag{5.4}$$

where $b = B/B_{C2}^*(T,\varepsilon)$ and $B_{C2}^*(T,\varepsilon)$ is the effective upper critical field which is parameterised by:

$$B_{C2}^*(T,\varepsilon) = B_{C2}^*(0,\varepsilon)(1-t^\nu) . \tag{5.5}$$

Here, $t = T/T_C^*(\varepsilon)$ and $T_C^*(\varepsilon)$ is the effective critical temperature. $\kappa_1^*(T,\varepsilon)$ is the Ginzburg–Landau parameter given by [75]:

$$\kappa_1^*(T,\varepsilon) = \frac{1.03\left[\eta(\varepsilon)\right]^{1/2} B_{C2}^*(T,\varepsilon)}{\mu_0^{1/2}\left[\gamma(\varepsilon)\right]^{1/2} T_C^*(\varepsilon)(1-t^2)} , \tag{5.6}$$

where $\eta(\varepsilon) = 1 - 12.2(k_B T_C/\hbar\omega_{ln})^2 \ln(\hbar\omega_{ln}/3k_B T_C)$ is a strong-coupling correction to the
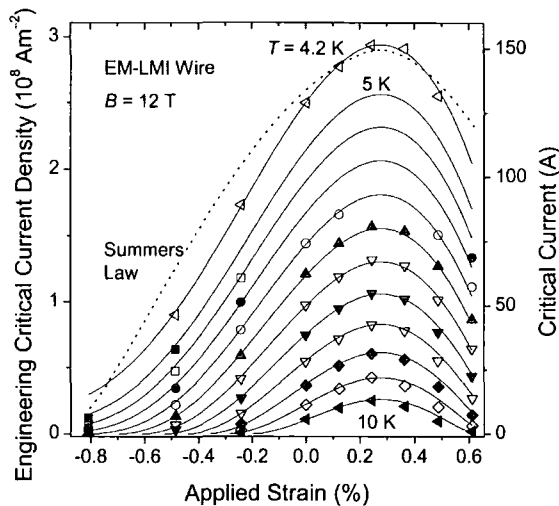
**Figure 5.9.** Engineering critical current density (and critical current) of the EM-LMI wire as a function of applied strain at 12 T and at 4.2 K and 0.5 K increments between 5 and 10 K. The symbols show the measured data, the solid lines the Interpolative Scaling Law, and the dotted line the Summers Scaling Law [obtained by fitting the $J_{\rm c}(B,T,\varepsilon)$ data for $|\varepsilon_{\rm I}| < 0.22\%$].
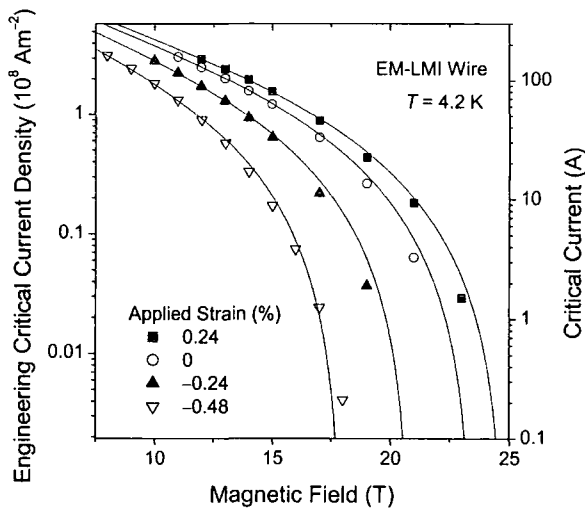
**Figure 5.10.** Engineering critical current density (and critical current) of the EM-LMI wire as a function of magnetic field at 4.2 K and at different applied strains between 0.24% and −0.48%. The symbols show the measured data, and the lines the Interpolative Scaling Law.

BCS value of the ratio $\mu_0 \gamma T_C^2 / \left[ B_C(0) \right]^2$ ($\omega_{\ln}$ is an average phonon frequency) and $\gamma(\varepsilon)$

is the electronic specific heat coefficient [29, 37, 75]. Combining Equations (5.4) and

(5.6), and incorporating $A'(\varepsilon)$, $\eta(\varepsilon)$, and $\gamma(\varepsilon)$ into a single strain-dependent parameter

$A(\varepsilon)$ results in the following expression for $J_C(B,T,\varepsilon)$ :

$$ J_C(B,T,\varepsilon) = A(\varepsilon) \left[ T_C^*(\varepsilon)(1-t^2) \right]^m \left[ B_{C2}^*(T,\varepsilon) \right]^{n-m-1} b^{p-1} (1-b)^q . \qquad (5.7) $$

The scaling law therefore involves the exponents *m*, *n*, *p*, *q*, and *v*, and the

parameters $A(\varepsilon)$, $T_C^*(\varepsilon)$, and $B_{C2}^*(0,\varepsilon)$. These strain-dependent parameters are

constrained to be fourth-order polynomial functions of applied strain with a stationary
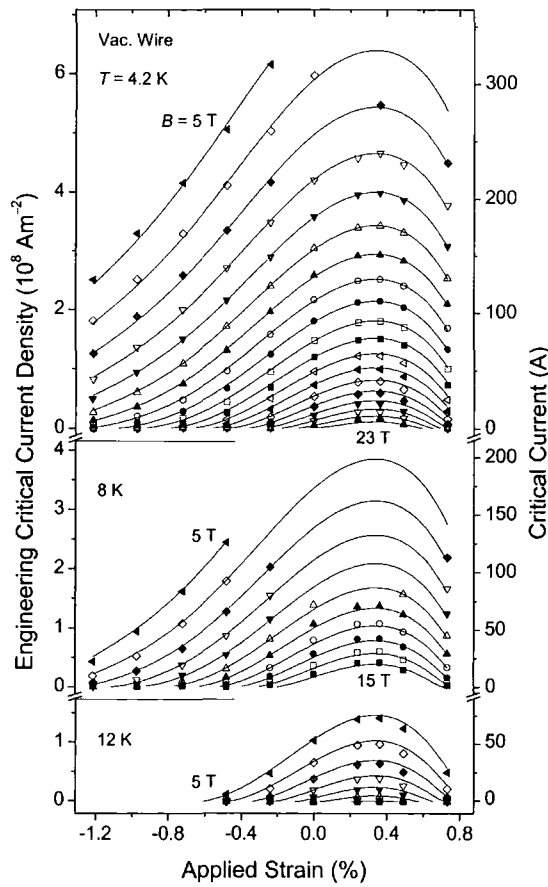


**Figure 5.11.** Engineering critical current density (and critical current) of the Vac wire as a
function of applied strain at integer magnetic fields between 5 and 23 T and at 4.2, 8, and 12 K.
The symbols show the measured data and the solid lines the Interpolative Scaling Law.
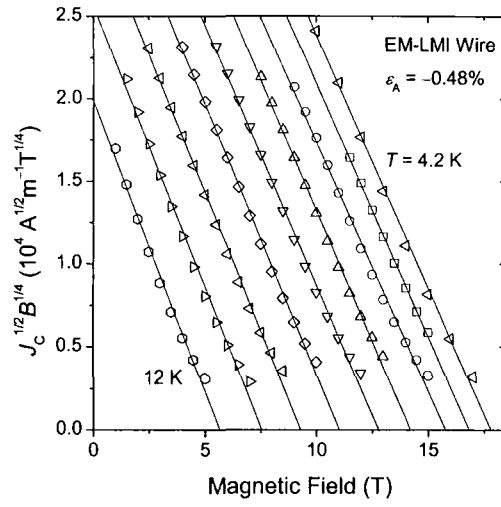
**Figure 5.12.** Kramer plots for the EM-LMI wire at −0.48% applied strain and at 4.2 K and 1 K increments between 5 and 10 K. The symbols show the measured data, and the lines the best straight-line fits.
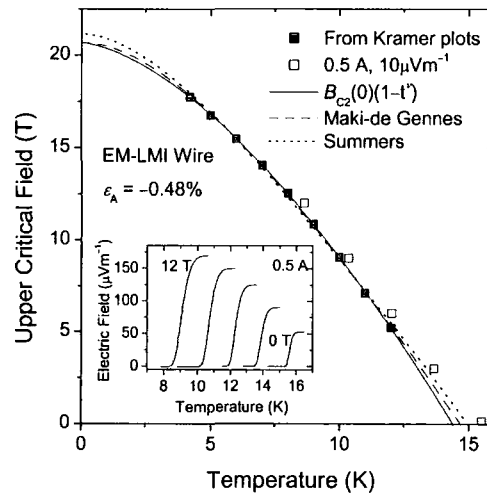


**Figure 5.13.** Upper critical field as a function of temperature for the EM-LMI wire at −0.48% applied strain (i.e. close to the operating strain of the TFMC [104]). The closed symbols show $B_{C2}^*$ obtained from Kramer plots (see Figure 5.12) and the lines show various fits to these data. The open symbols show the values of $B_{C2}^\rho$ determined at 0.5 A and 10 $\mu$Vm$^{-1}$ from the $E$–$T$ data shown in the inset.

point (e.g. maximum) at a common value, $\varepsilon_M$. Similarly to previous work, the exponent

$m$ is set to 2, implying the relation $J_C \propto 1/\left(\kappa_1^*\right)^2$ [78, 142]. The Interpolative Scaling

Law enables extremely accurate parameterisations of the $J_C$ data over the large ranges of

magnetic field, temperature, and strain that were investigated, with RMS differences

between the measured and calculated values of $2.72 \times 10^6 \, \text{Am}^{-2}$ (1.40 A) for the

EM-LMI wire and $3.98 \times 10^6 \, \text{Am}^{-2}$ (2.05 A) for the Vac wire. The parameterisations are

compared graphically with the measured $J_C\left(B,T,\varepsilon\right)$ in Figures 5.9–5.11.

For the EM-LMI wire, the optimum values of $p$ (0.474) and $q$ (1.95) are close to the

commonly-used "Kramer values" ($p = 1/2$ and $q = 2$) [46, 58, 142]. Figure 5.12 shows

Kramer plots ($J_C^{1/2}B^{1/4}$ versus $B$) for the EM-LMI wire at −0.48% applied strain: the good

straight-line fits also demonstrate that the magnetic field dependence of $J_C$ can be

parameterised with $p = 1/2$ and $q = 2$ (at least for $I_C > 1$ A). For the Vac wire, however,

the optimum values of $p$ (0.468) and $q$ (1.48) are further from the Kramer values, and

setting $p = 1/2$ and $q = 2$ results in a ~25% increase in the RMS error for the best fit

(from 2.05 A to 2.60 A) and unphysically high values for the effective upper critical

field, with $B_{C2}^*\left(0,\varepsilon_1 = 0\right) \approx 35$ T .

Figure 5.13 shows the upper critical field as a function of temperature for the

EM-LMI wire at −0.48% applied strain. It can be seen that Equation (5.5) provides a

good fit to the $B_{C2}^*\left(T,\varepsilon\right)$ data obtained from the Kramer plots in Figure 5.12 (with

$\nu \approx 1.5$ in this case). Two other fits to these data are also shown: the Maki–de Gennes

relation for a dirty superconductor with no Pauli paramagnetic limiting [40, 41, 43],

which fits the data well, and the Summers Scaling Law relation [Equation (5.9)], which is

somewhat less accurate. Also shown in Figure 5.13 are the values of upper critical field

[$B_{C2}^{\rho}\left(T,\varepsilon\right)$] determined from the $E$–$T$ characteristics for a current of 0.5 A and an

electric-field criterion of $10 \, \mu\text{Vm}^{-1}$ (5–20% of the transition height). Note that the
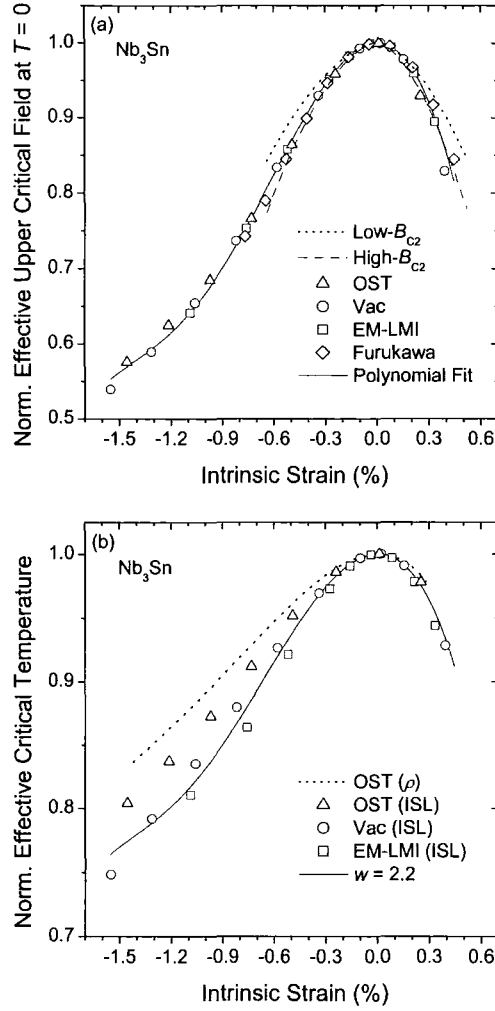
**Figure 5.14.** (a) The normalised effective upper critical field at $T = 0$ and (b) normalised effective critical temperature as a function of intrinsic strain for different $Nb_3Sn$ wires. In (a), the symbols show data for wires measured in Durham and the solid line shows a universal fit to these data, while the dotted line is for previous measurements on low- $B_{C2}^*(0)$ wires [61] and the dashed line for high- $B_{C2}^*(0)$ wires [80]. For the Furukawa data and the dashed and dotted lines, $B_{C2}^*(0)$ was calculated from the $B_{C2}^*(4.2 \text{ K})$ data using Equations (5.5) and (5.11). In (b), the solid line is calculated using the universal fit to the normalised $B_{C2}^*(0)$ data and the power-law relation with $w = 2.2$, while the dotted line shows $T_C^p(\varepsilon_1)$ data obtained from resistivity measurements for the OST wire.

equivalence between the $E$–$T$ and $E$–$J$ data demonstrated in Section 5.3.2 means that these values of $B_{C2}^p(T,\varepsilon)$ are also the values of $B$ where $I_C$ at 10 $\mu Vm^{-1}$ is 0.5 A. These low-current-density values are ~0.4 K higher for $B \geq 4$ T and ~0.8 K higher for $B = 0$ than the values obtained from the Kramer plots [and Equation (5.5)]. At this value of strain, the measured $J_C$ goes to zero less rapidly than the Kramer lines, with a "tail" that is usually associated with the distribution of $T_C$ and $B_{C2}$ in technological wires [75, 120]. Determining $T_C$ from measurements at very low current densities ($B \approx 0$) provides a method for assessing the strain-state of the model coils at cryogenic temperatures, although it must be noted that the measured value of $T_C^p(B=0)=15.5$ K at −0.76% intrinsic strain differs quite considerably from the scaling-law parameter $T_C^*$ (= 14.6 K). Self-field effects may also be important in such measurements.

Figure 5.14(a) shows normalised values of $B_{C2}^*(0,\varepsilon_1)$ for the EM-LMI and Vac wires, as well as additional data for the Furukawa wire [139] and an OST wire [75]. It can be seen that $B_{C2}^*(0,\varepsilon_1)$ for these Nb₃Sn wires follows an approximately universal relation, which is also largely independent of the choice of $p$ and $q$ [61]. Hence the higher strain-sensitivity of $J_C$ for the EM-LMI wire in relation to the other wires (see Figure 5.8) is due to lower absolute values of $B_{C2}^*(0)$ and $T_C^*$ at zero intrinsic strain. Figure 5.14(a) also includes two different datasets obtained from the literature, represented by best-fit lines [61, 80]. These values were calculated from the $B_{C2}^*(4.2\,\text{K},\varepsilon_1)$ data using Equations (5.5) and (5.11), although the differences between the normalised values of $B_{C2}^*$ at $T = 0$ and 4.2 K are not large (the Furukawa values were also calculated in this way) [148]. The less strain-sensitive line taken from Ekin's well-known work represents relatively clean Nb₃Sn with low values of $B_{C2}^*(0,\varepsilon_1 = 0)$ of ~24 T [61], while the more strain-sensitive line is for Nb₃Sn wires with Ta additions and higher values of $B_{C2}^*(0,\varepsilon_1 = 0)$ [80]. The ITER-candidate wires and other recently-developed Nb₃Sn wires have ternary additions of Ti (EM-LMI) or Ta (Vac) and relatively high values of

$B^*_{C2}(0, \varepsilon_1 = 0)$: typically 28–30 T. Hence the better agreement with the previous ternary data rather than the binary data correlates with the higher values of $B^*_{C2}(0, \varepsilon_1 = 0)$. The differences between binary and ternary Nb$_3$Sn are also predicted by microscopic theory (see Section 5.5), but have been somewhat neglected in the past [148].

Figure 5.14(b) shows normalised values of $T^*_C(\varepsilon_1)$ for the EM-LMI, Vac, and OST wires. It can be seen that there is more variation between the different wires, although for the two ITER-candidate wires the differences are only ~4%. Also shown in Figure 5.14(b) are $T^\rho_C(\varepsilon_1)$ data obtained from resistivity measurements for the OST wire, which can be seen to be less strain-sensitive than the scaling-law values. This behaviour is observed for the $B^\rho_{C2}(T,\varepsilon)$ and $T^\rho_C(\varepsilon_1)$ data for all of the wires we have investigated, and can be related to strain (and temperature) variations in the low-current-density tails discussed above. A reasonable interpretation of the difference is that the scaling law values of $B^*_{C2}$ (and $T^*_C$) are characteristic values for the bulk of the material, while the resistivity values give the maxima of the distributions in $B_{C2}$ (and $T_C$) [61, 75, 164].

## 5.4.2 Comparison with Summers Scaling Law

The Summers Scaling Law for $J_C(B,T,\varepsilon)$ involves the following relations [61, 148, 149]:

$$J_C(B,T,\varepsilon) = C(\varepsilon)(1-t^2)^2 \left[ B^*_{C2}(0,\varepsilon) \right]^{-1/2} b^{-1/2}(1-b)^2 \tag{5.8}$$

$$B^*_{C2}(T,\varepsilon) = B^*_{C2}(0,\varepsilon)(1-t^2)\left[1 - 0.31t^2(1 - 1.77\ln t)\right] \tag{5.9}$$

$$\frac{B^*_{C2}(0,\varepsilon_1)}{B^*_{C2}(0,0)} = \left[\frac{T^*_C(\varepsilon_1)}{T^*_C(0)}\right]^3 = \left[\frac{C(\varepsilon_1)}{C(0)}\right]^2 = 1 - a|\varepsilon_1|^{1.7}, \tag{5.10}$$

with $a = 1250$ for $\varepsilon_1 > 0$ and $a = 900$ for $\varepsilon_1 < 0$. The scaling law is commonly used for ITER-candidate conductors [104, 129, 136, 149], but we have found that it predicts a weaker strain-dependence for $J_C$ than is observed and hence cannot parameterise ternary $Nb_3Sn$ data accurately—typical RMS differences are ~10 A. Figure 5.9 explicitly shows a comparison between the measured data for the EM-LMI wire and the values for $J_C(12 \text{ T},4.2 \text{ K},\varepsilon_1)$ calculated using the Summers Scaling Law with the free parameters obtained by fitting the data for $|\varepsilon_1| < 0.22\%$; similar disagreement is also observed for the Vac wire [104, 136].

We can improve the accuracy of the Summers fits over a limited strain range ($\varepsilon_1 \geq -0.8\%$) by leaving $a$ as a free parameter; for the EM-LMI wire, the best-fit is obtained with $a = 1840$ ($\varepsilon_1 > 0$) and 1160 ($\varepsilon_1 < 0$) and has an RMS error of 2.4 A, while for the Vac wire, values of $a = 1900$ and 1160, and an RMS error of 2.4 A are obtained. These values of $a$ are comparable with previous values for high- $B_{C2}^*(0)$ $Nb_3Sn$ [$a = 1690$ for $\varepsilon_1 > 0$ and 1210 for $\varepsilon_1 < 0$, see Figure 5.14(a)] [80]. However, Figure 5.14(a) shows that, even for optimum values of $a$, Equation (5.10) begins to deviate significantly from the measured $B_{C2}(0,\varepsilon_1)$ at a compressive strain of $\varepsilon_1 \approx -0.7\%$ (close to the strain at which the TFMC operates). Note, however, that Equation (5.10) is based upon measurements that were only performed at tensile applied strains corresponding to $\varepsilon_1 \geq -0.5\%$ [61]. The data in this chapter have second-derivatives (with respect to $\varepsilon_1$) of both $B_{C2}(0,\varepsilon_1)$ [Figure 5.14(a)] and $J_C(12 \text{ T},4.2 \text{ K},\varepsilon_1)$ (Figures 5.9 and 5.11) that change sign at $\varepsilon_1 \approx -0.7\%$, behaviour which cannot be reproduced by Equation (5.10). Hence we will set aside this function for the strain-dependence as polynomial functions seem preferable—especially if large strain ranges are being investigated.

# 5.5 Relationship between strain-dependent superconducting parameters

In this section, we will consider the relationship between $B_{C2}(0,\varepsilon_I)$ and $T_C(\varepsilon_I)$, presenting our experimental data for a number of wires and analysing the relationship using microscopic theory. For the analysis we adopt a similar approach to Welch [123], using Eliashberg theory (the Allen and Dynes equation [35, 36]) and Ginzburg–Landau–
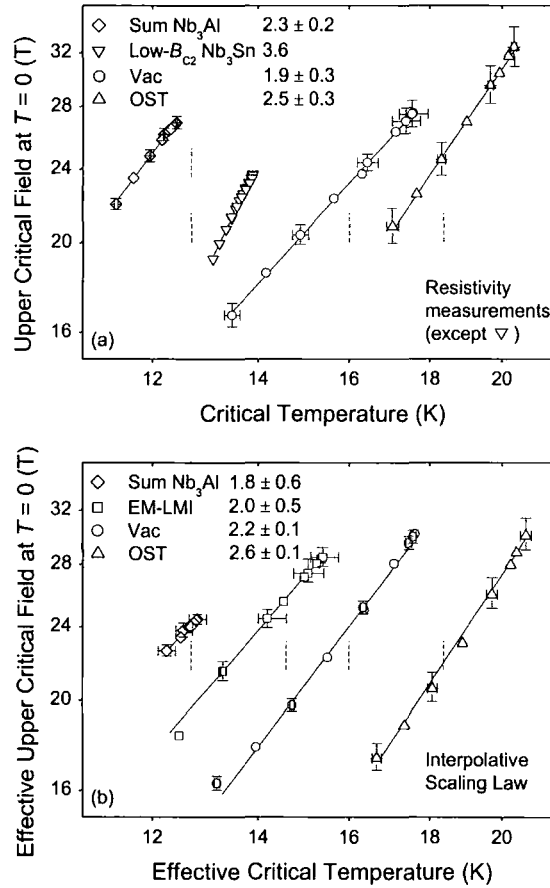


**Figure 5.15.** A log–log plot of upper critical field at $T = 0$ versus critical temperature for different $A$15 wires: (a) data from resistivity and other measurements; (b) effective values obtained by fitting the $J_C$ data using the Interpolative Scaling Law. The solid lines show the best power-law fits and the legend shows the values of the exponent $w$. Except for the Vac wire, the data have been shifted horizontally for clarity (the vertical dashed lines show $T_C = 16$ K for each wire).

Abrikosov–Gor'kov theory [27, 37, 41] to provide a better understanding of the empirical scaling-law relations, and the microscopic mechanisms responsible for the strain effects in $A15$ ($Nb_3Sn$ and $Nb_3Al$) superconducting wires.

## 5.5.1 Power-law relationship and experimental data

A power-law relationship between $B_{C2}(0,\varepsilon_1)$ and $T_C(\varepsilon_1)$ was first proposed by Ekin (although originally in terms of the upper critical field at 4.2 K) [61]:

$$\frac{B_{C2}(0,\varepsilon_1)}{B_{C2}(0,\varepsilon_1=0)} = \left(\frac{T_C(\varepsilon_1)}{T_C(\varepsilon_1=0)}\right)^w.$$ (5.11)

The exponent $w \approx 3$ was estimated using $B_{C2}^*(4.2\,\text{K},\varepsilon_1)$ data obtained from $J_C$ measurements on binary $Nb_3Sn$ wires [61] and $T_C^x(\varepsilon_1)$ data from susceptibility measurements on a different set of binary $Nb_3Sn$ wires [68]. The power-law with $w = 3$ is currently used in a number of scaling laws for $J_C(B,T,\varepsilon)$ [62, 148]. The original (low-$B_{C2}^*$) data are shown on a log–log plot in Figure 5.15(a), with $B_{C2}^*(0,\varepsilon_1)$ calculated from the $B_{C2}^*(4.2\,\text{K},\varepsilon_1)$ and $T_C^x(\varepsilon_1)$ data using the Maki-de Gennes relation. The best fit gives $w = 3.6$ (the value is 3.8 if the upper critical field data at 4.2 K are used directly). However, assuming that $T_C^x(\varepsilon_1)$ and $T_C^\rho(\varepsilon_1)$ behave similarly, the different strain-dependences observed for our scaling-law and resistivity data imply that artificially high values of $w$ may be obtained from combining $B_{C2}^*$ and $T_C^x$ data. Also shown in Figure 5.15(a) are values obtained from low-current-density measurements of $B_{C2}^\rho(T,\varepsilon_1)$ for the Vac $Nb_3Sn$ wire ($I = 0.5$ A), the OST $Nb_3Sn$ wire (30 mA) [75], and a Sumitomo $Nb_3Al$ wire (30 mA) [78], where Equation (5.5) was used to extrapolate to $T = 0$ and $T_C$. It can be seen that for these $A15$ wires, the values of $w$ are all between ~1.9 and ~2.5. In addition, Figure 5.15(b) shows the values of $B_{C2}^*(0,\varepsilon_1)$ and $T_C^*(\varepsilon_1)$ obtained using the Interpolative Scaling Law from the comprehensive $J_C(B,T,\varepsilon)$ datasets available for

four different $A15$ wires. These are also consistent with the power law and give similar values of $w$. For $Nb_3Sn$ wires characterised by high values of $B_{C2}^*\left(0,\varepsilon_1=0\right)$ (approximately 28–30 T), the values of $w \le 2.5$ are therefore similar for both resistivity and scaling-law data, despite the different strain-dependences observed, and are significantly lower than the values ($w \ge 3$) obtained for binary, low-$B_{C2}^*$ (~24 T) $Nb_3Sn$ wires.

## 5.5.2 Analysis using microscopic theory

The Allen and Dynes equation gives the critical temperature of strongly-coupled superconductors in terms of various microscopic parameters [35, 36]:

$$k_B T_C = \frac{f_1 f_2 \hbar \omega_{\ln}}{1.20} \exp\left(-\frac{1.04(1+\lambda)}{\lambda - \mu^* - 0.62\lambda\mu^*}\right), \tag{5.12}$$

where $\omega_{\ln}$ is a weighted logarithmically-averaged phonon frequency, $\lambda$ is the electron-phonon coupling parameter, $\mu^*$ is the effective Coulomb-repulsion parameter, and $f_1$ and $f_2$ are correction factors of order unity [35]. The electron-phonon coupling parameter is

**Table 5.1.** Microscopic parameters determined from tunnelling measurements on $Nb_3Sn$ [165] and $Nb_3Al$ (23 at. % Al) [166]. Also shown are the values of $T_C$ calculated using Equation (5.12), and the values of $\mu^*$ required for Equation (5.12) to give the measured values of $T_C$ (shown in brackets).

|                          | $Nb_3Sn$          | $Nb_3Al$          |
|--------------------------|-------------------|-------------------|
| $\omega_{\ln}$ (meV)     | 10.8              | 9.5               |
| $\omega_2$ (meV)         | 15.0              | 13.5              |
| $\lambda$                | $1.8 \pm 0.15$    | $1.7 \pm 0.05$    |
| $\mu^*$                  | $0.16 \pm 0.03$ (0.14) | $0.15 \pm 0.02$ (0.10) |
| $T_C$ (K) calc. (meas.)  | 16.2 (17.5)       | 13.9 (16.4)       |

related to the bare electronic density of states at the Fermi energy $N(0)$ and a weighted RMS phonon frequency $\omega_2$ by [36]:

$$\lambda = \frac{N(0)\langle I^2 \rangle}{M\omega_2^2},$$

(5.13)

where $\langle I^2 \rangle$ is the average over the Fermi surface of the electron-phonon matrix element squared and $M$ is the average ionic mass. The electronic specific heat coefficient $\gamma$ is related to $N(0)$ and $\lambda$ by [36]:

$$\gamma = \tfrac{2}{3}\pi^2 k_B^2 N(0)(1+\lambda).$$

(5.14)

The parameters $\omega_{ln}$, $\omega_2$, $\lambda$, and $\mu^*$ determined from tunnelling measurements on Nb$_3$Sn [165] and off-stoichiometric Nb$_3$Al [166] are shown in Table 5.1. In the analysis
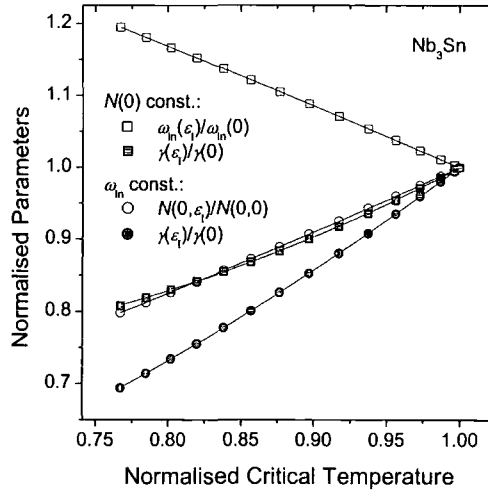


**Figure 5.16.** Calculated microscopic parameters for Nb$_3$Sn as a function of critical temperature, with all quantities normalised to their values at zero intrinsic strain. Square symbols: $\omega_{ln}$ and $\gamma$ calculated assuming constant $N(0)$; round symbols: $N(0)$ and $\gamma$ calculated assuming constant $\omega_{ln}$. The maximum reduction in critical temperature (23%) corresponds to the measured reduction for the Vac wire at $-1.55\%$ intrinsic strain.

described below, we will use $\mu^*$ as a free parameter to fit the measured zero-intrinsic-strain values of $T_C$, which can generally be achieved with relatively small changes in $\mu^*$ (see Table 5.1) [37]. We will make the assumption that the variations of $\mu^*$ or $\langle I^2 \rangle$ with strain are considerably less important than the other parameters, and hence they can be considered as constants. We will also assume that the strain-dependence of the normalised average phonon frequencies ($\omega_{ln}$ and $\omega_2$) is the same [153].

The variation of $T_C$ with uniaxial strain can be related to variations in the average phonon frequencies and/or variations in the bare electronic density of states at the Fermi energy. Due to a lack of detailed information in the literature about the uniaxial strain-dependence of these parameters, we will begin by considering the two extreme cases: firstly that the strain-dependence of $T_C$ is entirely due to the strain-dependence of the average phonon frequencies, and secondly that strain only affects electronic properties [i.e. $N(0)$]. For Nb$_3$Sn, Figure 5.16 shows how the various parameters depend on $T_C$ in these two cases: in the first case, $\omega_{ln}$ increases approximately linearly with decreasing $T_C$ and, in the second case, $N(0)$ decreases approximately linearly with decreasing $T_C$. In both cases, the magnitude of the change is ~20% for a decrease in $T_C$ of 23%, corresponding to $\varepsilon_I = -1.55\%$ for the Vac wire. The data shown in Figure 5.16 are calculated for Nb$_3$Sn with $T_C(\varepsilon_I = 0) = 17.5\,\mathrm{K}$ (Vac wire), but the relationships between the reduced parameters and the reduced critical temperature are insensitive (to within ~1%) to quite large variations in $T_C(\varepsilon_I = 0)$ (~1 K). These relationships are also similar (to within ~1%) for Nb$_3$Al, although the critical temperature of Nb$_3$Al is a factor of ~3 less sensitive to uniaxial strain [78].

The upper critical field at $T = 0$ can be calculated using the following expression [27, 37, 41]:

$$B_{C2}(0) = 0.973 \mu_0^{1/2} \eta_{B_{C2}(0)} \kappa^*(0, \lambda_{tr}) \left[R(\lambda_{tr})\right]^{-1}$$
$$\times \left[7.30 \times 10^{37} \left(\gamma T_C / S\right)^2 + 2.78 \times 10^6 \gamma T_C \rho_n \right], \tag{5.15}$$

where $\eta_{B_{C2}(0)}$ is a strong-coupling correction of order unity [37], $\kappa^*$ is the reduced temperature-dependent Ginzburg–Landau parameter [ $\kappa^*(0,0) = 1.26$ and $\kappa^*(0,\infty) = 1.20$], $R(\lambda_{tr})(1+\lambda_{tr})^{-1}$ is the Gor'kov function [ $R(0) = 1$ and $R(\infty) = 1.17$], $\lambda_{tr}$ is the reduced mean collision frequency given by [27]:

$$\lambda_{tr} = 0.882 \, \xi^*_{BCS}/l_{tr} = 3.81 \times 10^{-32} \, S^2 \rho_n / (\gamma T_C), \qquad (5.16)$$

$\xi^*_{BCS}$ is the renormalised BCS coherence length, $l_{tr}$ is the electron mean free path, $S$ is the Fermi surface area, and $\rho_n$ is the low-temperature normal-state resistivity.

Both $S$ and $\rho_n$ are expected to be largely independent of uniaxial strain, and are considered as constants with $S = (1.7 \pm 0.7) \times 10^{21} \, \text{m}^2$ for $Nb_3Sn$ [27] and $(1.8 \pm 0.7) \times 10^{21} \, \text{m}^2$ for $Nb_3Al$ [167]. For $\lambda_{tr} \ll 1$ (the "clean limit"), the first term in the square brackets in Equation (5.15) dominates and $B_{C2}(0) \propto (\gamma T_C)^2$ whereas for $\lambda_{tr} \gg 1$ (the "dirty limit"), the second term dominates and $B_{C2}(0) \propto \gamma T_C$. For intermediate values of $\lambda_{tr}$, $B_{C2}(0)$ is approximately proportional to $(\gamma T_C)^v$, where the exponent $v$ depends only on $\lambda_{tr}$ and has a value between ~1 and ~2. Analysis of data for monofilamentary bronze-route $Nb_3Sn$ wires [168] shows that $\lambda_{tr}(\varepsilon_I \approx 0) = 3 \pm 2.5$ for materials with tertiary additions (Ti, Ta) and optimal upper critical fields, which are similar to the technological wires that we have measured (the uncertainty in $\lambda_{tr}$ given here is calculated from the uncertainty in $S$). By setting $\lambda_{tr}(\varepsilon_I = 0) = 3$, the variation of $B_{C2}(0)$ can be calculated using Equations (5.15) and (5.16), with $\gamma(\varepsilon_I = 0)$ and $\rho_n$ calculated from the measured value of $B_{C2}(0)$ at zero intrinsic strain [for the Vac wire with $B_{C2}(0, \varepsilon_I = 0) = 27.6 \, \text{T}$, we get values consistent with the literature [27], $\rho_n = (41 \pm 17) \, \mu\Omega\text{cm}$ and $\gamma(\varepsilon_I = 0) = 860 \pm 350 \, \text{Jm}^{-3}\text{K}^{-2}$, although the conclusions given below are independent of the value of $B_{C2}(0,0)$].
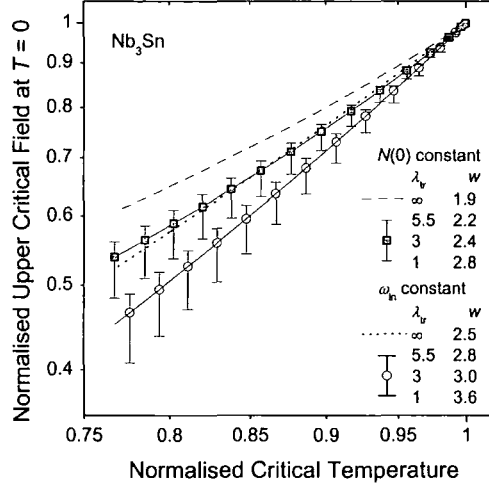
**Figure 5.17.** Log–log plot of the calculated upper critical field at $T = 0$ versus critical temperature for Nb$_3$Sn, with both quantities normalised to their values at zero intrinsic strain. Two cases are considered: (a) $N(0)$ is constant, and $\omega_{\ln}$ and $\omega_2$ vary with uniaxial strain, and (b) $\omega_{\ln}$ and $\omega_2$ are constant, and $N(0)$ varies with strain. The symbols are for $\lambda_{tr}(\varepsilon_1 = 0) = 3$, the error bars for $\lambda_{tr}(\varepsilon_1 = 0) = 5.5$ and 1 at their extrema, and the dotted and dashed lines for $\lambda_{tr}(\varepsilon_1 = 0) = \infty$ (extreme dirty limit). The maximum reduction in critical temperature (23%) corresponds to the measured reduction for the Vac wire at $-1.55\%$ intrinsic strain.

Figure 5.17 shows a normalised log–log plot of the calculated values of $B_{C2}(0, \varepsilon_1)$ as a function of $T_C(\varepsilon_1)$ for Nb$_3$Sn. It can be seen that the relationship between $B_{C2}(0)$ and $T_C$ is quite accurately described by a power law [Equation (5.11)] with, for $\lambda_{tr}(\varepsilon_1 = 0) = 3$, the exponent $w = 2.4$ for the case where only $\omega_{\ln}$ varies with uniaxial strain, and $w = 3.0$ for the case where only $N(0)$ varies with strain. These values are for fits over the range $0.77 \leq T_C(\varepsilon_1)/T_C(0) \leq 1$, which is relevant for comparison with our experimental data in Figure 5.15 although $w$ can vary depending on the exact temperature range chosen by about $\pm 0.1$. The deviations from the power law are such that $w$ is larger (by $\leq 0.6$) closer to $T_C(\varepsilon_1)/T_C(0) = 1$. We have investigated alternative functional forms that describe the theoretical data in Figure 5.17 rather better, but have not used them in this chapter because the power law is reasonably accurate for both clean and dirty

superconductors and the improvement in $J_C$ parameterisation was not sufficiently large. Given the large uncertainties in $\lambda_{tr}$, we have also shown in Figure 5.17 the results and values of $w$ for $\lambda_{tr}(\varepsilon_I = 0) = 5.5$ and 1 [1 is considered as the lower bound for Nb$_3$Sn with $B_{C2}(0, \varepsilon_I = 0) \geq 27$ T ], as well as for the extreme dirty limit ($\lambda_{tr} = \infty$). It can be seen that $w$ increases as $\lambda_{tr}(\varepsilon_I = 0)$ decreases or the relative contribution of variations in $N(0)$ increases. Measurements on Nb$_3$Al thin films [167] imply that $\lambda_{tr} \approx 7$, corresponding to $w \approx 2.5$ (variations only in $\omega_{ln}$) and $w \approx 2.9$ [variations only in $N(0)$] for the range $T_C(\varepsilon_I)/T_C(0) \geq 0.92$ ($\varepsilon_I = -1.4\%$ for the Nb$_3$Al Sumitomo wire).

## 5.5.3 Comparison of theoretical and experimental results

Comparing the theoretical values for $w$ (Figure 5.17) with the experimental data (Figure 5.15), it can be seen that the agreement is considerably better if the strain-dependence of the average phonon frequencies is the dominant factor. Assuming $\lambda_{tr}(\varepsilon_I = 0) = 3$, microscopic theory gives $w = 2.4$ if $N(0)$ is constant and higher values if $N(0)$ varies, compared to the typical experimental values for high-$B_{C2}^*(0)$ wires between ~2 and ~2.5. Our results are therefore in agreement with the implications of Testardi's work [169-171], who related the strain-dependence of $T_C$ to the large phonon anharmonicity effects in $A$15 superconductors [172, 173]. Alternatively, various properties of $A$15 compounds have been related to peaks in the electronic density of states near the Fermi energy [174, 175]. However, it has been noted that tertiary additions would broaden these peaks and therefore cause a reduction in the strain-sensitivity of $T_C$ if the variations in $N(0)$ were indeed the dominant factor, whereas the opposite effect is observed experimentally [see Figure 5.14(a)] [80]. Band-structure calculations [176-178] also show that there is only a relatively small decrease in $N(0)$ ($< 3\%$) for the transition from the cubic to the tetragonal phases of Nb$_3$Sn. Here, the distortion of the unit cell in the tetragonal phase [171] can be considered as equivalent to a macroscopic strain of

$\varepsilon_1 \approx -0.44\%$ (calculated by equating the deviatoric strain components [122]). The lower values of $T_C$ (~1 K in otherwise equivalent materials) [179] and $B_{C2}(0)$ (~3 T) [180] observed for the tetragonal phase are indeed broadly consistent with our strain results (see Figure 5.14).

Some other results in the literature can be used to assess the validity of the assumptions made in the analysis and the conclusions about the microscopic mechanism. Due to a lack of information about uniaxial strain effects, it is necessary to discuss measurements of microscopic properties as a function of various other adjustable parameters. In measurements on $Nb_3Sn$ under hydrostatic pressure [153], changes in both $N(0)$ and $\omega_{ln}$ were observed, and the parameter $\langle I^2 \rangle$ increased slightly as $N(0)$ decreased (in contrast to our assumption of $\langle I^2 \rangle = \text{constant}$). The large differences between the effect of non-hydrostatic (uniaxial) strains and hydrostatic strains on the superconducting properties $(T_C)$ [123] may indicate that there is a different mechanism operating in each case (indeed, the dependences are of opposite sign in $V_3Si$ [80, 181]). Nevertheless, such a correlation between $N(0)$ and $\langle I^2 \rangle$ [182] would tend to increase the calculated value of $w$ and therefore, from the comparison with the experimental data, further strengthen the case for phononic changes being the dominant factor. We also note that experimental [183] and computational [184] data show that $\langle I^2 \rangle$ is approximately constant for series of different niobium-based superconductors. Tunnelling measurements [185] on Nb-Sn samples with varying stoichiometry show that $\mu^*$ is approximately constant for variations in $T_C$ of ~7 K, consistent with our assumption for the case of uniaxial strain. In these measurements, the largest changes in $\alpha^2 F(\omega)$ occurred at lower frequencies and therefore $\omega_{ln}$ varied more than $\omega_2$ (by ~50% for variations in $T_C$ of ~3 K): this effect would also tend to increase the calculated value of $w$ (and further emphasise the role of phononic changes).

Comparison between our experimental data and theory provides strong evidence that in high- $B_{C2}^*$ Nb$_3$Sn, uniaxial strain predominantly changes the average phonon frequencies rather than the electronic density of states at the Fermi energy. The theory—in which $w$ decreases with increasing impurity scattering rate—also provides a straightforward explanation for low values of $w$ ($\leq 2.5$) for ternary Nb$_3$Sn compared to the binary materials (~3.6) [61, 68]. Estimating $\lambda_{tr} \approx 1$ for the binary Nb$_3$Sn wires [168], and considering values of $T_C(\varepsilon_1)/T_C(0) \geq 0.94$, gives $w \approx 3.3$ for the case where phononic changes dominate and $w \approx 3.9$ for the case where the electronic changes dominate.

# 5.6 Simplified interpolative scaling law for $J_C(B,T,\varepsilon)$

In this section, a simplified version of the Interpolative Scaling Law involving fewer free parameters is presented, and the typical accuracy that can be expected when using this scaling law to extrapolate from partial $J_C(B,T,\varepsilon)$ datasets is quantified [61, 148].

**Table 5.2.** RMS errors for fits to the comprehensive $J_C(B,T,\varepsilon)$ data using various scaling laws.

| Scaling Law | RMS error (mean $I_c$) (A) | | |
|---|---|---|---|
| | EM-LMI | Vac | OST |
| | (42.5) | (61.4) | (35.7) |
| ISL | 1.40 | 2.05 | 1.35 |
| Simplified ISL (*u* free) | 1.40 | 2.50 | 1.68 |
| Simplified ISL (*u* = 0) | 1.40 | 2.50 | 1.81 |
| Simplified ISL (*u* = 1.25) | 1.55 | 3.20 | 2.33 |
| Simplified ISL [free: $A(0)$, $T_C^*(0)$, $B_{C2}^*(0,0)$, $\varepsilon_M$] | 2.10 | 6.60 | 5.71 |

**Table 5.3.** Simplified Interpolative Scaling Law parameters for (a) the EM-LMI wire, (b) the Vac wire, and (c) the OST wire. Note that for the values given in the table intrinsic strain is in units of percent and the calculated $J_C$ is the engineering critical current density in units of $Am^{-2}$.

(a) EM-LMI Wire

| $p$ | $q$ | $n$ | $v$ | $w$ | $u$ | $\varepsilon_M$ (%) |
|---|---|---|---|---|---|---|
| 0.4741 | 1.953 | 2.338 | 1.446 | 1.936 | −0.056 | 0.2786 |

| $A(0)$ $(Am^{-2}T^{3-n}K^{-2})$ | $T_C^*(0)$ (K) | $B_{C2}^*(0,0)$ (T) | $c_2$ | $c_3$ | $c_4$ |
|---|---|---|---|---|---|
| $2.446 \times 10^7$ | 16.89 | 28.54 | −0.7697 | −0.4913 | −0.0538 |

(b) Vac Wire

| $p$ | $q$ | $n$ | $v$ | $w$ | $u$ | $\varepsilon_M$ (%) |
|---|---|---|---|---|---|---|
| 0.4625 | 1.452 | 2.457 | 1.225 | 2.216 | 0.051 | 0.3404 |

| $A(0)$ $(Am^{-2}T^{3-n}K^{-2})$ | $T_C^*(0)$ (K) | $B_{C2}^*(0,0)$ (T) | $c_2$ | $c_3$ | $c_4$ |
|---|---|---|---|---|---|
| $9.460 \times 10^6$ | 17.58 | 29.59 | −0.6602 | −0.4656 | −0.1075 |

(c) OST Wire

| $p$ | $q$ | $n$ | $v$ | $w$ | $u$ | $\varepsilon_M$ (%) |
|---|---|---|---|---|---|---|
| 0.4763 | 2.150 | 3.069 | 1.240 | 2.545 | −0.912 | 0.2421 |

| $A(0)$ $(Am^{-2}T^{3-n}K^{-2})$ | $T_C^*(0)$ (K) | $B_{C2}^*(0,0)$ (T) | $c_2$ | $c_3$ | $c_4$ |
|---|---|---|---|---|---|
| $6.417 \times 10^6$ | 18.00 | 29.17 | −0.6457 | −0.4514 | −0.1009 |

## 5.6.1 Parameterisations of complete $J_C(B,T,\varepsilon)$ datasets

Firstly, we assume that the power-law relation between $B_{C2}(0,\varepsilon_I)$ and $T_C(\varepsilon_I)$ given by Equation (5.11) is valid, which was shown to be the case for the experimental and theoretical results presented in Section 5.5. Secondly, we note that the optimum polynomial functions for $A(\varepsilon_I)$ are generally quite complex (>1 turning point), but have

large associated uncertainties (for example, are sensitive to the fitting procedure) and vary considerably between different wires. Hence for simplicity (and without much loss of accuracy, as shown below), it will be assumed that $A(\varepsilon_1)$ can also be constrained as a power-law function of $T_C(\varepsilon_1)$ [148]. The simplified Interpolative Scaling Law therefore involves the following relations (the exponent $m$ has been set to 2):

$$J_C(B,T,\varepsilon_1) = A(\varepsilon_1)\left[T_C^*(\varepsilon_1)\left(1-t^2\right)\right]^2\left[B_{C2}^*(T,\varepsilon_1)\right]^{n-3}b^{p-1}(1-b)^q \qquad (5.17)$$

$$B_{C2}^*(T,\varepsilon_1) = B_{C2}^*(0,\varepsilon_1)(1-t^\nu) \qquad (5.18)$$

$$\left(\frac{A(\varepsilon_1)}{A(0)}\right)^{1/u} = \left(\frac{B_{C2}^*(0,\varepsilon_1)}{B_{C2}^*(0,0)}\right)^{1/w} = \frac{T_C^*(\varepsilon_1)}{T_C^*(0)} \qquad (5.19)$$

$$\frac{B_{C2}^*(0,\varepsilon_1)}{B_{C2}^*(0,0)} = 1 + c_2\varepsilon_1^2 + c_3\varepsilon_1^3 + c_4\varepsilon_1^4, \qquad (5.20)$$

which we take to be valid for different electron-phonon coupling strengths and impurity scattering rates. Using this simplified scaling law to fit the complete $J_C(B,T,\varepsilon)$ datasets for the Vac, EM-LMI and OST [75] Nb$_3$Sn wires gives RMS errors of ~1.5–2.5 A, as shown in Table 5.2. The simplified Interpolative Scaling Law involves 13 free parameters (compared to 17 for the ISL), the optimum values of which are shown in Table 5.3. Table 5.2 also shows errors for the simplified ISL with fixed values for $u$ [the power-law exponent for $A(\varepsilon_1)$, discussed below] and with the set of universal values proposed in the next section for the parameterisations of partial datasets [in this case, there are 4 free parameters: $A(0)$, $B_{C2}^*(0,0)$, $T_C^*(0)$, and $\varepsilon_M$].

Using Equations (5.4), (5.6), and (5.7), the prefactor $A(\varepsilon_1)$ can be written as:

$$A(\varepsilon_1) = 0.97\mu_0^{1/2}A'(\varepsilon_1)\gamma(\varepsilon_1)/\eta(\varepsilon_1). \qquad (5.21)$$

The results from microscopic theory presented in Section 5.5.2 allow the term

$\gamma(\varepsilon_1)/\eta(\varepsilon_1)$ in Equation (5.21) to be related to $T_C^*(\varepsilon_1)$. Assuming that

$A'(\varepsilon_1) = \text{constant}$, an approximate power-law relationship between $A(\varepsilon_1)$ and $T_C^*(\varepsilon_1)$ is

then obtained with exponent $u = 1.25$ (variations only in $\omega_{\ln}$) or $u = 1.65$ [variations only

in $N(0)$]. As shown in Table 5.2, however, the fits to the complete datasets using the

simplified Interpolative Scaling Law with $u = 1.25$ have RMS errors that are ~30%

higher than the fits with $u$ as a free parameter. The optimum values for $u$ are

approximately zero for the EM-LMI and Vac wires and approximately $-1$ for the OST

wire, although the latter value has a large associated uncertainty, as shown by the small

increase in the error that is observed when $u$ is fixed at zero (see Table 5.2). Hence the

large uncertainties (and our assumption about the value of the exponent $m$) prevent any

definite physical interpretation of $A'(\varepsilon_1)$ at this stage [46, 71].

The optimum values of $u$ in the simplified Interpolative Scaling Law can also be

compared with the Summers Scaling Law, in which the variation of the prefactor was

fixed so that $F_{PM}(0,\varepsilon_1) \propto \left[ B_{C2}^*(0,\varepsilon_1) \right]^{n'}$ with $n' = 1$, in approximate agreement with

Ekin's Strain Scaling Law [ $F_{PM}(0,\varepsilon_1)$ is the maximum volume pinning force at $T = 0$]

[61, 148]. In the simplified Interpolative Scaling Law, $n' = w^{-1}\left[ u + 2 + w(n-2) \right]$ and has

values of ~1.1 (EM-LMI) and ~1.2 (Vac).

## 5.6.2 Parameterisations of partial $J_C(B,T,\varepsilon)$ datasets

An important practical issue in relation to scaling laws for $J_C(B,T,\varepsilon)$ relates to the

accuracy achieved when extrapolating parameterisations of partial datasets. Given the

considerable resources involved in obtaining comprehensive $J_C(B,T,\varepsilon)$ data, it is

important to understand the minimum datasets and the types of scaling law that are

required for sufficiently accurate predictions to be made. We will investigate this issue

by using the simplified Interpolative Scaling Law to fit subsets of the complete

**Table 5.4.** Approximate universal values for parameters in the simplified Interpolative Scaling Law used for fitting partial $J_C(B,T,\varepsilon)$ datasets (the letters in brackets show the partial datasets for which the universal values are required: see Table 5.5).

| $p$ | $q$ | $n$ | $v$ | $w$ | $T_C^*(0)$ (K) |
|---|---|---|---|---|---|
| $0.5^{(abc)}$ | $2^{(abc)}$ | $2.5^{(abc)}$ | $1.5^{(abc)}$ | $2.2^{(abc)}$ | $17.5^{(b)}$ |

| $u$ | $c_2$ | $c_3$ | $c_4$ | $c_5$ |
|---|---|---|---|---|
| $0^{(c)}$ | $-0.752^{(c)}$ | $-0.419^{(c)}$ | $0.0611^{(c)}$ | $0.0619^{(c)}$ |

**Table 5.5.** RMS errors for extrapolations made from partial datasets using the simplified Interpolative Scaling Law. The extrapolations and fits are limited to $4.2\,\mathrm{K} \le T \le 8\,\mathrm{K}$ and $|\varepsilon_1| \le 1.1\%$. Also shown are the mean values of $I_C$ in the extrapolation regions.

| Partial dataset fitted | RMS error for extrapolation (mean $I_C$) (A) | | |
|---|---|---|---|
| | EM-LMI wire | Vac wire | OST wire |
| (a) $J_C(B,T,\varepsilon_A = 0)$ and $J_C(B,4.2\,\mathrm{K},\varepsilon_A)$ | 2.6 (38.0) | 3.2 (43.0) | 3.0 (27.5) |
| (b) $J_C(B,4.2\,\mathrm{K},\varepsilon_A)$ | 3.7 (38.5) | 3.7 (43.0) | 7.2 (27.5) |
| (c) $J_C(B,T,\varepsilon_A = 0)$ | 2.6 (47.5) | 5.7 (83.0) | 7.0 (50.5) |

$J_C(B,T,\varepsilon)$ datasets, and then comparing the extrapolations with the measured data in regions of parameter space not included in the fit. Three types of partial dataset will be considered: (a) $J_C(B,4.2\,\mathrm{K},\varepsilon)$ and $J_C(B,T,\varepsilon = \mathrm{constant})$ data (i.e. variable-strain measurements at 4.2 K combined with variable-temperature measurements at zero applied strain); (b) only $J_C(B,4.2\,\mathrm{K},\varepsilon)$ data; (c) only $J_C(B,T,\varepsilon = \mathrm{constant})$ data.

In all three cases, it is necessary to use an appropriate fixed value for the exponent $w$. Based on our comprehensive data for a number of technological wires (EM-LMI, Vac, OST), and consistent with microscopic theory, we propose that $w = 2.2$ is the best "universal" value to take for $Nb_3Sn$ wires characterised by high values of $B_{C2}^*(0,0)$.

Variations in $w$ of approximately ±20% are observed (and are expected due to variations in the dirtiness of the $Nb_3Sn$), but it will be shown that this universal value is adequate for the extrapolations carried out below. Although the values of some or all of the exponents $p$, $q$, $n$, and $v$ can in principle be determined from each of the partial datasets, we have found that more accurate predictions are generally obtained if these exponents are fixed at the universal values shown in Table 5.4. These universal values include the Kramer values of $p = 1/2$ and $q = 2$ [46, 58], a value of $v = 3/2$ that approximately describes (to within ~2%) the Maki-de Gennes relation for $B_{C2}(T)$ [40, 41, 43], and a half-integral value of $n = 5/2$ observed for a number of $Nb_3Sn$ wires [75, 142]. It can be seen by comparing Tables 5.3 and 5.4 that there are some differences between the optimum and universal values for these exponents, particularly for the Vac wire. Nevertheless we have found that the universal values are generally closer to the optimum global values required for accurate extrapolations than the values obtained from partial datasets.

In case (a), constraining 5 parameters ($p$, $q$, $n$, $v$, $w$) to the universal values described above results in optimum extrapolations, while case (b) also requires a fixed value of $T_C^*(\varepsilon_I = 0)$, for which we propose 17.5 K as the best universal value [75, 105]. In case (c) where no variable-strain data are available, universal relations for the strain-dependent parameters are necessary. Figure 5.14 shows evidence of a universal relation for the normalised values of $B_{C2}^*(0, \varepsilon_I)$ in $Nb_3Sn$ wires characterised by high values of upper critical field. This relation can be described by a fifth-order polynomial with values for the coefficients as shown in Table 5.4. Given the accuracy of the fits shown in Table 5.2, we suggest setting $u = 0$, which (together with $w = 2.2$) then gives approximate universal relations for the normalised values of $A(\varepsilon_I) = \text{const}$ and $T_C^*(\varepsilon_I)$. In case (c), an estimate of the equivalent intrinsic strain (i.e. the parameter $\varepsilon_M$) is also required,

which can in principle be calculated [186, 187] but represents a potentially large additional source of error.

With the appropriate parameters fixed (see Table 5.4), the remaining free parameters can be obtained by fitting the partial datasets. Table 5.5 shows the accuracy of the resulting extrapolations for three different $Nb_3Sn$ wires, where the extrapolations (and the fits) are constrained to the region of parameter space defined by $4.2\,K \le T \le 8\,K$ and $|\varepsilon_1| \le 1.1\%$. It can be seen that for case (a) the RMS differences between the calculated and measured values in the extrapolation region are typically ~8% of the mean critical current. The errors are somewhat larger for case (b), particularly for the OST wire where the RMS error is ~25%. Note also that in case (c) it has been assumed that $\varepsilon_M$ has been accurately calculated to be the optimum value, although it is found that errors of ±10% in $\varepsilon_M$ cause the RMS errors for the extrapolations to increase by ~50%. If the extrapolations are extended to the whole range of parameter space (i.e. $4.2\,K \le T \le 12\,K$ and $|\varepsilon_1| \le 1.6\%$ ) the errors increase further, typically by a factor of ~2.

In conclusion, we propose the simplified Interpolative Scaling Law for parameterising $J_C(B,T,\varepsilon)$ data. For complete datasets, it allows interpolations to be made with an accuracy of ~4% and, with fewer and more easily-determinable free parameters (in relation to the ISL), it facilitates interlaboratory and intersample comparisons. For partial datasets, the simplified Interpolative Scaling Law with appropriate fixed parameters allows extrapolations to be made that are reasonably accurate and extensive: if variable-temperature and variable-strain datasets are available, accuracies of ~8% can be achieved over limited ranges, whereas if only variable-temperature or only variable-strain data are available, the errors increase.

# 5.7 Conclusions

Comprehensive $J_C(B,T,\varepsilon)$ data are presented for the EM-LMI and Vac $Nb_3Sn$ superconducting wires used in the two ITER model coils. Various consistency tests demonstrate good interlaboratory agreement and that $J_C$ is a single-valued function of $B$, $T$, and $\varepsilon$. For high-upper-critical-field (28–30 T) $Nb_3Sn$ wires, we report an approximately universal relationship between normalised $B_{C2}^*(0)$ and intrinsic strain, and a power-law relationship between $B_{C2}^*(0,\varepsilon_{\mathrm{I}})$ and $T_C^*(\varepsilon_{\mathrm{I}})$ with a typical value of ~2.2 for the exponent. Both results differ from those obtained previously for binary, low-upper-critical-field (~24 T) $Nb_3Sn$ wires in which $B_{C2}^*(0)$ and $T_C^*$ are less strain-dependent and the power-law exponent is larger ($\geq 3$). The standard Summers Scaling Law therefore predicts a weaker strain-dependence for $J_C$ and does not accurately fit the $J_C(B,T,\varepsilon)$ data for either the EM-LMI or Vac wires. Analysis of the relationship between $B_{C2}^*(0,\varepsilon_{\mathrm{I}})$ and $T_C^*(\varepsilon_{\mathrm{I}})$ using microscopic theory shows that the calculated value for the power-law exponent decreases with increasing impurity scattering rate in agreement with the experimental data, and that the uniaxial strain effects are predominantly due to changes in the average phonon frequencies rather than the electronic density of states at the Fermi energy. We propose a simplified Interpolative Scaling Law to describe $J_C(B,T,\varepsilon)$ in technological $Nb_3Sn$ wires with high values of upper critical field, motivated by microscopic theory and scaling considerations. The scaling law incorporates a polynomial function for normalised $B_{C2}^*(0,\varepsilon_{\mathrm{I}})$ and modified power-law relations between the strain-dependent variables. It allows accurate (~4%) parameterisations to be made of complete $J_C(B,T,\varepsilon)$ datasets and, with appropriate universal values for some of the parameters, reasonably accurate and extensive predictions to be made from partial datasets.

# Chapter 6

# Future work

In this final chapter, we will consider the possible future directions of the work reported in this thesis.

The apparatus and techniques that have been developed make it possible to perform variable-strain measurements on most superconducting wires or tapes (with appropriate spring designs). Data for Nb$_3$Sn will continue to be required in the future, as new wires are developed and mass-produced for ITER, and as applications such as NMR move to even higher magnetic fields (where $J_C$ is more strain-sensitive). Various other groups have carried out investigations of the high-temperature superconductor (Bi,Pb)$_2$Sr$_2$Ca$_2$Cu$_3$O$_x$ and magnesium diboride—the recently-discovered superconductor with $T_C = 39$ K. However, the strain effects in these materials are found to be largely due to cracking in the filaments, in contrast to the reversible, intrinsic changes in Nb$_3$Sn. We have recently obtained $J_C(B,T,\varepsilon)$ data for an advanced ITER Nb$_3$Sn wire, and a Chevrel phase PbMo$_6$S$_8$ superconducting wire, which shows large reversible strain effects but a breakdown of scaling (discussed below). The Nb$_3$Sn wire has a much higher critical current than the wires measured previously, typically by a factor of 2, and is approaching the operating limits of the strain probe. In the future, a new probe may be required that is capable of measuring currents up to ~1000 A, which can be achieved with careful design of the current leads.

The new scaling law presented in Chapter 5 is, we believe, the best approach to parameterising $J_C(B,T,\varepsilon)$ data for technological Nb$_3$Sn wires. This will be tested as

data for new wires become available. Some parts of the scaling-law framework can be developed in the future. The empirical function for the strain-dependence of $B_{C2}^*(0)$ (or $T_C^*$) could eventually be replaced with an alternative function motivated by a theoretical model but still remaining sufficiently accurate for engineering purposes. This is an active but complex area of research, requiring calculations of the three-dimensional strain-state of the $Nb_3Sn$ filaments (e.g. by FEA) and the strain dependence of the microscopic and hence superconducting parameters of $Nb_3Sn$. It is also possible to further investigate the scaling law exponents $(p, q, m, n, u)$ and their connection with flux-pinning models. However, we believe that progress in this area may require a (non-scaling) model that explicitly includes distributions in the superconducting parameters. The $Nb_3Sn$ data do indeed show small systematic deviations from the scaling law, while such an approach may also allow us to develop a framework for parameterising the $n$-value, which is presently unavailable. Our recent data for the Chevrel Phase wire show a much larger breakdown of scaling, and it is clear that a new model is required in this case. It is our belief that comprehensive critical current density measurements as a function of magnetic field, temperature, and strain are a promising way of investigating flux pinning in both low- and high-temperature superconductors.

# *References*

[1]     H. K. Onnes, Communications from the Physical Laboratory of the University of Leiden **124C**, 21 (1911).

[2]     J. File and R. G. Mills, Phys. Rev. Lett. **10**, 93 (1963).

[3]     W. Meissner and R. Ochsenfeld, Naturwissenschaften **21**, 787 (1933).

[4]     P. Dai, B. C. Chakoumakos, G. F. Sun, K. W. Wong, Y. Xin, and D. F. Lu, Physica C **243**, 201 (1995).

[5]     A. A. Abrikosov, Sov. Phys. JETP **5**, 1174 (1957).

[6]     H. Traüble and U. Essmann, J. Appl. Phys. **39**, 4052 (1968).

[7]     E. J. Eck, http://www.superconductors.org, 2004.

[8]     V. V. Struzhkin, M. I. Eremets, W. Gan, H. K. Mao, and R. J. Hemley, Science **298**, 1213 (2002).

[9]     R. Flukiger, in *Handbook of Superconducting Materials*, edited by D. Cardwell and D. Ginley (IOP Publishing, Bristol, 2003), Vol. 1, p. 391.

[10]    J. Nagamatsu, N. Nakagawa, T. Muranaka, Y. Zenitani, and J. Akimitsu, Nature **410**, 63 (2001).

[11]    D. P. Hampshire, in *Handbook of Superconducting Materials*, edited by D. Cardwell and D. Ginley (IOP, Bristol, 2002), Vol. 2, p. 1903.

[12]    L. D. Cooley, P. Lee, and D. C. Larbalestier, in *Handbook of Superconducting Materials*, edited by D. Cardwell and D. Ginley (IOP Publishing, Bristol, 2002), Vol. 1, p. 603.

[13]    T. Miyazaki, T. Hase, and T. Miyatake, in *Handbook of Superconducting Materials*, edited by D. Cardwell and D. Ginley (IOP Publishing, Bristol, 2003), Vol. 2, p. 639.

[14]    J. G. Bednorz and K. A. Müller, Z. Phys. B **64**, 189 (1986).

[15]    M. K. Wu, J. R. Ashburn, C. J. Torng, P. H. Hor, R. L. Meng, L. Gao, Z. J. Huang, Y. Q. Wang, and C. W. Chu, Phys. Rev. Lett. **58**, 908 (1987).

[16]    H. Maeda, Y. Tanaka, M. Fukutomi, and T. Asano, Jap. J. Appl. Phys. **27**, L209 (1988).

[17]    R. C. Weast, M. J. Astle, and W. H. Beyet, *Handbook of Chemistry and Physics* (CRC Press, Boca Raton, FL, 1989).

[18]    D. N. Zheng, H. D. Ramsbottom, and D. P. Hampshire, Phys. Rev. B **52**, 12931 (1995).

[19]    C. Buzea and T. Yamashita, Supercond. Sci. Tech. **14**, R115 (2001).

[20]    D. R. Harshman and A. P. Mills Jr., Phys. Rev. B **45**, 10684 (1992).

[21]    F. London and H. London, Proc Roy Soc (London) **A149**, 71 (1935).

[22]    C. J. Gorter and H. B. G. Casimir, Phys. Z. **35**, 963 (1934).

[23]    V. L. Ginzburg and L. D. Landau, Zh. Eksp. Teor. Fiz. **20**, 1064 (1950).

[24]    D. R. Tilley and J. Tilley, *Superfluidity and Superconductivity* (IOP publishing Ltd., Bristol, 1990).

[25]    W. H. Kleiner, L. M. Roth, and S. H. Autler, Phys. Rev. **133**, A1226 (1964).

[26]    H. F. Hess, R. B. Robinson, R. C. Dynes, J. M. Valles Jr, and J. V. Waszczak, Phys. Rev. Lett. **62**, 214 (1989).

[27]    T. P. Orlando, E. J. McNiff, S. Foner, and M. R. Beasley, Phys. Rev. B **19**, 4545 (1979).

[28]    H. J. Niu and D.P.Hampshire, Phys. Rev. Lett. **91**, 027002 (2003).

[29]    J. Bardeen, L. N. Cooper, and J. R. Schrieffer, Phys. Rev. **108**, 1175 (1957).

[30]    H. Fröhlich, Phys. Rev. **79**, 845 (1950).

[31]    L. N. Cooper, Phys. Rev. **104**, 1189 (1956).

[32]    J. R. Waldram, *Superconductivity of Metals and Cuprates* (IOP Publishing Ltd., London, 1996).

[33]    G. M. Eliashberg, Sov. Phys. JETP **11**, 696 (1960).

[34]    D. J. Scalapino, J. R. Schrieffer, and J. W. Wilkins, Phys. Rev. **148**, 263 (1966).

[35]    P. B. Allen and R. C. Dynes, Phys. Rev. B **12**, 905 (1975).

[36]    W. L. McMillan, Phys. Rev. **167**, 331 (1968).

[37]    J. P. Carbotte, Rev. Mod. Phys. **62**, 1027 (1990).

[38]    L. P. Gor'kov, Sov. Phys. JETP **9**, 1364 (1959).

[39]    B. B. Goodman, Rep. Prog. Phys. **29**, 445 (1966).

[40]    K. Maki, Physics **1**, 21 (1964).

[41]    E. Helfand and N. R. Werthamer, Phys. Rev. **147**, 288 (1966).

[42]    N. R. Werthamer, E. Helfand, and P. C. Hohenberg, Phys. Rev. **147**, 295 (1966).

[43]    P. G. De Gennes, Phys. Kondens. Mater. **3**, 79 (1964).

[44]    A. M. Campbell and J. E. Evetts, Adv. Phys. **21**, 395 (1972).

[45]    J. Bardeen and M. J. Stephen, Phys. Rev. **140**, 1197 (1965).

[46]    D. Dew-Hughes, Philos. Mag. **30**, 293 (1974).

[47]    W. A. Fietz and W. W. Webb, Phys. Rev. **178**, 657 (1969).

[48]    D. Dew-Hughes, Philos. Mag. B **55**, 459 (1987).

[49]    A. I. Larkin and Y. N. Ovchinnikov, J. Low Temp. Phys. **34**, 409 (1979).

[50]  M. V. Feigel'man, V. B. Geshkenbein, A. I. Larkin, and V. M. Vinokur, Phys. Rev. Lett. **63**, 2303 (1989).

[51]  P. W. Anderson and Y. B. Kim, Rev. Mod. Phys. **36**, 39 (1964).

[52]  P. W. Anderson, Phys. Rev. Lett. **9**, 309–311 (1962).

[53]  R. Wördenweber, Rep. Prog. Phys. **62**, 187 (1999).

[54]  E. J. Kramer and H. C. Freyhardt, J. Appl. Phys. **51**, 4930 (1980).

[55]  E. V. Thuneberg, Cryogenics **29**, 236 (1989).

[56]  A. Pruymboom, P. H. Kes, E. van der Drift, and S. Radelaar, Phys. Rev. Lett. **60**, 1430 (1988).

[57]  A. Pruymboon, P. H. Kes, E. Drift, and S. Radelaar, Appl. Phys. Lett. **52**, 662 (1988).

[58]  E. J. Kramer, J. Appl. Phys. **44**, 1360 (1973).

[59]  E. H. Brandt, Phys. Stat. Solid. B **77**, 551 (1976).

[60]  J. E. Evetts and C. J. G. Plummer, in *International Symposium on Flux Pinning and Electromagnetic Properties of Superconductors, Fukuoka, 1985*, edited by T. Matsushita, K. Yamafuji, and F. Irie (Matsukuma, Fukuoka, 1985), p. 146.

[61]  J. W. Ekin, Cryogenics **20**, 611 (1980).

[62]  B. ten Haken, A. Godeke, and H. H. J. ten Kate, J. Appl. Phys. **85**, 3247 (1999).

[63]  N. Cheggour and D. P. Hampshire, J. Appl. Phys. **86**, 552 (1999).

[64]  H. J. N. van Eck, D. C. van der Laan, M. Dhallé, B. tenHaken, and H. H. J. ten Kate, Supercond. Sci. Tech. **16**, 1026 (2003).

[65]  D. Uglietti, B. Seeber, V. Abacherli, A. Pollini, D. Eckert, and R. Flukiger, Supercond. Sci. Tech. **16**, 1000 (2003).

[66]  C. R. Walters, I. M. Davidson, and G. E. Tuck, Cryogenics **26**, 406 (1986).

[67]  D. M. J. Taylor and D. P. Hampshire, (in progress).

[68]  T. Luhman, M. Suenaga, and C. J. Klamut, Adv. Cryo. Eng. **24**, 325 (1978).

[69]  G. Rupp, IEEE Trans. Appl. Supercond. **13**, 1565 (1977).

[70]  B. ten Haken, Ph.D. thesis, University of Twente, 1994.

[71]  D. M. Kroeger, D. S. Easton, A. DasGupta, C. C. Koch, and J. O. Scarbrough, J. Appl. Phys. **51**, 2184 (1980).

[72]  J. W. Ekin and S. L. Bray, Adv. Cryo. Eng. **42**, 1407 (1996).

[73]  W. Specking, J. L. Duchateau, and P. Decool, in *Proceedings of the 15th International Conference on Magnet Technology*, edited by L. Liangzhen, S. Guoliao, and Y. Luguang (Science Press, Beijing, 1998), p. 1210.

[74] S. T. Wang, R. Wahrer, C. J. Chen, T. S. Tenforde, R. M. Scanlan, J. W. Ekin, and S. Bray, IEEE Trans. Magn. **30**, 2344 (1994).

[75] S. A. Keys and D. P. Hampshire, Supercond. Sci. Tech. **16**, 1097 (2003).

[76] N. Mitchell, Fusion Eng. Des. **66-8**, 971 (2003).

[77] J. W. Ekin, F. R. Fickett, and A. F. Clark, Adv. Cryo. Eng. **22**, 449 (1975).

[78] S. A. Keys, N. Koizumi, and D. P. Hampshire, Supercond. Sci. Tech. **15**, 991 (2002).

[79] T. Takeuchi, Y. Iijima, K. Inoue, H. Wada, B. ten Haken, H. H. J. ten Kate, K. Fukuda, G. Iwaki, S. Sakai, and H. Moriai, Appl. Phys. Lett. **71**, 122 (1997).

[80] J. W. Ekin, Adv. Cryo. Eng. **30**, 823 (1984).

[81] T. Kuroda, H. Wada, Y. Iijima, and K. Inoue, J. Appl. Phys. **65**, 4445 (1989).

[82] W. Goldacker, W. Specking, F. Weiss, G. Rimikis, and R. Flukiger, Cryogenics **29**, 955 (1989).

[83] J. W. Ekin, T. Yamashita, and K. Hamasaki, IEEE Trans. Magn. **21**, 474 (1985).

[84] W. Goldacker and S. I. Schlachter, Physica C **378–381**, 889 (2002).

[85] H. Kitaguchi, A. Matsumoto, H. Hatakeyama, and H. Kumakura, Supercond. Sci. Tech. **16**, 976 (2003).

[86] J. W. Ekin, D. K. Finnemore, Q. Li, J. Tenbrink, and W. Carter, Appl. Phys. Lett. **61**, 858 (1992).

[87] W. Goldacker, J. Kessler, B. Ullmann, E. Mossang, and M. Rikel, IEEE Trans. Appl. Supercond. **5**, 1834 (1995).

[88] H. Kitaguchi, K. Itoh, H. Kumakura, T. Takeuchi, K. Togano, and H. Wada, IEEE Trans. Appl. Supercond. **11**, 3058 (2001).

[89] M. Suenaga, Y. Fukumoto, P. Haldar, T. R. Thurston, and U. Wildgruber, Appl. Phys. Lett. **67**, 3025 (1995).

[90] R. Passerini, M. Dhallé, E. Giannini, G. Witz, B. Seeber, and R. Flukiger, Physica C **371**, 173 (2002).

[91] N. Cheggour, J. W. Ekin, C. C. Clickner, D. T. Verebelyi, C. L. H. Thieme, R. Feenstra, and A. Goyal, Appl. Phys. Lett. **83**, 4223 (2003).

[92] W. Goldacker, in *Handbook of Superconducting Materials*, edited by D. Cardwell and D. S. Ginley (IOP, Bristol, 2003), Vol. 2, p. 1527.

[93] N. Cheggour and D. P. Hampshire, Rev. Sci. Instrum. **71**, 4521 (2000).

[94] A. Godeke, M. Dhallé, A. Morelli, L. Stobbelaar, H. van Weeren, H. J. N. van Eck, W. Abbas, A. Nijhuis, A. den Ouden, and B. ten Haken, Rev. Sci. Instrum. **75**, 5112 (2004).

[95] L. F. Goodrich and F. R. Fickett, Cryogenics **22**, 225 (1982).

[96]   S. A. Keys and D. P. Hampshire, in *Handbook of Superconducting Materials*, edited by D. Cardwell and D. Ginley (IOP Publishing, Bristol, 2003), Vol. 2, p. 1297.

[97]   J. W. Ekin, J. Appl. Phys. **49**, 3406 (1978).

[98]   M. Polak, W. Zhang, J. Parrell, X. Y. Cai, A. Polyanskii, E. E. Hellstrom, D. C. Larbalestier, and M. Majoros, Supercond. Sci. Tech. **10**, 769 (1997).

[99]   International Electrotechnical Commission Report No. 61788-2 (First edition), 1999.

[100]  H. Wada, L. F. Goodrich, C. Walters, and K. Tachikawa, Cryogenics **35**, S105 (1995).

[101]  D. M. J. Taylor, S. A. Keys, and D. P. Hampshire, Physica C **372**, 1291 (2002).

[102]  A. Vostner (private communication).

[103]  B. ten Haken, A. Godeke, H. H. J. ten Kate, and W. Specking, IEEE Trans. Magn. **32**, 2739 (1996).

[104]  R. Zanino and L. Savoldi-Richard, Cryogenics **43**, 91 (2003).

[105]  A. Godeke and H. G. Knoopers, University of Twente Report No. UT-NET 98-5, 1998.

[106]  D. M. J. Taylor and D. P. Hampshire, Supercond. Sci. Tech. **18**, 356 (2005).

[107]  F. Mathu and H. C. Meijer, Cryogenics **22**, 428 (1982).

[108]  J. Yeager and M. A. Hrusch-Tupta, *Fifth Edition, Low Level Measurements* (Keithley Instruments, Inc., Cleveland, OH, 2000).

[109]  NIST, http://cryogenics.nist.gov/, 2004.

[110]  R. C. Rice, J. L. Jackson, J. Bakuckas, and S. Thompson, U.S. Department of Transportation, Federal Aviation Administration Report No. DOT/FAA/AR-MMPDS-01, 2003.

[111]  A. F. Clark, in *Materials at Low Temperatures*, edited by R. P. Reed and A. F. Clark (American Society for Metals, Metals Park, OH, 1983), p. 75.

[112]  MatWeb, www.matweb.com, 2004.

[113]  N. Mitchell, ITER JCT Report No. 01/06/04, 2004.

[114]  A. Nyilas, in *Advances in Cryogenic Engineering: Transactions of the International Cryogenic Materials Conference 2003*, edited by U. B. Balachandran (Springer-Verlag, New York, 2004), Vol. 50, p. 151.

[115]  A. Nyilas, K. Osamura, and M. Sugano, Supercond. Sci. Tech. **16**, 1036 (2003).

[116]  D. M. J. Taylor and D. P. Hampshire, Physica C **401**, 40 (2003).

[117]  D. M. J. Taylor, S. A. Keys, and D. P. Hampshire, Cryogenics **42**, 109 (2002).

[118]  Anonymous, Vishay Measurements Group Report No. TN-504 (Appendix), 2004.

[119]  J. L. Duchateau, M. Spadoni, E. Salpietro, D. Ciazynski, M. Ricci, P. Libeyre, and A. della Corte, Supercond. Sci. Tech. **15**, R17 (2002).

[120] P. J. Lee and D. C. Larbalestier, IEEE Trans. Appl. Supercond. **11**, 3671 (2001).

[121] H. Ford, *Advanced Mechanics of Materials* (Longmans Green and Co, London, 1963).

[122] A. Godeke, B. ten Haken, and H. H. J. ten Kate, Physica C **372 - 376**, 1295 (2002).

[123] D. O. Welch, Adv. Cryo. Eng. **26**, 48 (1980).

[124] B. ten Haken, A. Godeke, and H. H. J. ten Kate, IEEE Trans. Magn. **30**, 1867 (1994).

[125] S. Murase, H. Okamoto, T. Wakasa, T. Tsukii, and S. Shimamoto, IEEE Trans. Appl. Supercond. **13**, 3386 (2003).

[126] W. Goldacker and R. Flukiger, IEEE Trans. Magn. **21**, 807 (1985).

[127] W. D. Markiewicz, Cryogenics **44**, 767 (2004).

[128] B. ten Haken, A. Godeke, and H. H. J. ten Kate, IEEE Trans. Appl. Supercond. **5**, 1909 (1995).

[129] A. Martínez and J. L. Duchateau, Cryogenics **37**, 865 (1997).

[130] W. Turner, Patent No. US4416739 (22 November 1983).

[131] N. Cheggour and D. P. Hampshire, Cryogenics **42** (2002).

[132] S. Ochiai and K. Osamura, Cryogenics **32**, 584 (1992).

[133] P. Bruzzone, A. M. Fuchs, B. Stepanov, and G. Vecsey, IEEE T. Appl. Supercon. **12**, 516 (2002).

[134] G. Rupp, in *Filamentary A15 Superconductors*, edited by M. Suenaga and A. F. Clark (Plenum Press, New York, 1980), p. 155.

[135] R. Aymar, Fusion Eng. Des. **55**, 107 (2001).

[136] R. Zanino, N. Mitchell, and L. Savoldi-Richard, Cryogenics **43**, 179 (2003).

[137] M. Takayasu, R. A. Childs, R. N. Randall, R. J. Jayakumar, and J. V. Minervini, IEEE Trans. Appl. Supercond. **9**, 644 (1999).

[138] M. Spadoni (private communication).

[139] D. P. Hampshire, D. M. J. Taylor, P. Foley, and S. A. Keys, University of Durham Report No. DurSC0601, 2001.

[140] A. Godeke and H. J. G. Krooshoop, University of Twente Report No. UT-NET/EFDA 2000-5, 2000.

[141] R. Zanino, M. Bagnasco, G. Dittrich, W. H. Fietz, H. Fillunger, D. P. Hampshire, R. Heller, P. Komarek, O. Langhans, R. Maix, V. Marchese, N. Martovetsky, N. Mitchell, A. Nijhuis, S. Raff, M. Ricci, M. Suesser, E. Salpietro, L. Savoldi Richard, D. M. J. Taylor, A. Ulbricht, A. Vostner, F. Wuechner, and G. Zahn, IEEE Trans. Appl. Supercond. **14**, 1519 (2004).

[142] D. P. Hampshire, H. Jones, and E. W. J. Mitchell, IEEE Trans. Magn. **21**, 289 (1984).

[143] D. S. Easton and R. E. Schwall, Appl. Phys. Lett. **29**, 319 (1976).

[144] E. Buehler and H. J. Levinstein, J. Appl. Phys. **36**, 3856 (1965).

[145] J. W. Ekin, Appl. Phys. Lett. **29**, 216 (1976).

[146] I. L. McDougall, IEEE Trans. Magn. **11**, 1467 (1975).

[147] G. Rupp, IEEE Trans. Magn. **15**, 189 (1979).

[148] L. T. Summers, M. W. Guinan, J. R. Miller, and P. A. Hahn, IEEE Trans. Magn. **27**, 2041 (1991).

[149] ITER, Design Requirements and Guidelines Level 1 (Annex), 2002.

[150] J. W. Ekin, J. Appl. Phys. **62**, 4829 (1987).

[151] K. Katagiri, T. Kuroda, H. Wada, H. S. Shin, K. Watanabe, K. Noto, Y. Shoji, and H. Seto, IEEE Trans. Appl. Supercond. **5**, 1900 (1995).

[152] B. ten Haken, A. Godeke, and H. H. J. ten Kate, in *Proceedings of EUCAS 1995, the 2nd European Conference on Applied Superconductivity*, edited by D. Dew-Hughes (IOP Publishing, Bristol, 1995), p. 85.

[153] K. C. Lim, J. D. Thompson, and G. W. Webb, Phys. Rev. B **27**, 2781 (1983).

[154] B. L. Brandt, D. W. Liu, and L. G. Rubin, Rev. Sci. Instrum. **70**, 104 (1999).

[155] Y. Takahashi, N. Koizumi, Y. Nunoya, Y. Takaya, and H. Tsuji, IEEE Trans. Appl. Supercond. **12**, 1799 (2002).

[156] H. Wada, L. F. Goodrich, C. Walters, and K. Tachikawa, Cryogenics **35**, S65 (1995).

[157] E. D. Marquandt, J. P. Lee, and R. Radebaugh, in *Cryocooler 11*, edited by R. G. Ross Jr. (Kluwer Academic/Plenum Publishers, New York, 2001), p. 681.

[158] R. Zanino and L. Savoldi-Richard, Cryogenics **43**, 79 (2003).

[159] L. F. Goodrich, L. T. Medina, and T. C. Stauffer, Adv. Cryo. Eng. **44**, 873 (1998).

[160] H. Kupfer and W. Gey, Philos. Mag. **36**, 859 (1977).

[161] A. B. Sneary, C. M. Friend, J. C. Vallier, and D. P. Hampshire, IEEE Trans. Appl. Supercond. **9**, 2585 (1999).

[162] L. F. Goodrich and T. C. Stauffer, IEEE Trans. Appl. Supercond. **11**, 3234 (2001).

[163] A. Nijhuis, presented at ITER meeting, Naka, Japan, 2003 (unpublished).

[164] A. Godeke, M. C. Jewell, A. A. Golubov, B. Ten Haken, and D. C. Larbalestier, Supercond. Sci. Tech. **16**, 1019 (2003).

[165] E. L. Wolf, J. Zasadzinski, G. B. Arnold, D. F. Moore, J. M. Rowell, and M. R. Beasley, Phys. Rev. B **22**, 1214 (1980).

[166] J. Kwo and T. H. Geballe, Phys. Rev. B **23**, 3230 (1981).

[167] J. Kwo, T. P. Orlando, and M. R. Beasley, Phys. Rev. B **24**, 2506 (1981).

[168] M. Suenaga, D. O. Welch, R. L. Sabatini, O. F. Kammerer, and S. Okuda, J. Appl. Phys. **59**, 840 (1986).

[169] L. R. Testardi, Rev. Mod. Phys. **47**, 637 (1975).

[170] L. R. Testardi, Phys. Rev. B **5**, 4342 (1972).

[171] L. R. Testardi, in *Physical Acoustics*, edited by W. P. Mason and R. N. Thurston (Academic, New York, 1973), Vol. 10, p. 193.

[172] J. R. Patel and B. W. Batterman, Phys. Rev. **148**, 662 (1966).

[173] M. Poirier, F. Laroche, M. Martin, and J. F. Bussiere, Appl. Phys. Lett. **47**, 92 (1985).

[174] M. Weger and I. B. Goldberg, in *Solid State Physics*, edited by H. Ehrenreich, F. Seitz, and D. Turnbull (Academic, New York, 1973), Vol. 28, p. 1.

[175] B. M. Klein, L. L. Boyer, D. A. Papaconstantopoulos, and L. F. Mattheiss, Phys. Rev. B **18**, 6411 (1979).

[176] W. Weber and L. F. Mattheiss, Phys. Rev. B **25**, 2270 (1982).

[177] B. Sadigh and V. Ozolins, Phys. Rev. B **57**, 2793 (1998).

[178] L. F. Mattheiss and W. Weber, Phys. Rev. B **25**, 2248 (1982).

[179] L. J. Vieland and A. W. Wicklund, Phys. Lett. **34A**, 43 (1971).

[180] S. Foner and J. McNiff, E.J., Solid State Commun. **39**, 959 (1981).

[181] C. W. Chu and V. Diatschenko, Phys. Rev. Lett. **41**, 572 (1978).

[182] J. J. Hopfield, Phys. Rev. **186**, 443 (1969).

[183] A. Junod, T. Jarlborg, and J. Muller, Phys. Rev. B **27**, 1568 (1983).

[184] B. M. Klein, L. L. Boyer, and D. A. Papaconstantopoulos, Phys. Rev. Lett. **42**, 530 (1979).

[185] D. A. Rudman and M. R. Beasley, Phys. Rev. B **30**, 2590 (1984).

[186] S. Ochiai, K. Osamura, and K. Watanabe, J. Appl. Phys. **74**, 440 (1993).

[187] D. S. Easton, D. M. Kroeger, W. Specking, and C. C. Koch, J. Appl. Phys. **51**, 2748 (1980).

# *Appendix 1: Publications*

1. *The scaling law for the strain-dependence of the critical current density in $Nb_3Sn$ superconducting wires*

   D. M. J. Taylor and D. P. Hampshire, in progress (2005).

2. *Properties of helical springs used to measure the effect of axial strain on the critical current density of superconducting wires*

   D. M. J. Taylor and D. P. Hampshire, Supercond. Sci. Tech., **18**, 356 (2005).

3. *$T_{CS}$ tests and performance assessment of the ITER Toroidal Field Model Coil (Phase II)*

   R. Zanino,..., D. M. J. Taylor, *et al.*, IEEE Trans. Appl. Supercond. **14**, 1519 (2004).

4. *Effect of axial strain cycling on the critical current density and n-value of ITER niobium-tin wires*

   D. M. J. Taylor and D. P. Hampshire, Physica C **401**, 40 (2004).

5. *E-J characteristics and n-values of a niobium-tin superconducting wire as a function of magnetic field, temperature and strain*

   D. M. J. Taylor, S. A. Keys, and D. P. Hampshire, Physica C **372–376**, 1291 (2002).

6. *Reversible and irreversible effects of strain on the critical current density of a niobium-tin superconducting wire*

   D. M. J. Taylor, S. A. Keys, and D. P. Hampshire, Cryogenics **42**, 109 (2002).

# *Appendix 2: Conferences, courses, and placements*

## Conference presentations:

*Talks:*

1. International Cryogenics Material Conference: Topical Conference, University of Twente, Netherlands, May 2003 *(Invited talk)*.

2. Condensed Matter and Material Physics Conference (CMMP), Belfast, April 2003.

*Posters:*

1. CMMP, University of Warwick, April 2004.

2. SET for Britain, House of Commons, London, March 2004.

3. IOP Superconductivity Group Annual Conference, University of Cambridge, January 2003 *(Best Student Poster Prize)*.

4. CMMP, Brighton, April 2002.

5. Superconductivity Group Conference, University of Cambridge, January 2002.

6. 5th European Conference on Applied Superconductivity, Copenhagen, August 2001.

7. Superconductivity Group Conference, University of Birmingham, April 2001.

## Courses and placements:

1. EPSRC/IOP Theory of Condensed Matter Summer School, Ambleside, August– September 2003.

2. Industrial CASE Placement, Oxford Instruments Superconductivity, Eynsham, April– July 2002.

3. Superconductivity Winter School, University of Cambridge, January 2002.

4. IOP Low Temperature Techniques Course, Birmingham, November 2000.

# *Appendix 3: Computer Programs*

1. *JC(B,T,eps)_G.vi*

   LabVIEW program to run $J_c(B,T,\varepsilon)$ measurements in Grenoble. Controls the in-house magnet console, three Lakeshore temperature controllers, McLennan stepper-motor controller (optional), Oxford Instruments power supply (for the sample current), and three Keithley 2000 voltmeters (for reading the sample current and voltages from two sets of taps).

2. *JC(B,T,eps)_D.vi*

   LabVIEW program to run $J_c(B,T,\varepsilon)$ measurements in Durham. As above, but controls an Oxford Instruments magnet power supply.

3. *Strain_Cycling.vi*

   LabVIEW program to perform multiple strain cycles using the stepper motor and controller.

4. *Blank_VI.xls*

   A Microsoft Excel spreadsheet with a number of Visual Basic Macros to analyse the *V–I* data and calculate values for the critical current density and *n*-value.

5. *Rect_2.st7, Tee_2.st7*

   Strand7 FEA models of the rectangular and tee-shaped springs with attached wires.

6. *Rect_2.inp, Tee_2.inp*

   ANSYS input files for building FEA models of rectangular and tee-shaped springs with attached wires.